UCSF
UC San Francisco Electronic Theses and Dissertations

Title

Structural characterization of the PEAK3/14-3-3 and PI3Kα/KRas complexes

Permalink

https://escholarship.org/uc/item/1jm0r2x3

Author

Torosyan, Hayarpi

Publication Date

2024

Peer reviewed|Thesis/dissertation

eScholarship.org Powered by the California Digital Library
University of California

Structural characterization of the PEAK3/14-3-3 and PI3Kα/KRas complexes

by
Hayarpi Torosyan

DISSERTATION
Submitted in partial satisfaction of the requirements for degree of
DOCTOR OF PHILOSOPHY

in

Biophysics

in the

GRADUATE DIVISION
of the
UNIVERSITY OF CALIFORNIA, SAN FRANCISCO

Approved:

DocuSigned by:
Natalia Jura
E438674A382B42F...

Natalia Jura
Chair

DocuSigned by:
Kliment Verba
DC0B9413C4A0416...

Kliment Verba

DocuSigned by:
Kevan Shokat
DC0B9413C4A0416...

Kevan Shokat

DocuSigned by:
Orion Weiner
DC0B9413C4A0416...

Orion Weiner

Committee Members

Copyright 2024

by

Hayarpi Torosyan

Dedicated to my parents,

Susanna Simonyan and Simon Torosyan

ACKNOWLEDGMENTS

First of all, I would like express my gratitude to my advisors, Natalia Jura and Kliment Verba, for their guidance and support during my doctoral journey. You not only supported me in my scientific endeavors, but also celebrated my personal milestones and offered understanding and support during the more challenging times. Natalia, thank you for encouraging me to be a curious and determined investigator and teaching me how to communicate science with compelling storytelling. Klim, thank you for taking the time to train me in cryo-EM, delving into the intricacies of every experiment, and most importantly, teaching me to think deeply about my science.

Next, I would like to thank all of the members of the Jura and Verba labs whom I have had the privilege to learn from during my graduate studies. Thank you for creating such a fun and welcoming environment. The boba runs, hot pot nights, and gossip sessions, of course, provided much-needed breaks from the failing science. I would also like to thank the UCSF community, in particular, the members of my thesis committee: Kevan Shokat and Orion Weiner. Thank you for giving me your time and scientific expertise during my training. Your support, positivity and encouragement helped me navigate the emotional highs and lows that often come with scientific pursuit. Thank you to the UCSF EM Core Facility heroes, David Bulkley and Glenn Gilbert. Your dedication and expertise were invaluable. Thank you to the UCSF Biophysics program for the opportunity to study at UCSF and for granting me access to its brilliant and collaborative scientific minds and state-of-the-art resources. I would like to give special thanks to the Biophysics directors, Tanja Kortemme, James Fraser, and Aashish Manglik, as well as the wonderful Nicole Flowers, for making it all possible.

Thank you to my friends who have been with me from the start, as well as those who have come into my life along the way. You are some of the kindest, most thoughtful and funniest people that I know, and I feel so lucky to have you by my side. Thank you to my entire family. I am incredibly fortunate to have your unconditional love and support. Susan and Simon, everything I have achieved is a testament to your loving parenting and all the opportunities you have afforded me through your hard work.

Finally, thank you to my husband, Stevo Bailey, who deserves an honorary doctoral for all the support he has given me throughout my PhD. From serving as my personal stat mech TA, to pausing his video games to decipher error messages on data processing workstations, believing me when I said we would only stop by lab for 20 minutes on a Saturday and driving with me to campus at 2 AM to rescue my grid from a warming Krios. Most importantly, thank you for being my on-call therapist during the difficult times and encouraging me to celebrate the small victories. I feel so lucky to have met you before embarking on this crazy journey, because I truly could not have done it without you.

Portions of this dissertation are reproductions of material previously published in:

Torosyan, H.*, Paul, M.D.*, Forget, A., Lo, M., Diwanji, D., Pawlowski, K., Krogan, N.J., Jura, N., Verba, K.A. (2023). "Structural insights into regulation of the PEAK3 pseudokinase scaffold by 14-3-3." *Nat Commun* **14**, 3543. (*) Denotes equal contribution.

Torosyan, H., Meyer, B., Verba, K.A., Jura, N. (2024). "Membrane-bound structures of the PI3Kα/KRas complex reveal dynamic activation of PI3Kα." (in preparation)

Structural characterization of the PEAK3/14-3-3 and PI3Kα/KRas complexes

Hayarpi Torosyan

ABSTRACT

Cell communication is a dynamic process in which extracellular signals are transformed into biological responses through an intricate network of protein-protein interactions. These interactions can modulate cell signaling in a context-dependent manner, ensuring cellular homeostasis. Disruptions within these networks compromise normal cell communication, leading to disease. While the functional roles of many protein interaction partners have been studied in depth, their high-resolution structural characterization is lacking. Determining the structures of these integral protein complexes is essential to gain mechanistic insight into their functions and to understand how these very mechanisms are perturbed in disease. Here, we present the structural characterization of two protein complexes which are important regulators of cell signaling: PEAK3/14-3-3 and PI3Kα/KRas. We reveal that the dimeric PEAK3 scaffold associates with 14-3-3 in a unique asymmetric binding mode stabilized by a canonical phosphosite-dependent primary interface and an unusual secondary interface not seen in previous 14-3-3/client complexes. The secondary interface, which is largely stabilized by the SHED domain of PEAK3, explains why PEAK3 dimerization is essential for its scaffolding function. Additionally, we show that 14-3-3 sequesters PEAK3 in the cytosol, where it further modulates PEAK3's interactome. We also elucidate membrane-bound structures of the lipid kinase PI3Kα in complex with KRas, revealing dynamic changes in PI3Kα during activation. Our structures demonstrate that when bound to POPC/POPS membranes, PI3Kα adopts three distinct conformations which model various stages of its activation trajectory. When bound to PIP2-containing membranes, the orientation of PI3Kα relative to the membrane changes significantly,

tightly aligning its active site with the membrane and inducing conformational changes in key regulatory motifs. Most remarkably, the addition of an activating phosphopeptide induces dimerization of the PI3Kα/KRas complex, which is facilitated by an interface that is sterically occluded in auto-inhibited PI3Kα. Together, our studies provide the first structural characterization of the PEAK3/14-3-3 and PI3Kα/KRas complexes, offering mechanistic insights into their roles as regulators of cell migration and survival, respectively.

TABLE OF CONTENTS

Chapter 1: Structural and functional characterization of the PEAK3/14-3-3 complex..... 1

Abstract..... 2

Introduction..... 3

Results..... 7

Discussion..... 39

Materials and methods..... 44

References..... 55

Chapter 2: Structural characterization of the PI3Kα/KRas complex on membranes..... 64

Abstract..... 65

Introduction..... 66

Results..... 68

Discussion..... 88

Materials and methods..... 92

References..... 98

LIST OF FIGURES

Chapter 1

Figure 1.1: Structure of the PEAK3/14-3-3 complex 8

Figure 1.2: Mass spectrometry analysis of the purified PEAK3/14-3-3 complex 9

Figure 1.3: Putative 14-3-3 binding sites in PEAK family members 10

Figure 1.4: Processing workflow, resolution estimation and map quality of PEAK3/14-3-3 complex and PEAK3 homodimer dataset 12

Figure 1.5: Q-score analysis of the PEAK3/14-3-3 cryo-EM structure 13

Figure 1.6: Low-resolution structure of the PEAK3 homodimer 14

Figure 1.7: PEAK3 oligomerization 15

Figure 1.8: Identification of 14-3-3 isoforms in PEAK3/14-3-3 complex 17

Figure 1.9: SHED-dependent dimerization of PEAK3 20

Figure 1.10: Asymmetric binding mode of the PEAK3/14-3-3 complex 23

Figure 1.11: Structural analysis of PEAK3's specificity for 14-3-3ε 25

Figure 1.12: Unique features of the PEAK3 pseudokinase domain 28

Figure 1.13: PEAK3 homodimerization and both 14-3-3 binding interfaces are critical for PEAK3/14-3-3 complex formation 30

Figure 1.14: A phosphomimetic substitution at S69 does not reproduce the PEAK3/14-3-3 interaction 31

Figure 1.15: 14-3-3 influences cellular localization and scaffolding range of PEAK3 34

Figure 1.16: PKD regulates the PEAK3/14-3-3 interaction 37

Figure 1.17: Allosteric inhibition of PKD regulates the PEAK3/14-3-3 interaction 38

Chapter 2

Figure 2.1: In-vitro reconstitution of the PI3Kα/KRas complex bound to POPC/POPS membranes 69

Figure 2.2: Resolution estimation, map quality and processing workflow for the POPC/POPS-PI3Kα/KRas complex dataset 71

Figure 2.3: Multi-state structures of the PI3Kα/KRas complex bound to POPC/POPS membranes 72

Figure 2.4: Confirmational rearrangements and increased dynamics within the PI3Kα active site upon binding to KRas and POPC/POPS membranes 74

Figure 2.5: Comparison of the PI3Kα/KRas and PI3Kγ/HRas interfaces 76

Figure 2.6: In-vitro reconstitution of the PI3Kα/KRas complex bound to POPC/POPS/PIP2 membranes 78

Figure 2.7: Resolution estimation, map quality and processing workflow for the POPC/POPS/PIP2-PI3Kα/KRas complex dataset 79

Figure 2.8: PIP2 remodels the active site of PI3Kα 81

Figure 2.9: In-vitro reconstitution of the PI3Kα/KRas/peptide complex bound to POPC/POPS/PIP2 membranes 82

Figure 2.10: Resolution estimation, map quality and processing workflow for the POPC/POPS/PIP2-PI3Kα/KRas/peptide complex dataset 83

Figure 2.11: Phosphopeptide binding induces p110α-mediated dimerization of the PI3Kα/KRas complex 85

Figure 2.12: Dynamic membrane insertion of Ras 87

LIST OF ABBREVIATIONS

ABD	Adaptor binding domain
AML	Acute myeloid leukemia
BSA	Buried surface area
Cryo-EM	Cryo-electron microscopy
Csk	C-terminal Src kinase
CTF	Contrast transfer function
EV	Empty vector
GO	Graphene-oxide
MS	Mass-spectrometry
MSP	Membrane scaffold protein
NKF3	New Kinase Family 3
PDB	Protein data bank
PEAK	Pseudopodium enriched atypical kinase
PEST	Proline, glutamine, serine, threonine
PI3K	Phosphoinositide 3-kinase
PIP2	Phosphatidylinositol (4,5)-bisphosphate
PIP3	Phosphatidylinositol (3,4,5)-trisphosphate
POPC	1-palmitoyl-2-oleoyl-glycero-3-phosphocholine
POPS	1-palmitoyl-2-oleoyl-sn-glycero-3-phospho-L-serine
RBD	Ras binding domain
RTK	Receptor tyrosine kinase
SAXS	Small angle x-ray scattering

SEC	Size exclusion chromatography
SHED	Split helical dimerization domain
WT	Wild-type

Chapter 1: Structural and functional characterization of the PEAK3/14-3-3 complex

ABSTRACT

PEAK pseudokinases are molecular scaffolds which dimerize to regulate cell migration, morphology, and proliferation, as well as cancer progression. The mechanistic role dimerization plays in PEAK scaffolding remains unclear, as there are no structures of PEAKs in complex with their interactors. Here, we report the cryo-EM structure of dimeric PEAK3 in complex with an endogenous 14-3-3 heterodimer. Our structure reveals an asymmetric binding mode between PEAK3 and 14-3-3 stabilized by one pseudokinase domain and the SHED domain of the PEAK3 dimer. The binding interface contains a canonical phosphosite-dependent primary interaction and a unique secondary interaction not observed in previous structures of 14-3-3/client complexes. Additionally, we show that PKD regulates PEAK3/14-3-3 binding, which when prevented leads to PEAK3 nuclear enrichment and distinct protein-protein interactions. Altogether, our data demonstrate that PEAK3 dimerization forms an unusual secondary interface for 14-3-3 binding, facilitating 14-3-3 regulation of PEAK3 localization and interactome diversity.

INTRODUCTION

By catalyzing phosphorylation, protein kinases play important roles in regulating essential cellular processes such as cell survival, proliferation, migration, and organogenesis[7-10]. However, a significant subset of human kinases, termed pseudokinases, lack this vital enzymatic function due to the presence of inactivating mutations within key catalytic motifs. Instead, these catalytically inactive kinases have evolved other functionalities to propagate signaling, including allosteric modulation and scaffolding of their interaction partners[11,12]. Although pseudokinases are increasingly recognized as essential regulators of cellular signal transduction, the molecular mechanisms of most of their non-canonical kinase functions remain poorly understood.

The pseudopodium enriched atypical kinase (PEAK) family of pseudokinases, also known as New Kinase Family 3 (NKF3), is composed of three members: PEAK1 (also known as Sugen kinase [SgK] 269), PEAK2 (also known as Pragmin or SgK223), and PEAK3 (also known as chromosome 19 Open Reading Frame 35 [C19orf35]). The three PEAKs act as molecular scaffolds in pathways involved primarily in cell motility and migration[13,14]. PEAK1 overexpression increases cell motility and migration, likely due to a combination of a PEAK1-dependent increase in ERK signaling and through an ERK-independent mechanism via direct association of PEAK1 with the Src/p130Cas/Crk complex[15,16]. Notably, PEAK1 has been shown to be important for modulation of the late phase of EGF-induced EGFR signaling via its interaction with Shc1[17]. PEAK1 binding to Shc1 results in a switch in the Shc1-associated proteome from factors involved in pro-mitogenic and pro-survival signaling to proteins involved in cytoskeletal reorganization, migration, and eventually signal termination[17]. PEAK2 was initially found to increase RhoA signaling by interacting with the Rho family GTPase Rnd2, resulting in inhibition of neurite outgrowth[18]. However, in epithelial cells, PEAK2 activity

induces cell growth upon binding the C-terminal Src kinase (Csk), as a result of Src-dependent phosphorylation[9,10]. PEAK2/Csk binding increases Csk localization and activity at focal adhesions, inducing cell elongation and motility[19,20]. The emerging understanding of PEAK family signaling is that PEAKs regulate distinct cellular outcomes by selectively engaging their interaction partners.

PEAK3, the newest member of the PEAK pseudokinase family, and most distinct in its primary sequence, remained unannotated as a kinase until recently, and its functional characterization lags behind PEAK1 and PEAK2[21,22]. In fibroblast cells, PEAK3 was found to directly interact with CrkII and inhibit CrkII-dependent membrane ruffling[21,22]. Similar to what has been observed for PEAK2, the function of PEAK3 is cell type-dependent. In contrast to its effect on fibroblast cells, PEAK3 overexpression in epithelial cells was shown to increase cell motility and invasion[23]. These effects may be attributed to the multi-scaffolding capacity of PEAK3, since it interacts with a diverse set of signaling proteins, including Grb2, CrkII, Cbl, PYK2, ASAP1, and EGFR[23,24]. Reminiscent of the signal switching effect that PEAK1 has on the EGF-induced Shc1 proteome, the PEAK3 interactome is also altered by EGF stimulation, suggesting that PEAK3 has a dynamic role in signaling[23]. Importantly, in osteosarcoma and acute myeloid leukemia (AML) cell lines, overexpression of PEAK3 results in elevated AKT activity and increased cell growth[24].

The three PEAKs have a similar domain architecture, composed of an unstructured N-terminal domain followed by a pseudokinase domain[25]. The N-terminal domain contains a PEST linker (Proline, Glutamate, Serine, Threonine-rich region), which houses numerous consensus binding motifs, including those for SH2, SH3, and PTB domains. Interestingly, the N-terminal domain of PEAK3 is approximately one-tenth the length of the N-terminal domains of PEAK1

and PEAK2 (130 residues in PEAK3 vs 1282 residues in PEAK1 and 947 residues in PEAK2). All PEAKs have been shown to utilize their N-terminal domains for scaffolding, but the underlying molecular mechanisms are poorly understood. The pseudokinase domains in all three PEAKs have highly conserved helical regions adjoining both their N- and C-termini[21,22,26,27]. Crystal structures of truncated PEAK1 and PEAK2 lacking the unstructured N-terminal domains revealed that these pseudokinase domain-flanking helices fold into an "XL"-shaped helical bundle and facilitate dimerization by forming an "XX"-shaped high-affinity dimerization interface termed the Split HElical Dimerization (SHED) domain. All three PEAKs have been shown to homo- and heterodimerize in co-immunoprecipitation studies, with the pseudokinase and SHED domains being essential for these interactions[22,23,28]. The importance of this novel dimerization interface is reflected in the findings that binding of nearly all identified PEAK interaction partners is dependent on the ability of PEAK pseudokinases to dimerize[22,23,28].

PEAKs are classified as pseudokinases due to substitutions in key catalytic motifs, including mutation of the DFG motif in PEAK1 and PEAK2 and of the HRD motif in PEAK1 and PEAK3. Crystal structures of PEAK1 and PEAK2 illustrate how these unique sequence features contribute to the lack of PEAK1 and PEAK2 catalytic activity. In these structures, the putative nucleotide-binding pockets of PEAK1 and PEAK2 are partially collapsed and occluded by bulky hydrophobic side chains, preventing nucleotide binding[21,26,27]. Due to sequence deviations in PEAK3 and the lack of PEAK3 structures, it has not been clear whether PEAK3 adopts a similar architecture. An intact DFG motif in PEAK3, as well as the presence of a conserved "catalytic lysine" with its potential salt bridge partner (a glutamate located in the predicted αC helix), presented the possibility that the nucleotide binding capability of PEAK3 might deviate from its family members.

In this study, we use cryo-electron microscopy (cryo-EM) to obtain the first structural insights into PEAK3 and the mechanisms that mediate its protein-protein interactions. Strikingly, full-length human PEAK3 purifies from mammalian cells as a homodimer in complex with an endogenous 14-3-3 heterodimer, and we have obtained a 3.1 Å structure of this complex. 14-3-3s are ubiquitous regulatory proteins that act as dimeric scaffolds to modulate their client proteins through a wide array of mechanisms, such as altering protein-protein interactions, inducing conformational changes, regulating subcellular localization, and sterically blocking access to phosphorylation sites[29-32]. This has recently been exquisitely demonstrated in high resolution cryo-EM structural studies of 14-3-3s in complex with RAF and MEK kinases[33,34]. In our PEAK3 structure, key structural kinase elements, the αC helix and the activation loop, are fully resolved, in contrast to previous structures of PEAK1 and PEAK2. The N-terminal domain of PEAK3 is largely disordered, with the exception of the phosphorylated 14-3-3 binding motifs of each PEAK3 monomer that interact with each 14-3-3 monomer. Most remarkably, our structure reveals a unique secondary interface between the PEAK3 and 14-3-3 dimers that has not been previously observed in other structures of 14-3-3/client complexes. Analysis of the PEAK3/14-3-3 complex by mutagenesis demonstrates how this interaction regulates PEAK3 subcellular localization and the expansiveness of its cellular interactome.

RESULTS

Structure of the PEAK3/14-3-3 complex

The long, unstructured N-terminal domains of PEAK1 and PEAK2 make it challenging to express them as recombinant full-length proteins for structural studies by X-ray crystallography[15]. We succeeded in expressing the much shorter full-length PEAK3 in mammalian Expi293F cells and purifying it for cryo-EM studies. Following affinity purification, FLAG-tagged full-length PEAK3 remained associated with a ~ 30 kDa doublet band, which we determined to be a mixture of 14-3-3 proteins by mass spectrometry (MS) **(Fig. 1.1 a, b; Fig. 1.2 a, b)**. A primary sequence analysis of PEAK3 revealed the presence of a putative 14-3-3 consensus binding motif within the N-terminal domain of PEAK3 (RTQSLP, residues 66-71) **(Fig. 1.1 c; Fig. 1.3 a)**, which is highly conserved in evolution **(Fig. 1.1 d)**[2].

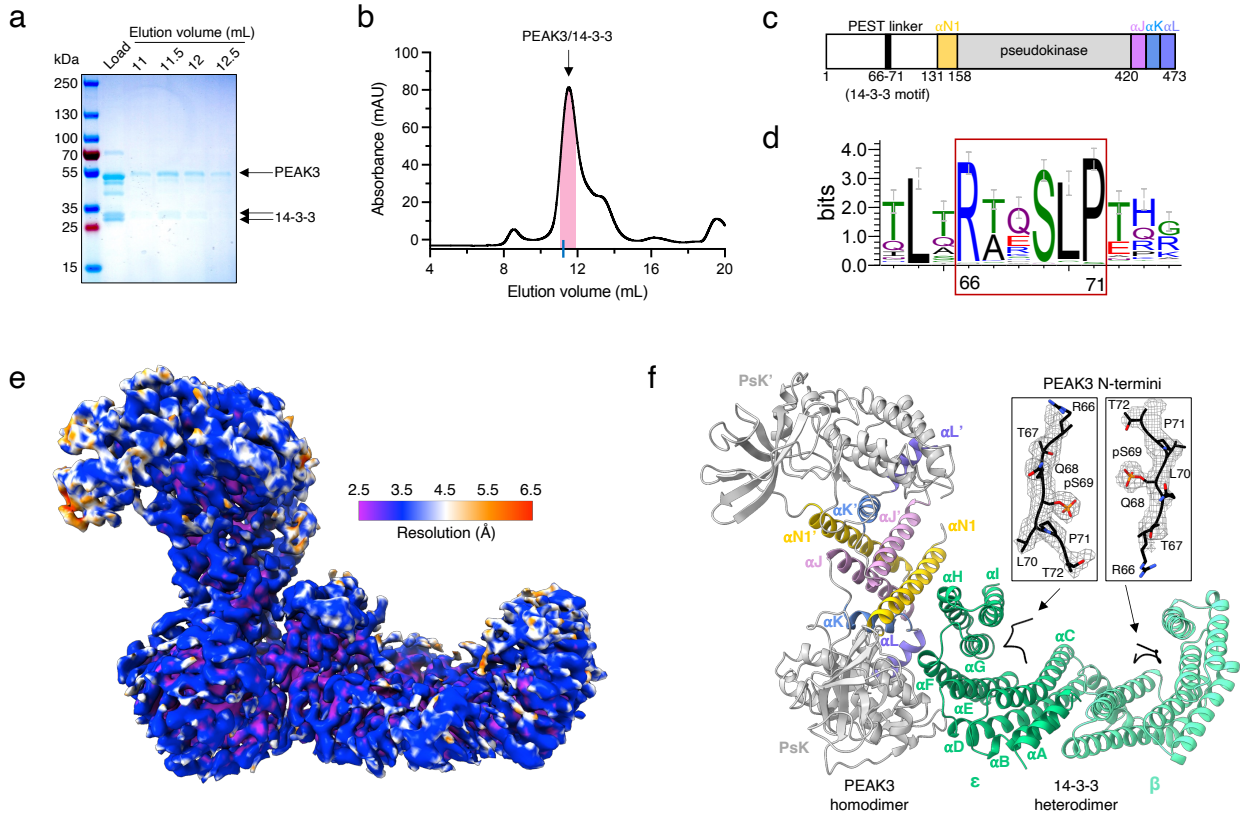


Figure 1.1: Structure of the PEAK3/14-3-3 complex

a Representative Coomassie-stained SDS-PAGE gel analysis of the purified PEAK3/14-3-3 complex and **b** corresponding size exclusion chromatography profile resolved on a Superdex 200 10/300 Increase column. Pink bar on the chromatogram indicates collected fractions. Blue tick on the x-axis represents the elution volume of Bovine γ-globulin (158,000 Da) as a reference for the PEAK3/14-3-3 tetrameric complex (161,801 Da). SDS-PAGE and size exclusion chromatography results are representative of at least 3 independent experiments. **c** Cartoon schematic of PEAK3 domain structure depicting location of the 14-3-3 binding site. **d** Sequence logo (Weblogo) demonstrating conservation of the 14-3-3 binding site in PEAK3 across evolution. PEAK3 homolog sequences were collected by BLAST search in the Refseq database and clustered at 80% sequence identity. **e** Cryo-EM map of the PEAK3/14-3-3 complex colored according to local resolution determined by ResMap. **f** Structure of the PEAK3/14-3-3 complex and zoomed-in view of PEAK3 N-terminal 14-3-3 consensus binding sites superimposed with the cryo-EM map, demonstrating occupancy of both canonical substrate binding grooves in 14-3-3 by phosphorylated 14-3-3 consensus sequences of PEAK3. PEAK3 pseudokinase domains (PsK and PsK') are in gray and the resolved regions of the N-terminal PEST linkers are shown in black. SHED domain helices αN1 are in yellow, αJ in pink, αK in blue, and αL in purple. 14-3-3ε is shown in green and 14-3-3β is shown in light green.

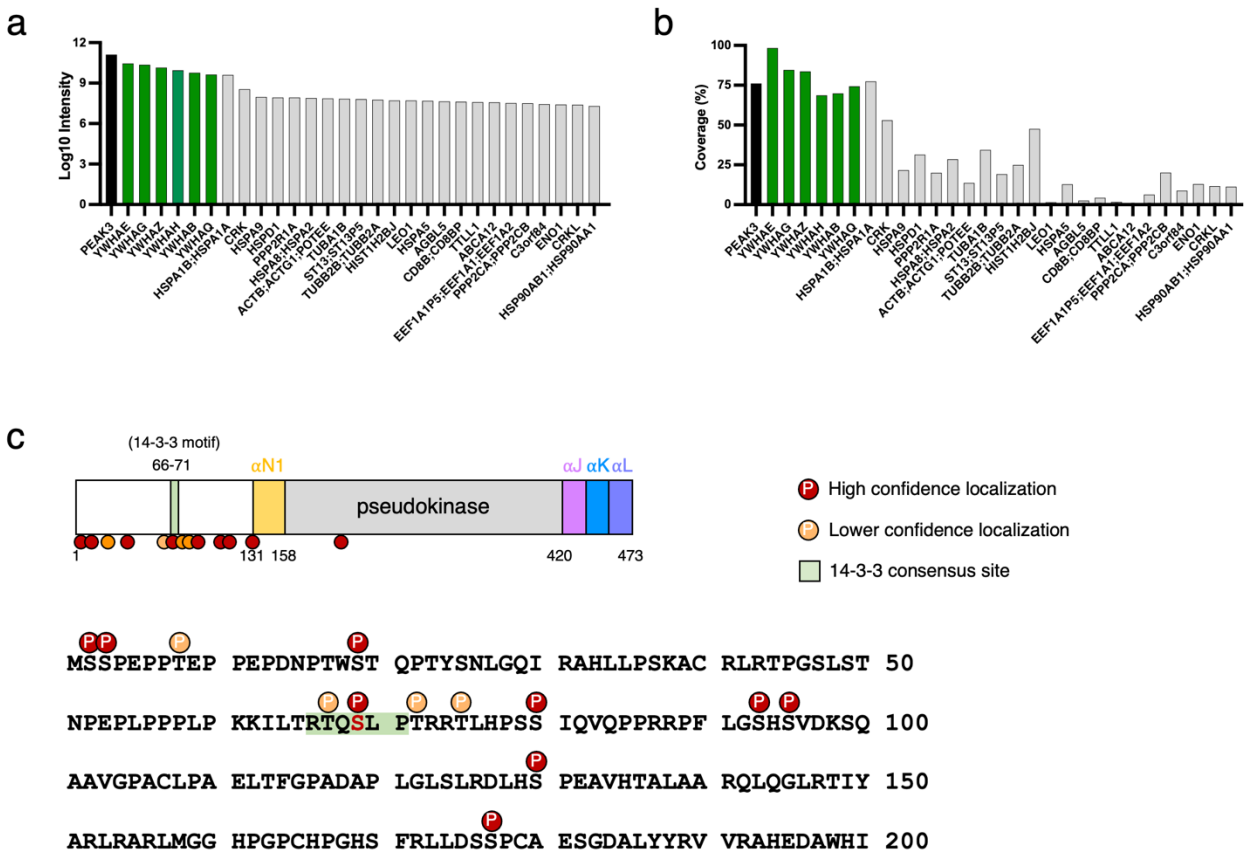


Figure 1.2: Mass spectrometry analysis of the purified PEAK3/14-3-3 complex
a Bar chart representing the log10 protein spectral intensity for the top 30 proteins identified by mass spectrometry (MS) analysis of the purified PEAK3/14-3-3 complex, and **b** their corresponding protein sequence coverage (black: PEAK3, green: 14-3-3, gray: other interactors). **c** Schematic representation of the identified phospho-sites in PEAK3 by MS analysis (red: localization probability > 0.8; orange: localization probability < 0.8). The S69 phospho-site within the 14-3-3 consensus binding site (green) of PEAK3 represents a high confidence site.

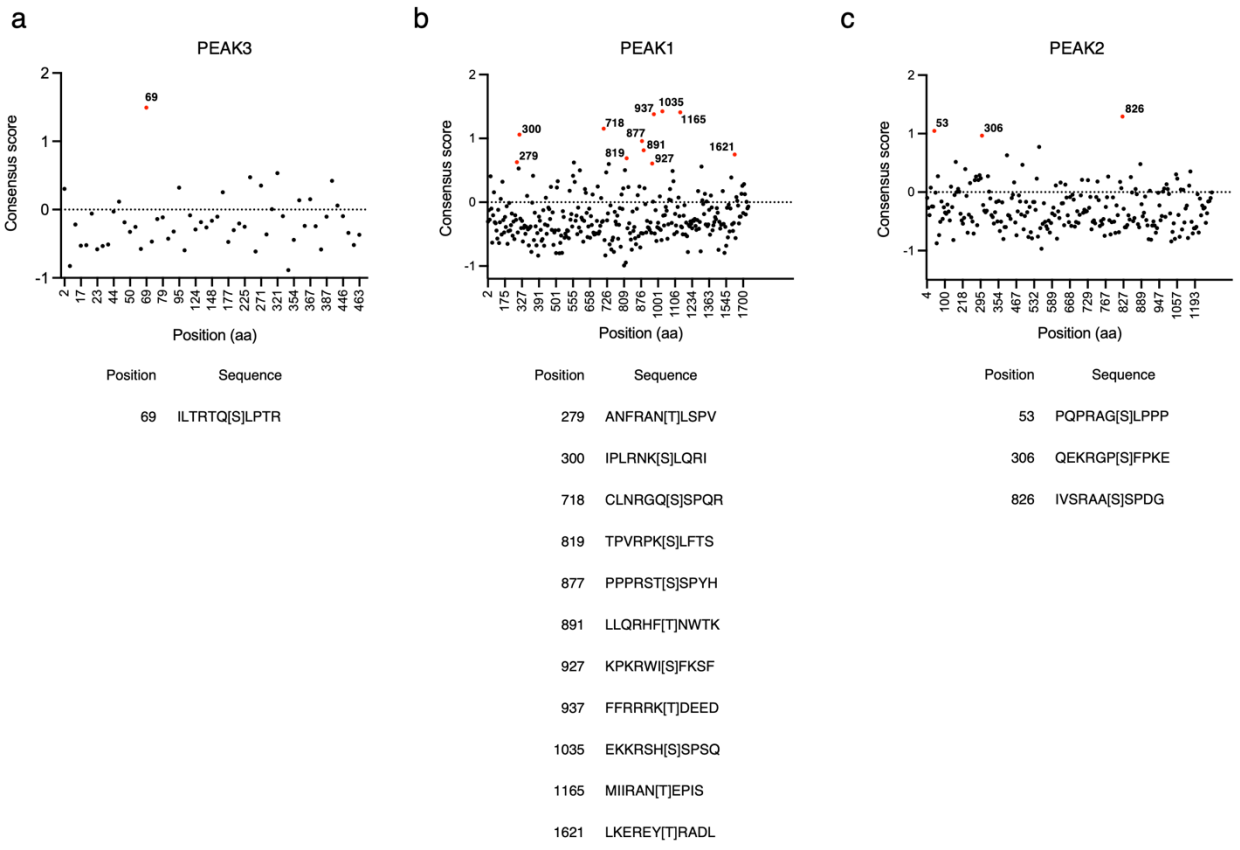


Figure 1.3: Putative 14-3-3 binding sites in PEAK family members

a-c Sequence-based prediction of 14-3-3 consensus binding sites in PEAK family members using the 14-3-3-Pred webserver[2] based on three different classifiers (ANN, PSSM and SVM). Data points represent the amino acid position of the phosphorylated serine or threonine within the putative binding site. Sites, which score highly in all three prediction models, are colored red.

We observed both PEAK3/14-3-3 complex and PEAK3 homodimer particles in the cryo-EM dataset; however, these particles exhibited orientation bias which limited our ability to reconstruct high resolution maps. The addition of 0.1% n-Octyl-β-D-glucoside to the sample prior to plunge freezing alleviated preferred orientation, and selective processing of the PEAK3/14-3-3 complex particles in CryoSPARC yielded a 3.1 Å structure of the PEAK3 homodimer bound to a 14-3-3 heterodimer **(Fig. 1.1 e; Fig. 1.4; Fig. 1.5)**. The addition of detergent to combat the orientation bias required us to work in a higher protein concentration regime, which shifted the particle equilibrium toward the complex, limiting the number of PEAK3-only particles. Nevertheless, the available PEAK3-only particles were initially processed in CryoSPARC and then re-extracted and imported to RELION for 3D classification and refinement to further alleviate streaking artifacts common for samples with preferred orientation. This yielded a low-resolution (4.9 Å) reconstruction of the PEAK3 homodimer **(Fig. 1.4; Fig. 1.6 a)**. The limited resolution could be due to the low number of particles in the resulting reconstruction (32,734), especially impactful for a protein of this small size (108,034 Da). Another possibility is that the apo-PEAK3 homodimer exhibits conformational flexibility that is reduced upon 14-3-3 binding. Globally, however, comparison of the PEAK3/14-3-3 structure with the low-resolution structure of the PEAK3 homodimer alone did not reveal major differences within the PEAK3 dimer, with an overall average RMSD of 0.623 Å **(Fig. 1.6 b)**.

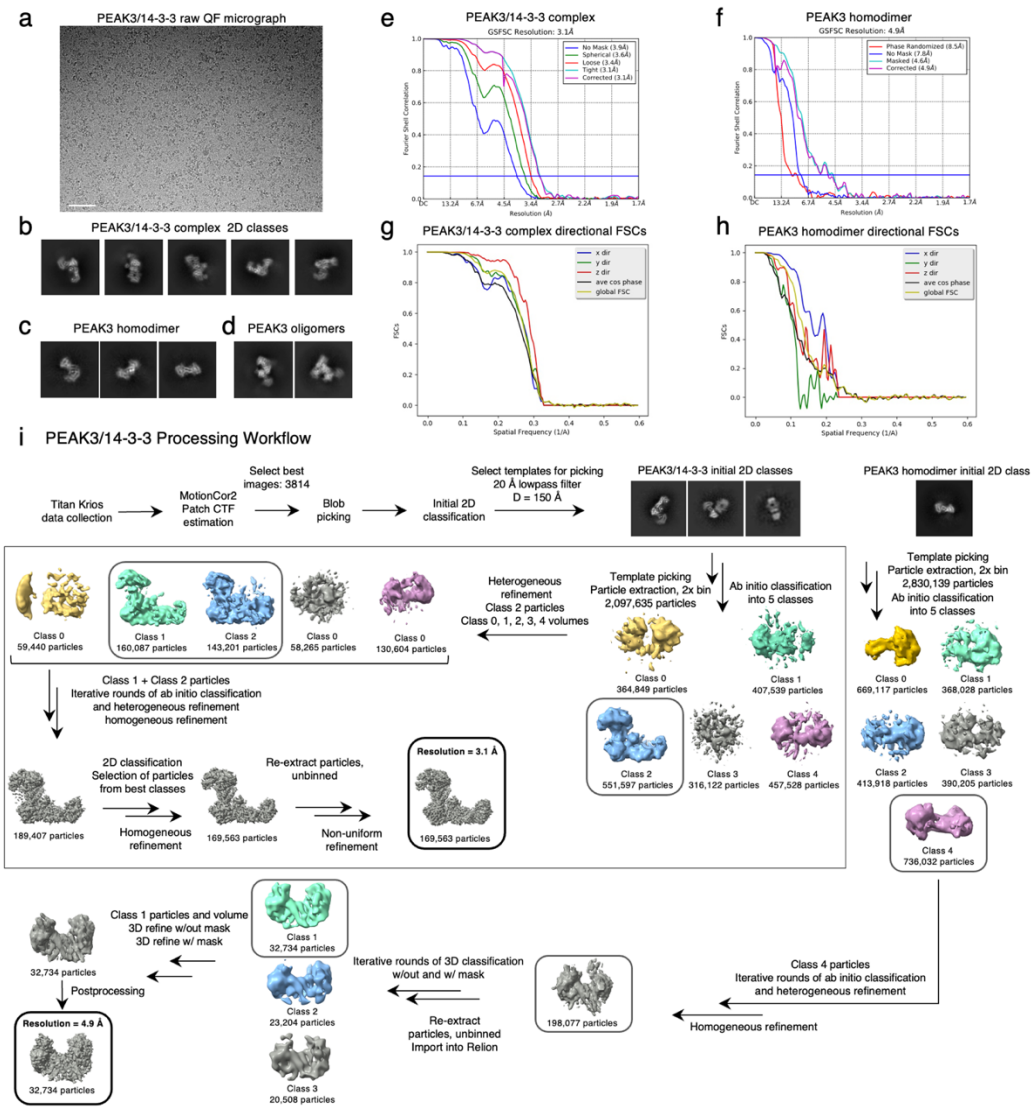


Figure 1.4: Processing workflow, resolution estimation and map quality of PEAK3/14-3-3 complex and PEAK3 homodimer dataset

a Representative micrograph of the PEAK3/14-3-3 complex sample on Quantifoil R1.2/1.3 300 mesh Au holey-carbon grids, from a dataset with 3814 micrographs. The scale bar corresponds to 500 Å. **b-d** Example cryo-EM 2D class averages of particles corresponding to (**b)** PEAK3/14-3-3 complex, (**c)** PEAK3 homodimer, and (**d)** PEAK3 oligomers in the absence or presence of 14-3-3 binding. **e,f** Gold Standard Fourier Shell Correlation (GSFSC) of the final map used for model building of the (**e**) PEAK3/14-3-3 complex from CryoSPARC[4] with a reported resolution of 3.1 Å and final map for model building of the (**f**) PEAK3 homodimer from RELION[5] with a reported resolution of 4.9 Å. **g,h** Directional FSCs of the (**g**) PEAK3/14-3-3 complex and the (**h**) PEAK3 homodimer calculated by 3DFSC server[6]. **i** Workflow for processing the PEAK3/14-3-3 complex dataset. Gray boxes indicate model and associated particle stack used for downstream processing. The final model is indicated with a bolded black box.

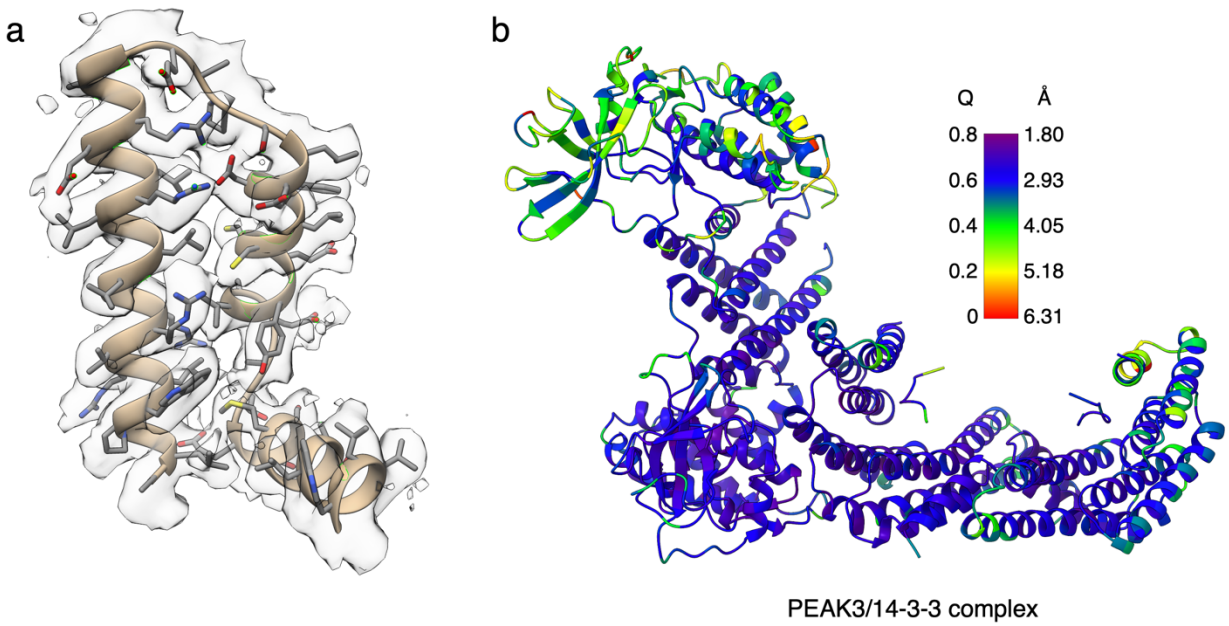


Figure 1.5: Q-score analysis of the PEAK3/14-3-3 cryo-EM structure
a Zoomed-in view of the cryo-EM map and corresponding model of the PEAK3/14-3-3 complex (residues 419-472) demonstrating features appropriate for reported resolution. **b** PEAK3/14-3-3 complex model colored by estimated per residue Q-score. Color scale bar indicates corresponding estimated resolution in Å for reported Q-scores. Expected Q-score for a 3.1 Å structure is 0.569.

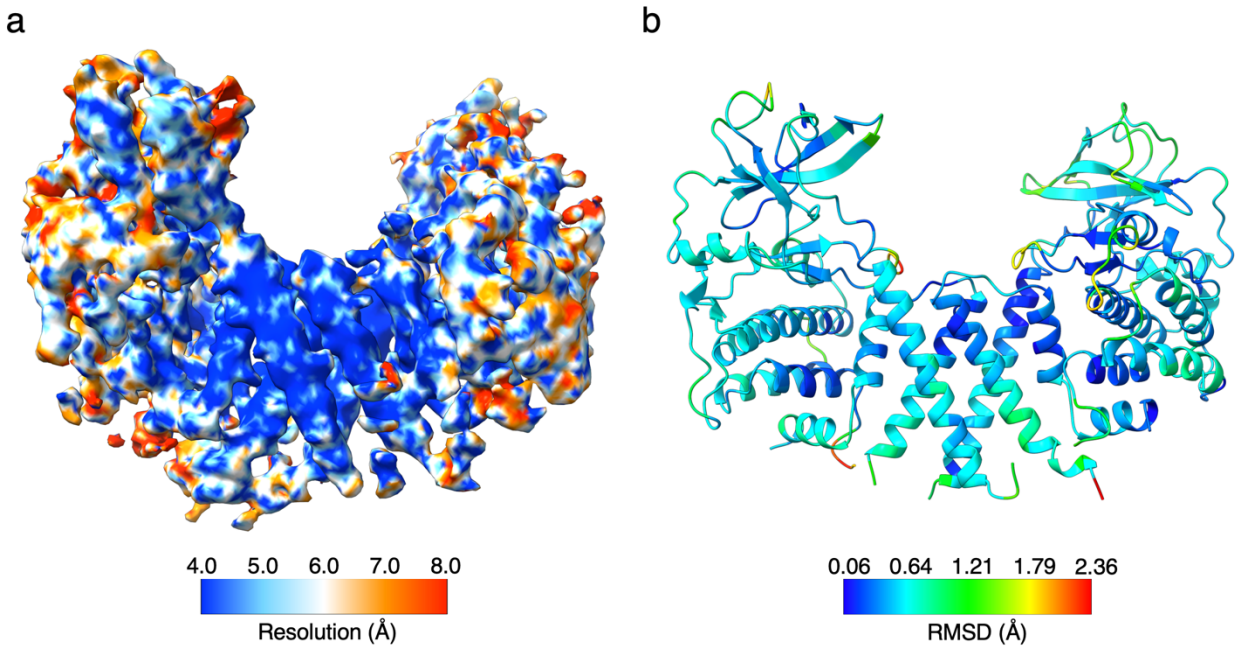


Figure 1.6: Low-resolution structure of the PEAK3 homodimer
a Cryo-EM map of the PEAK3 homodimer colored according to local resolution determined by ResMap[1]. **b** Corresponding model of the PEAK3 homodimer structure colored by per residue Root Mean Square Deviation (RMSD, Å) relative to PEAK3 homodimer as part of the PEAK3/14-3-3 complex.

Previously, PEAK1 and PEAK2 pseudokinase dimers have been shown to organize into higher-order oligomers[27,28]. Concordant with this, a subset of 2D class averages in our PEAK3/14-3-3 cryo-EM dataset was also consistent with higher-order PEAK3 oligomers, both in the absence and presence of 14-3-3 **(Fig. 1.7 a, b)**. However, the particle counts for these complexes were too low to enable 3D reconstructions. To investigate if such oligomeric complexes of PEAK3 could form using the same interface observed in PEAK2, and presumably in PEAK1, even in the presence of 14-3-3 binding, we built structural models of PEAK3 oligomers using the interface observed in the crystal structure of PEAK2[27]. This analysis revealed that the PEAK3 dimer is able to engage both 14-3-3 and another PEAK3 dimer simultaneously via the same monomer or different monomers without steric clashes **(Fig. 1.7 c)**.

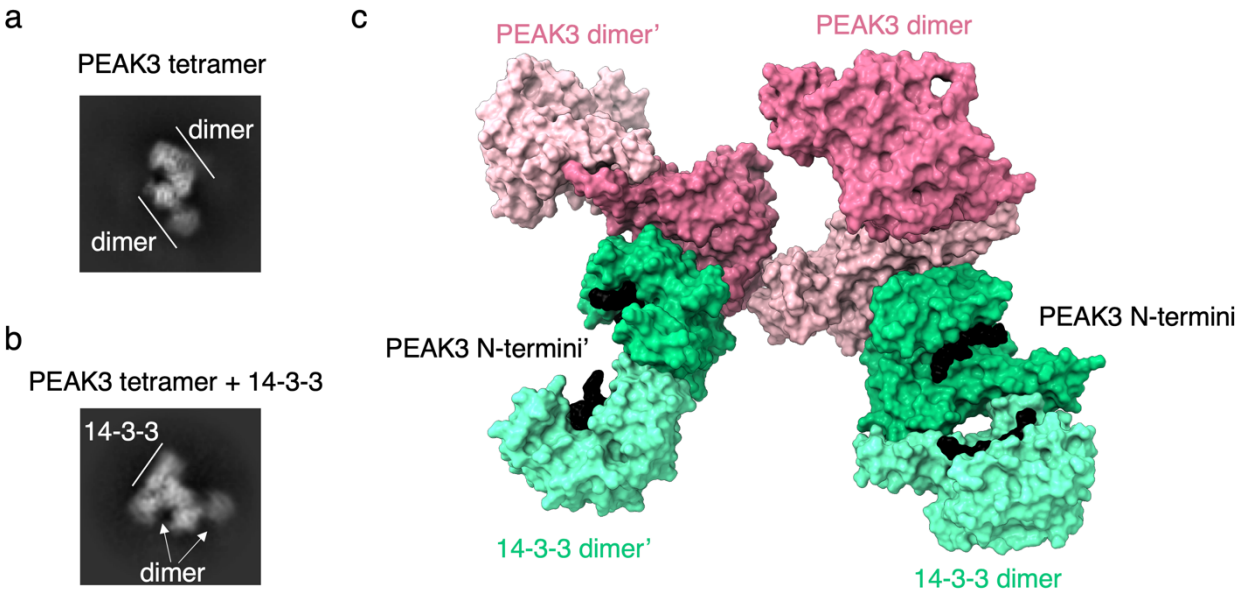


Figure 1.7: PEAK3 oligomerization
a,b PEAK3 oligomerization in the absence (**a**) and presence (**b**) of 14-3-3 binding as demonstrated by cryo-EM 2D class averages. **c** Putative oligomeric PEAK3/14-3-3 complex model derived from oligomeric interface identified from crystal packing of PEAK2 crystal structure (PDB ID: 5VE6). PEAK3 homodimer within the PEAK3/14-3-3 complex was first aligned with one of the two PEAK2 homodimers, followed by alignment of a second PEAK3 homodimer to the second PEAK2 homodimer.

MS analysis of the purified PEAK3/14-3-3 complex used for cryo-EM identified six of the seven isoforms of human 14-3-3 (β, γ, ε, η, θ, and ζ) **(Fig 1.2 a, b)** and phosphorylation of the Ser 69 residue within the 14-3-3 binding motif of PEAK3 **(Fig. 1.2 c**). In the cryo-EM map, the phosphorylated Ser 69 was clearly identifiable in both 14-3-3 binding grooves **(Fig. 1.1 f)**, allowing us to manually build the neighboring peptide sequences (RTQS^{69}LP), presumably coming from both N-terminal domains of the PEAK3 dimer. In the structure, the PEAK3 homodimer is docked to one side of the 14-3-3 dimer cradle, with only one monomer of PEAK3 forming an extensive interface with one of the 14-3-3 monomers, yielding a buried surface area (BSA) of ~1453 Å^2 **(Fig. 1.1 f)**. Based on the cryo-EM map, we were able to unambiguously identify this 14-3-3 monomer as the ε isoform (**Fig. 1.8 a-g)**, while the distal 14-3-3 monomer was most consistent with the β isoform **(Fig. 1.8 h-n)**. Because MS analysis identified multiple 14-3-3 isoforms, all of which exhibit high sequence conservation, we cannot rule out a mixture of 14-3-3 isoforms in the β monomer density. Nevertheless, our final model was constructed with the ε and β isoforms of 14-3-3, which most closely match the cryo-EM density. Although it has been well appreciated that 14-3-3ε preferentially heterodimerizes with other 14-3-3 isoforms rather than forming homodimers, likely due to the formation of an additional salt bridge at the dimerization interface[35], our structure provides the first high resolution experimental view of such a heterodimer. With the exception of the 14-3-3 binding motifs, discussed later, the remainder of the PEAK3 N-terminal domain of each monomer was not resolved, consistent with its predicted intrinsic flexibility **(Fig. 1.1 f)**[25].

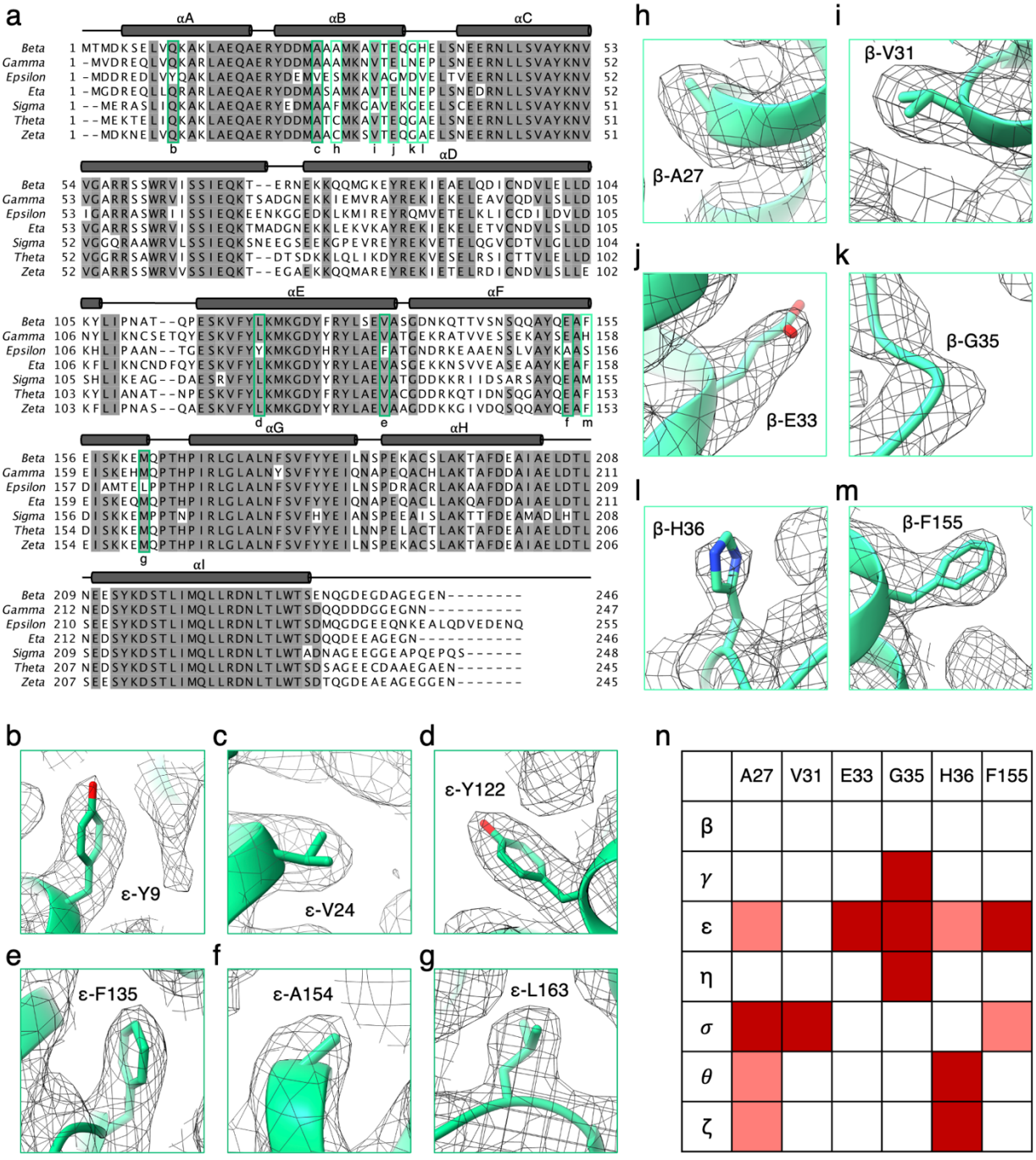


Figure 1.8: Identification of 14-3-3 isoforms in PEAK3/14-3-3 complex

a Structure-based sequence alignment of human 14-3-3 isoforms depicting their secondary structure elements. Conserved residues are shaded in gray. **b-m** Zoomed-in view of residue side chains in 14-3-3ε (**b-g**) and in 14-3-3β (**h-m**) overlayed with the cryo-EM map used to determine the identity of the 14-3-3 monomers in the PEAK3/14-3-3 structure. **n** Summary table of (**h-m**) residues and their compatibility with the cryo-EM map in all 14-3-3 isoforms. Dark red, light red and white squares indicate that the corresponding residue in a particular 14-3-3 isoform is not consistent, somewhat consistent or consistent with the cryo-EM density, respectively.

SHED-mediated dimerization is conserved in PEAK3

Similar to the previously seen dimerization poses of PEAK1 and PEAK2, in our structure, PEAK3 dimerizes via the "XL"-shaped helical bundles flanking each pseudokinase domain. Consistent with previous predictions based on sequence conservation and homology modeling[22], these individual "XL" helical bundles come together to form the canonical "XX"-shaped SHED domain, burying a total surface area of 2726 Å^2 **(Fig. 1.9 a)**. The "XL"-shaped helical bundle within each PEAK3 monomer is held together by a tightly packed network of hydrophobic interactions involving the αN1, αJ, αK, and αL helices, largely conserved in PEAK1 and PEAK2 **(Fig. 1.9 b)**. Notably, Leu 146 of the αN1 helix and Cys 453 of the αK helix contribute to this network. Individual mutation of these residues is sufficient to disrupt PEAK3 homo- and heterodimerization[22,23] and ablate its interaction with almost all identified binding partners[13,14]. The SHED domain is stabilized primarily via hydrophobic interactions between the αN1 and αJ helices of the two PEAK3 monomers **(Fig. 1.9 c)**. This interface contains Ala 436 on the αJ helix, mutation of which has also been shown to disrupt PEAK3 dimerization and its scaffolding functions[22,23].

Like in PEAK1 and PEAK2, SHED domain helices not only participate in the dimerization interface, but they also make extensive interactions with the pseudokinase domain of PEAK3 (**Fig. 1.9 d, e**). The N-lobe of the pseudokinase domain, specifically the αC-β4 loop Phe 228 (PEAK1: Phe 1385, PEAK2: Phe 1045), forms a hydrophobic contact with Trp 450 (PEAK1: Trp 1722, PEAK2: Trp 1382) of the αK helix. Trp 450 additionally links the αN1 helix to the β7-β8 loop of the N-lobe by positioning Leu 157 (PEAK1: Phe 1309, PEAK2: Phe 974) to interact with Cys 318 (PEAK1: unresolved, PEAK2: Cys 1156) **(Fig. 1.9 d)**. The C-lobe of the pseudokinase domain forms a more substantial interface with the αJ, αK, and αL helices of the

SHED domain. In particular, the αK residues, Cys 452 (PEAK1: Cys 1724, PEAK2: Cys 1384) and Glu 454 (PEAK1: Gln 1726, PEAK2: Gln 1386), form hydrophobic and electrostatic contacts with Trp 400 (PEAK1: Trp 1668, PEAK2: Trp 1330) and Arg 392 (PEAK1: Lys 1660, PEAK2: Lys 1322) of the αI helix, respectively. In turn, Leu 398 (PEAK1: Leu 1666, PEAK2: Leu 1328) and Ala 397 (PEAK1: Cys 1665, PEAK2: Cys 1327) of the αI helix pack against Leu 471 (PEAK1: Leu 1743, PEAK2: Leu 1403) and Ala 467 (PEAK1: Ile 1739, PEAK2: Ser 1399) of the αL helix, while Pro 402 (PEAK1: Pro 1670, PEAK2: Pro 1332), located on the C-terminus of the pseudokinase domain, forms an additional hydrophobic contact with Trp 423 (PEAK1: Trp 1694, PEAK2: Trp 1354) of the αJ helix **(Fig. 1.9 e)**. The SHED domain in PEAK3 has the greatest rotation angle among all PEAK structures, and this rotation is caused by an outward movement of the αJ helix, which in turn forces the αL helix to rotate upwards **(Fig. 1.9 f)**. Consequently, the pseudokinase domain of PEAK3, which interfaces with the αL helix via its C-lobe, is pushed upward and to the back relative to PEAK1 and PEAK2, resulting in a more twisted overall architecture in the PEAK3 homodimer **(Fig. 1.9 g)**.

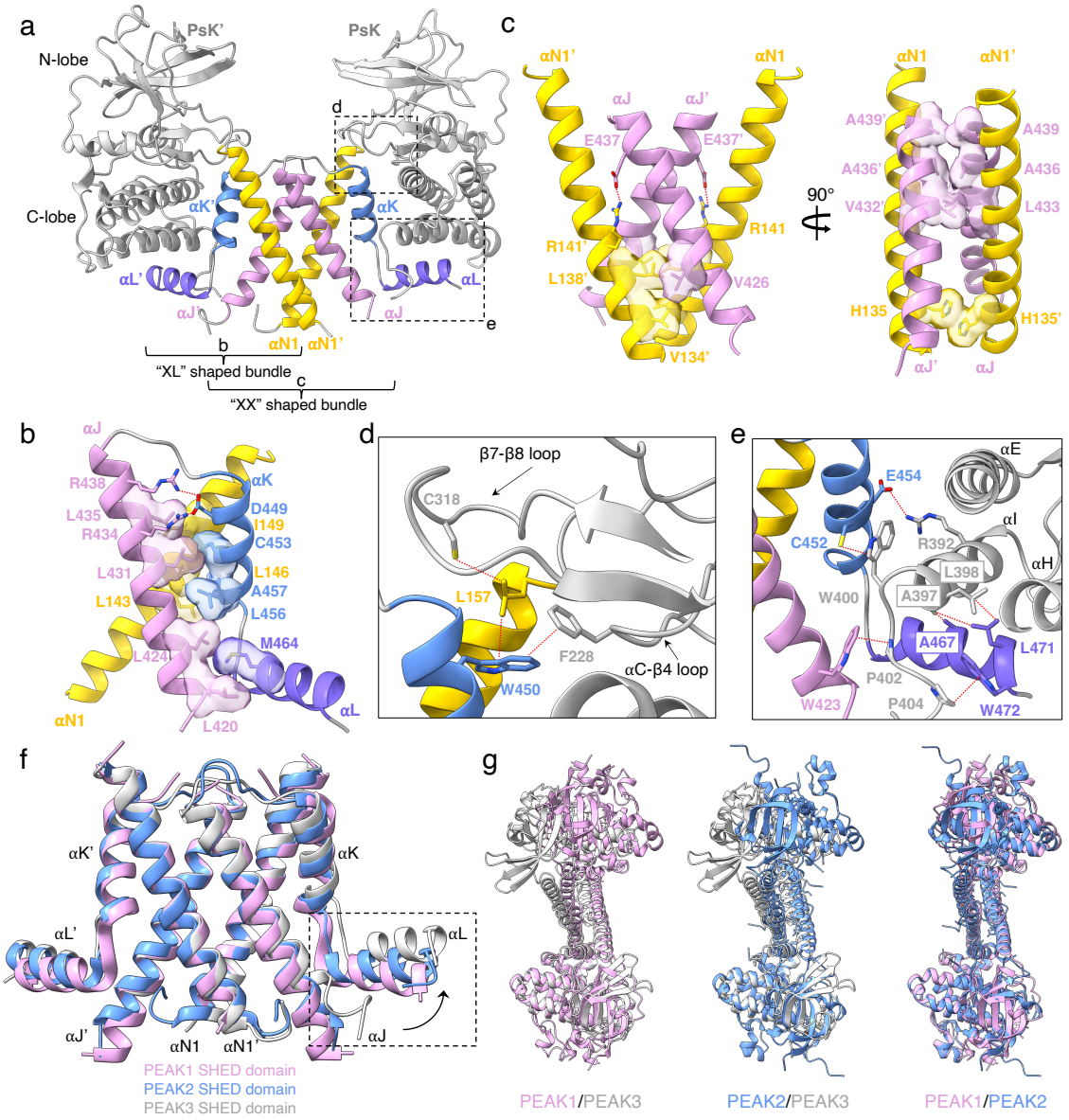


Figure 1.9: SHED-dependent dimerization of PEAK3

a Overall structure of the PEAK3 dimer as part of the PEAK3/14-3-3 complex (14-3-3 is not shown). **b** XL-shaped helical bundle of one PEAK3 monomer, highlighting intramolecular interactions. **c** Intermolecular interactions between helices αN1 and αJ of each PEAK3 monomer within the SHED dimer. **d,e** Zoomed-in views of the interactions between the SHED domain and pseudokinase/N-lobe (**d**) and pseudokinase/C-lobe (**e**). **f** Structural alignment of PEAK family SHED domains (PDB ID: 6BHC for PEAK1, and PDB ID: 5VE6 for PEAK2) along αN1 and αJ helices, depicting movement of αJ and αL helices in PEAK3 relative to their position in PEAK1 and PEAK2. **g** Overlay of the PEAK1 (PDB ID: 6BHC), PEAK2 (PDB ID: 5VE6) and PEAK3 dimer structures aligned along one pseudokinase domain (shown at the bottom of each overlay). Dashed lines in red indicate interactions with distances ≤ 4 Å.

Asymmetric binding mode of the PEAK3/14-3-3 complex

Binding of 14-3-3s to client proteins is typically mediated by two sets of contacts, termed the primary and secondary interactions **(Fig. 1.10 a)**[35]. The primary interaction involves binding of the client to the conserved amphipathic groove formed by the αI, αE, αG, and αC helices of 14-3-3 via a consensus 14-3-3 binding motif, which contains a phosphorylated serine or threonine residue[35]. The secondary interaction involves a larger interface between the globular domain of the client protein and 14-3-3[35]. Although the disordered N-terminal domain of PEAK3 is largely unresolved in our structure (residues 1-127), the cryo-EM map does contain robust density for the 14-3-3 primary interaction motif (residues 66-71), with clear density for the phosphate group of Ser 69 **(Fig. 1.1 f)**. The Ser 69 phosphate group forms contacts with the positively charged groove of 14-3-3, including the canonical Arg (ε-57/β-58), Arg (ε-130/β-129), Tyr (ε-131/β-130) triad as well as a Lys (ε-50/β-51) within the αE helix **(Fig. 1.10 b)**. The PEAK3/14-3-3 interaction maintains hydrogen bonding between the conserved residues of 14-3-3 (ε-Asn 176/β-Asn 175 and ε-Asn 227/β-Asn 226) and the backbones of Leu 70 and Gln 68 of PEAK3's consensus sequence, respectively **(Fig. 1.10 b)**.

The secondary interaction between PEAK3 and 14-3-3 in our model is quite unusual, because it is located outside of the 14-3-3 cradle. Only one monomer of 14-3-3 engages the PEAK3 dimer at this interface via helices αH, αE, and αF of 14-3-3ε **(Fig. 1.1 f).** This binding mode is distinct from any other 14-3-3/client complexes found in the Protein Data Bank (PDB), which can be sorted into two separate categories. The first has the client protein sitting within the cradle formed by the 14-3-3 dimer, interacting with the αI helix or both αI and αH helices of 14-3-3, as observed with the B-Raf/14-3-3 complex **(Fig. 1.10 c, left)**[33]. A second binding mode has the globular domains of the client sitting atop the sides of the 14-3-3 cradle, forming contacts

with both αI and αH helices, as seen in the Exoenzyme T/14-3-3 complex **(Fig. 1.10 c, middle)**[36]. To our knowledge, 14-3-3/client complexes where the dimeric client sits outside of the 14-3-3 cradle and the secondary interface only forms contacts with one 14-3-3 monomer, as observed in the PEAK3/14-3-3 complex **(Fig. 1.10 c, right)**, have never been captured in crystal structures.

The unique secondary interface in the PEAK3/14-3-3 complex is stabilized by several polar contacts between the SHED and the pseudokinase domain of PEAK3 and 14-3-3ε **(Fig. 1.10 d)**. Residues Gln 144 and Arg 147 of the αN1 helix within the SHED domain of PEAK3 form a hydrogen bond and a salt bridge with Asp 200 and Asp 201 belonging to the 14-3-3ε αH helix, respectively **(Fig. 1.10 e)**. Leu 146, a residue we and others have previously demonstrated to be important for PEAK3 dimerization[22,23], sits between Gln 144 and Arg 147, but faces inwards towards the SHED domain interface. Leu 146 makes hydrophobic contacts with Leu 431 and Val 432 of the αJ helix and Cys 453 of the αK helix, another residue involved in PEAK3 dimerization **(Fig. 1.10 e)**[22,23]. The close proximity of Gln 144 and Arg 147 to Leu 146 suggests that PEAK3 dimerization likely results in the proper positioning of Gln 144 and Arg 147 to interact with 14-3-3, increasing the affinity of the PEAK3/14-3-3 interaction. Several residues within the pseudokinase domain of PEAK3 also make polar contacts with 14-3-3ε. These include Ser 225 of the αC-β4 loop **(Fig. 1.10 f)**, which hydrogen bonds with Glu 162 of the αF helix of 14-3-3ε, as well as Lys 293 and Trp 298 **(Fig. 1.10 g, h)**, which sit on the αE helix of PEAK3 and interact with the αF helix Asp 157 and the αE helix Lys 118 of 14-3-3ε, respectively. This large interface contributed by the pseudokinase domain of PEAK3 likely stabilizes the unusual asymmetric interaction with 14-3-3ε.

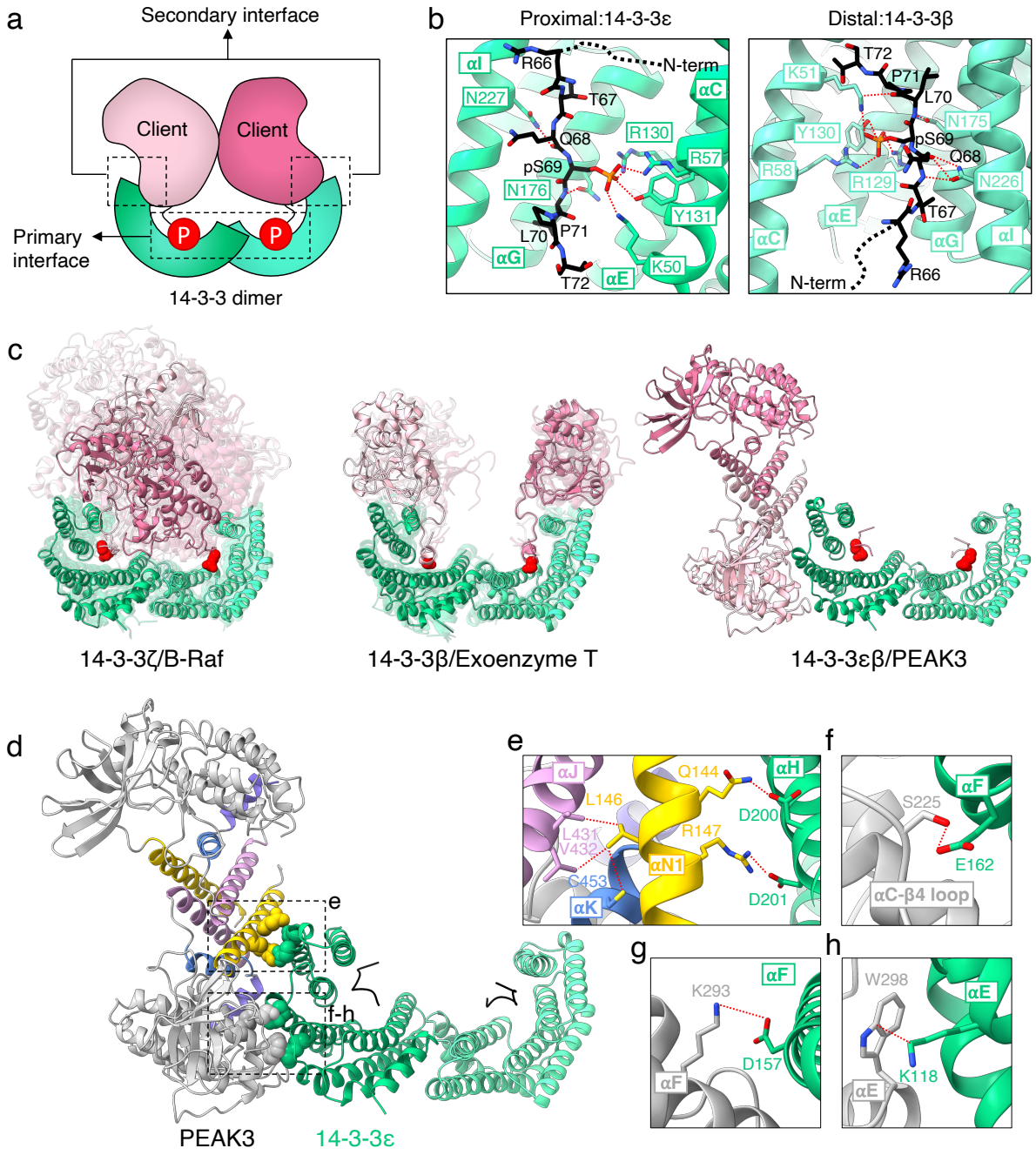


Figure 1.10: Asymmetric binding mode of the PEAK3/14-3-3 complex

a Cartoon depicting primary and secondary interactions within a 14-3-3/client complex. **b** PEAK3 binding to the amphipathic grooves of 14-3-3ε and 14-3-3β, highlighting key conserved interactions. **c** Known binding modes of 14-3-3/client complexes found in the Protein Data Bank. 14-3-3 monomers are shown in green and light green, 14-3-3 substrate monomers are shown in pink and light pink, and phosphorylated residues or phosphomimetics which engage the 14-3-3 binding grooves are shown as red spheres. See Methods for alignment details. **d** PEAK3/14-3-3 structure highlighting PEAK3 SHED domain (box e) and pseudokinase domain (box f-h) interactions with 14-3-3ε. **e-h** Zoomed-in view of PEAK3/14-3-3ε secondary interface, highlighting key interactions. Dashed lines in red indicate interactions with distances ≤ 4 Å.

To rationalize PEAK3's selectivity for 14-3-3ε over the remaining six isoforms, we first considered cellular localization patterns of 14-3-3 isoforms. Only ε, β, θ, and ζ isoforms have been shown to localize to the cytoplasm where PEAK3 is predominantly found[32]. To determine if a specific sequence of 14-3-3ε contributes to its binding to PEAK3, we flexibly fit, using Rosetta FastRelax protocol, structures of 14-3-3β[35], θ[37], and ζ[38] in place of 14-3-3ε into the PEAK3/14-3-3 cryo-EM volume. Both the primary and secondary interface residues of 14-3-3ε, which make important interactions with PEAK3, were highly conserved among β, θ, and ζ isoforms, failing to explain 14-3-3ε's specificity (**Fig. 1.11 a, b**). However, analysis of the electrostatic surface potential at the secondary interface between PEAK3 and 14-3-3 isoforms allowed us to rationalize specificity towards the ε isoform **(Fig. 1.11 c)**. 14-3-3ε buries neutral Met 160 and Thr 161 into a basic cavity on PEAK3 (Arg 154, Lys 293, Arg 392) **(Fig. 1.11 d)**. In contrast, the other 14-3-3 isoforms contain two conserved lysines instead of Met 160 and Thr 161 (β: Lys 159, Lys 160; θ: Lys 157, Lys 158; ζ: Lys 157, Lys 158) which would clash with the basic PEAK3 cavity, likely explaining 14-3-3ε's specificity.

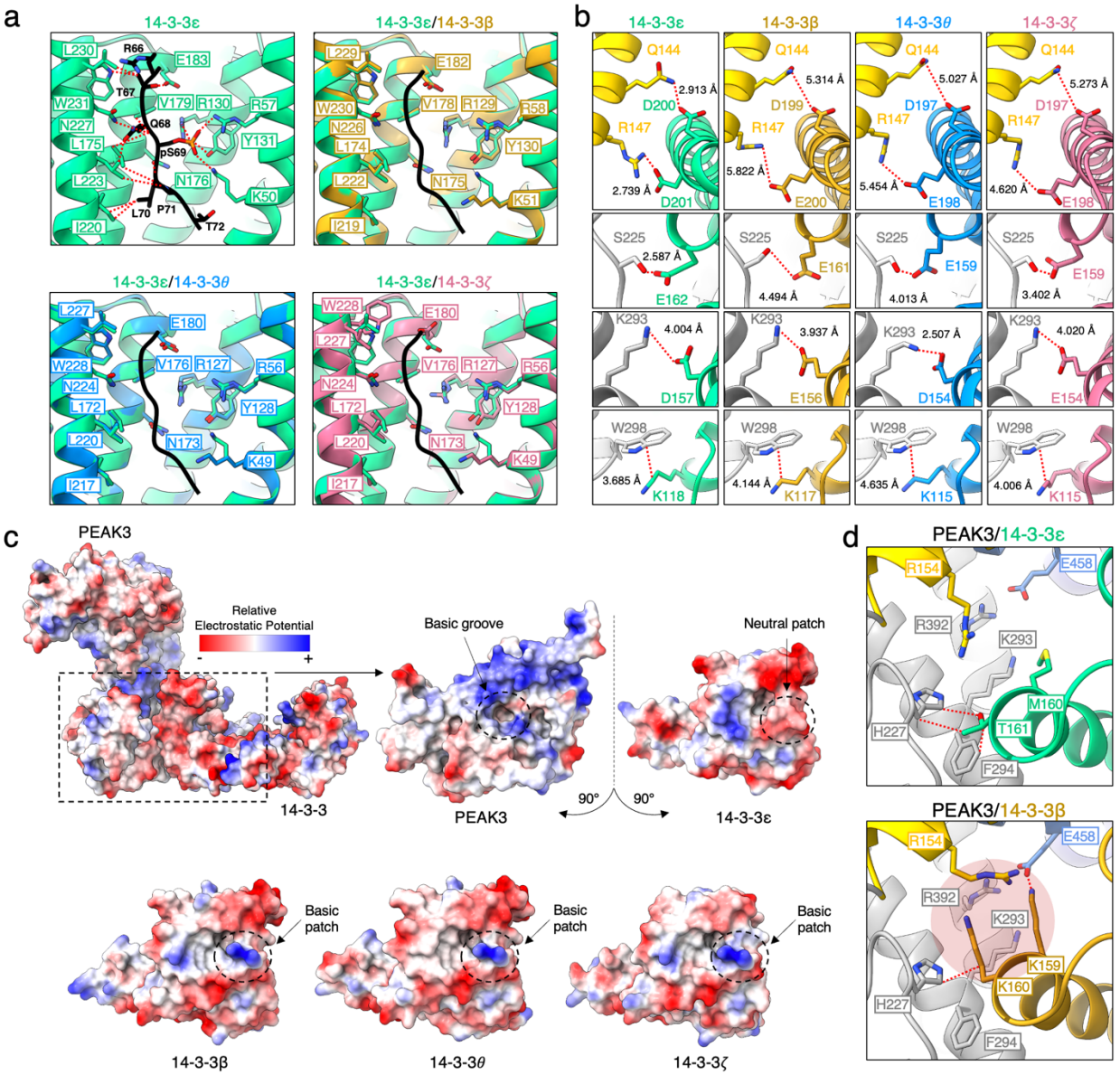


Figure 1.11: Structural analysis of PEAK3's specificity for 14-3-3ε

The PEAK3 homodimer model from the PEAK3/14-3-3 complex and crystal structures of 14-3-3 β (PDB ID: 2C23), *θ* (PDB ID: 6KZH), and ζ (PDB ID: 1A38) were fit into the PEAK3/14-3-3 complex cryo-EM map with FastRelax protocol in Rosetta[3] in torsion space, and the resulting models were compared. **a** Top left: primary interface interactions between PEAK3 and 14-3-3ε. Top right and bottom left and right: corresponding overlays between 14-3-3ε (green) and 14-3-3β (mustard yellow), 14-3-3*θ* (blue), and 14-3-3ζ (pink) demonstrating conservation of PEAK3-interacting residues among 14-3-3 isoforms. **b** Overlays of important secondary interface interactions found between PEAK3 and 14-3-3ε and preserved in 14-3-3β, *θ*, and ζ. **c** Surface representations of the PEAK3/14-3-3εβ complex and 14-3-3β, *θ*, and ζ colored by surface electrostatic potential, highlighting a distinct patch in 14-3-3ε which favors its interaction with PEAK3, relative to β, *θ*, and ζ isoforms. **d** Zoomed-in view of the patch identified in (**c**) highlighting key interactions between PEAK3 and 14-3-3ε (green) and PEAK3 and 14-3-3β (mustard yellow), with the red bubble emphasizing a charge clash between PEAK3 and 14-3-3β. Dashed lines in red indicate interactions with distances ≤ 4 Å, unless otherwise noted.

Unique features of the PEAK3 pseudokinase domain

Our structure shows that the PEAK3 pseudokinase domain adopts the canonical kinase fold, composed of a β-strand rich N-lobe and an α-helical C-lobe, although it lacks the αG helix—a feature that distinguishes it from PEAK1 and PEAK2 **(Fig. 1.12 a, b)**. There are several other key structural elements that are unique to the PEAK3 pseudokinase compared to PEAK1 and PEAK2. The activation loop, which is largely disordered in structures of PEAK1 and PEAK2, is fully resolved in PEAK3 and adopts an extended conformation. Notably, PEAK3's activation loop is approximately two-thirds the length of that of PEAK1 and PEAK2 **(Fig. 1.12 a)**. The DFG motif, only present in PEAK3, is in the "DFG-in" state in our structure, as seen in the canonical "active" conformation in kinases **(Fig. 1.12 c)**. Additionally, the αC helix is fully resolved in the PEAK3 structure, in contrast to PEAK1 and PEAK2 structures, and it adopts a conformation similar to the αC helix in active PKA[39] **(Fig. 1.12 d).** The partially resolved αC helix in PEAK1 is in a similar conformation, while the αC helix is completely unresolved in the PEAK2 structure **(Fig. 1.12 b)**. Interestingly, sequence alignment of the αC helix region of all three PEAKs shows that the C-terminal portion, which forms an ordered helix in the PEAK1 and PEAK3 structures, is absent in PEAK2 **(Fig. 1.12 a)**. Our ability to fully resolve the αC helix and the activation loop of PEAK3 is likely also due to stabilization of these regions upon 14-3-3 binding. Both the αC helix and the activation loop pack against the 14-3-3ε monomer, contributing to the already extensive interface formed between the PEAK3 and 14-3-3 dimers **(Fig. 1.12 e)**. Notably, the region of the PEAK3 activation loop which interfaces with 14-3-3 is rich in proline and glycine residues (residues 338-347: "PPGPPGSPGP") and is not present in PEAK1 or PEAK2.

Despite an active-like conformation of helix αC in PEAK3 and the presence of the "catalytic lysine," the essential salt bridge which forms between the catalytic lysine and the αC helix glutamate in active kinases is absent in PEAK3, and the αC helix glutamate in PEAK3 is substituted with Gln 221 **(Fig. 1.12 f)**. Additionally, like in the structures of the PEAK1 and PEAK2 pseudokinases, the nucleotide-binding site in PEAK3 is sterically occluded, preventing nucleotide binding. In PEAK3, the side chains of Asp 184, Tyr 187, Gln 231, and Leu 311 occupy the pocket, with Asp 184 and Gln 231 "hijacking" PEAK3's "catalytic lysine" (Lys 204), while Gln 221 of the αC helix hydrogen bonds with Gln 231 **(Fig. 1.12 f)**. Therefore, although PEAK3 mimics some organizational features associated with the active conformation of protein kinases, the fully occluded active site we observe is consistent with its classification as a pseudokinase.

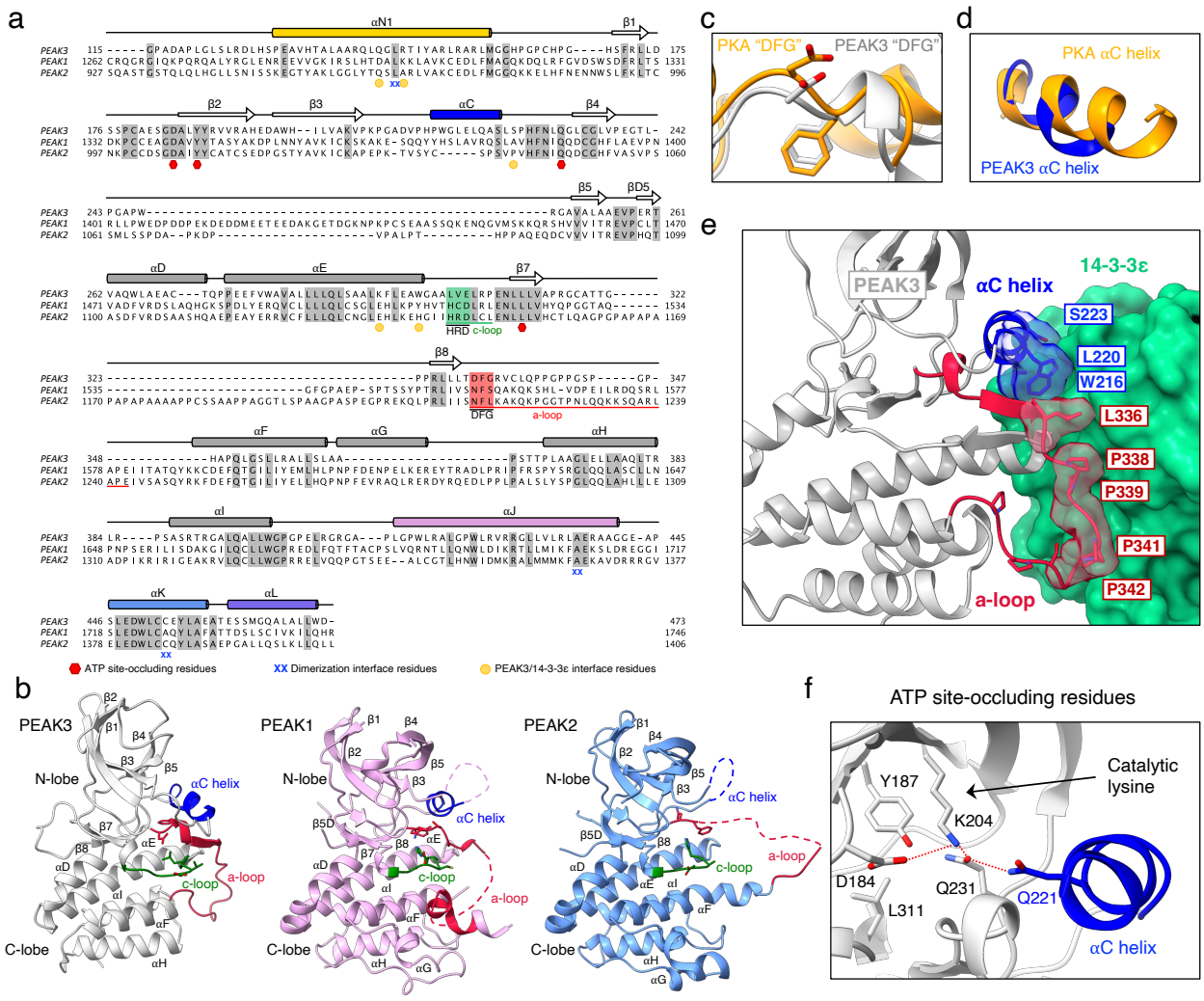


Figure 1.12: Unique features of the PEAK3 pseudokinase domain

a Protein sequence alignment of PEAK1, PEAK2, and PEAK3 depicting secondary structure elements, sequence motifs corresponding to canonical catalytic motifs in active kinases, and key dimerization interface residues based on structures of PEAK1 (PDB ID: 6BHC), PEAK2 (PDB ID: 5VE6) and PEAK3 (PEAK3/14-3-3 complex). Conserved residues are shaded in gray, αC helix is shown in blue while catalytic and activation loops with their corresponding motifs are highlighted in green and red, respectively. Residues involved in PEAK3 dimerization and those shown to occlude the pseudoactive site and PEAK3/14-3-3 secondary interface residues are marked by the indicated symbols. **b** Comparison of PEAK3 pseudokinase domain (light gray) with PEAK1 (light pink, PDB ID: 6BHC) and PEAK2 (light blue, PDB ID: 5VE6) pseudokinase domains with key structural elements highlighted (catalytic loop [c-loop] in green, activation loop [a-loop] in red, αC helix in blue). **c,d** Zoomed-in view of the (**c**) DFG motif and (**d**) αC helix in PEAK3, overlayed on the structure of PKA (PDB ID: 1ATP), aligned along entire kinase domain. **e** Zoomed-in view of the packing between the αC helix and activation loop of PEAK3 and the 14-3-3ε monomer. **f** Zoomed-in view of the pseudoactive site of PEAK3 showing the occluded nucleotide-binding site, the orientation of the catalytic lysine and the substituted Gln 221 in the αC helix.

The PEAK3/14-3-3 interaction is dependent on a canonical 14-3-3 binding motif and is further stabilized by the secondary interface

We tested the contribution of the individual binding interfaces in the PEAK3/14-3-3 structure to complex formation via co-immunoprecipitation of endogenous 14-3-3 with transiently expressed FLAG-tagged PEAK3 variants in HEK293 cells **(Fig. 1.13 a)**. Endogenous 14-3-3 robustly co-immunoprecipitated with wild type (WT) PEAK3, while mutation of the consensus site phosphorylated serine (S69A) completely abolished this interaction **(Fig. 1.13 b)**. Substituting this serine for a glutamic acid (S69E) was unable to mimic the phosphoserine, as it did not restore the PEAK3/14-3-3 interaction **(Fig. 1.14 a, b)** and resulted in relocalization of PEAK3 to the nucleus **(Fig. 1.14 c, d)**. Next, we examined whether the secondary interface between PEAK3 and 14-3-3ε, involving PEAK3's SHED and pseudokinase domains, was important for the interaction. We generated mutants of PEAK3 aimed at breaking critical interactions between the αN1 helix of the SHED domain (R147A) or the pseudokinase domain (S225A, K293A, W298A, K293A/W298A) and 14-3-3ε. Mutations in the secondary interface also diminished co-immunoprecipitation of PEAK3 with endogenous 14-3-3, with the disruption of the SHED domain interaction involving the αN1 helix (R147A) leading to an approximately 75% reduction in 14-3-3 association **(Fig. 1.13 c, d)**. Most of the mutations within the pseudokinase domain (K293A, W298A, K293A/W298A) resulted in a more modest, but statistically significant, decreases in 14-3-3 association **(Fig. 1.13 c, d)**. However, none of the mutations designed to break the secondary interface were able to completely ablate the PEAK3/14-3-3 interaction, suggesting that this interface likely serves to stabilize the complex after engagement of the phosphorylated 14-3-3 consensus sequence.

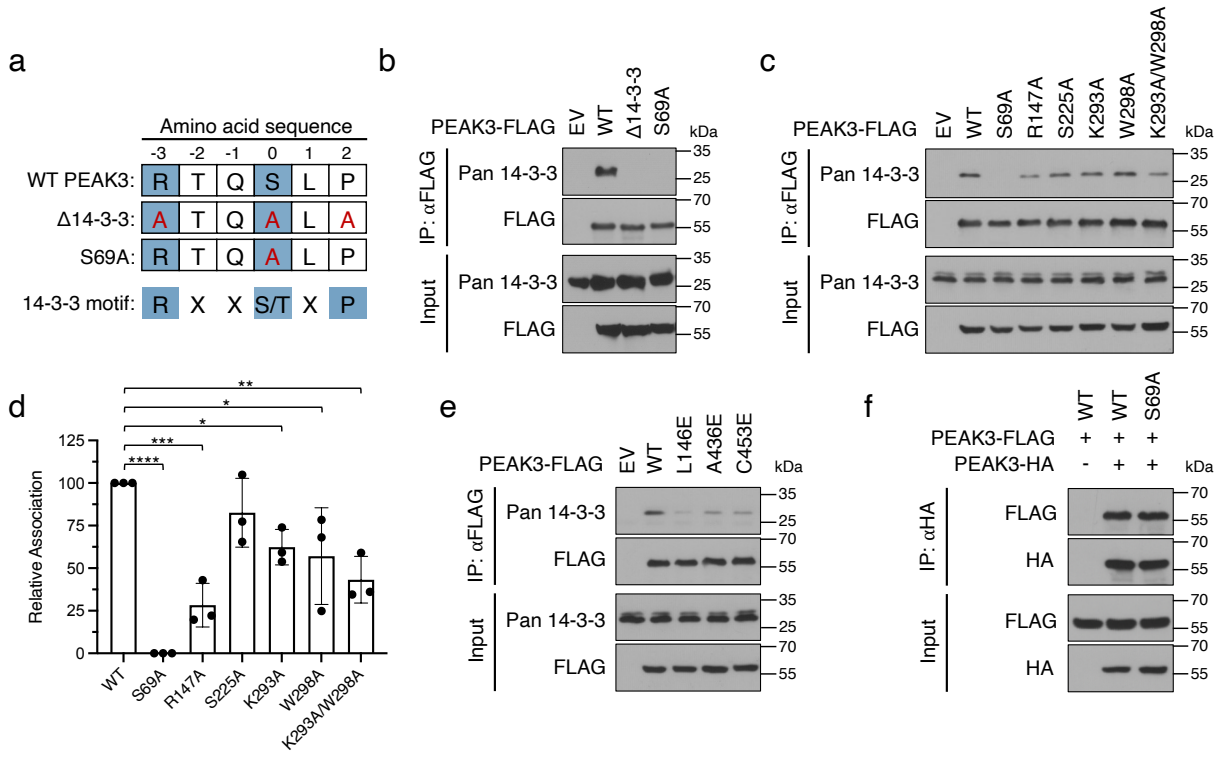


Figure 1.13: PEAK3 homodimerization and both 14-3-3 binding interfaces are critical for PEAK3/14-3-3 complex formation

a Diagram of PEAK3 mutants generated to probe PEAK3 binding to the primary site on 14-3-3. **b** Co-immunoprecipitation of endogenous 14-3-3 with FLAG-tagged WT PEAK3 and PEAK3 mutants (Δ14-3-3, S69A) transiently expressed in HEK293 cells. **c** Representative co-immunoprecipitation of endogenous 14-3-3 with PEAK3 variants carrying mutations in the secondary 14-3-3 binding interface (R147A, S225A, K293A, W298A, K293A/W298A) transiently expressed in HEK293 cells. **d** Quantification of co-immunoprecipitation data shown in panel (**c**) plotted as the mean with standard deviation from 3 independent experiments. Statistical significance was determined using One-way ANOVA Dunnett's multiple comparisons test, *p < 0.05, **< 0.01, ***p<0.001, ****p<0.0001. **e** Co-immunoprecipitation of endogenous 14-3-3 with homodimerization-deficient PEAK3 mutants (L146E, A436E, C453E) transiently expressed in HEK293 cells. **f** Co-immunoprecipitation of FLAG-tagged and HA-tagged WT PEAK3 and PEAK3 S69A transiently expressed in HEK293 cells. In panels **b-f**, protein levels were detected with the indicated antibodies by Western Blot. All co-immunoprecipitation data are representative of at least 3 independent experiments. Source data are provided as a Source Data file.

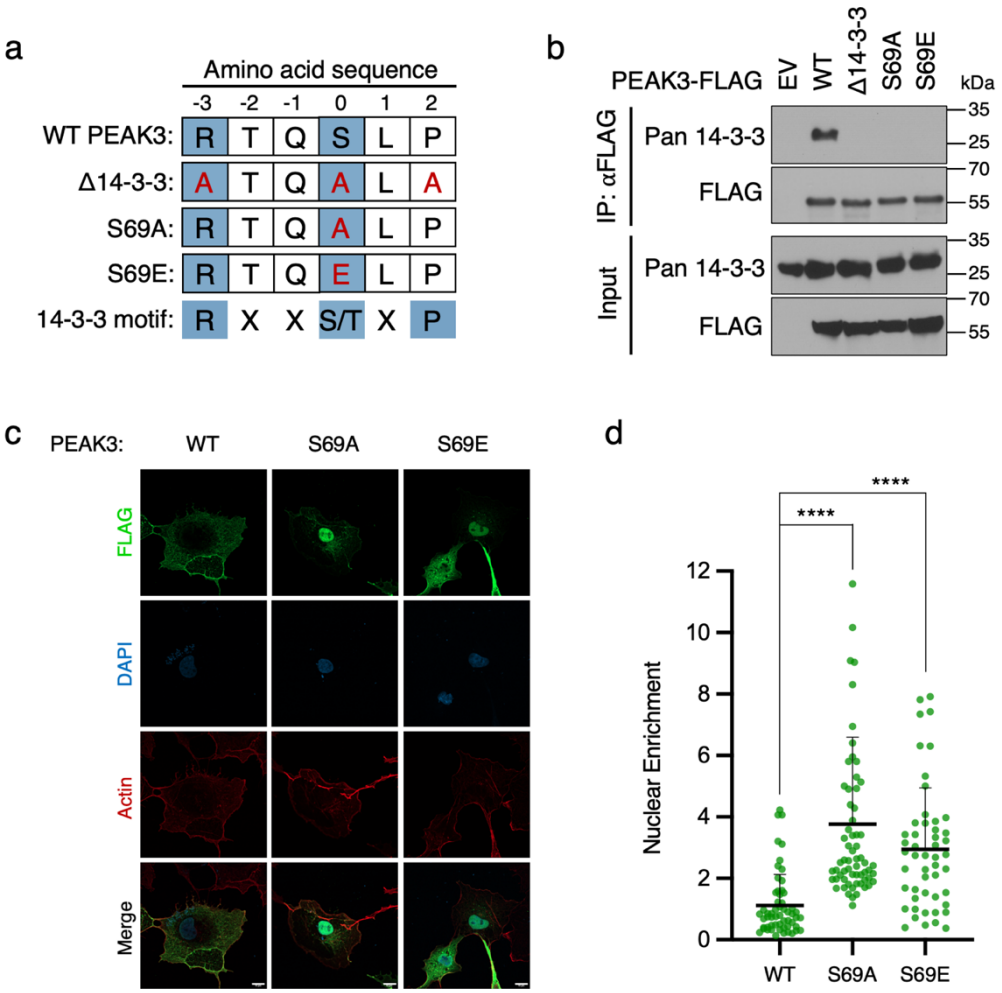


Figure 1.14: A phosphomimetic substitution at S69 does not reproduce the PEAK3/14-3-3 interaction

a Diagram of PEAK3 mutants generated to probe PEAK3 binding to the primary site on 14-3-3. **b** Co-immunoprecipitation of endogenous 14-3-3 with FLAG-tagged WT PEAK3 and PEAK3 mutants (Δ14-3-3, S69A, S69E) transiently expressed in HEK293 cells. Co-immunoprecipitation data is representative of at least 3 independent experiments. **c** Immunofluorescence-based imaging of FLAG-tagged PEAK3 transiently expressed in COS-7 cells. Representative confocal microscopy images show cells transfected with PEAK3 variants: WT, S69A or S69E. PEAK3 was detected with an anti-FLAG antibody (green), and cells were further stained with DAPI (blue, nucleus) and iFluor-647 conjugated phalloidin (red, actin). Scale bars: 10 µm. **d** Quantification of relative nuclear enrichment of PEAK3 under conditions of impaired 14-3-3 binding. The ratio of fluorescence intensity in the green channel after background subtraction measured in the nucleus to the fluorescence intensity of the non-nuclear portion of the cell is plotted for each PEAK3 variant; see Methods for details. Data are plotted as the mean with standard deviation, combining all cells from at least 3 independent experiments (n = 57, 65, and 50 total cells for WT, S69A, and S69E respectively). Statistical significance was determined using One-way ANOVA Dunnett's multiple comparisons test, ****$p<0.0001$. Source data are provided as a Source Data file.

PEAK3 homodimerization is necessary for high-affinity binding to 14-3-3

We and others have previously shown that PEAK3 homodimerization is essential for its ability to interact with its binding partners and for its signaling[22,23]. Therefore, we asked whether PEAK3 dimerization is also necessary for 14-3-3 binding. Dimerization-deficient mutants of PEAK3 (L146E, A436E, C453E)[22] were significantly impaired in binding endogenous 14-3-3, as measured by co-immunoprecipitation, emphasizing the importance of PEAK3 dimerization for a stable 14-3-3 interaction **(Fig. 1.13 e)**. We then looked if the reciprocal is true, as one of the well-characterized functions of 14-3-3 proteins is mediating protein-protein interactions between client proteins, including dimerization[40,41]. We thus tested whether 14-3-3s contribute to PEAK3 dimerization, by co-expressing HA-tagged and FLAG-tagged WT or S69A variants of PEAK3 in HEK293 cells and measuring their ability to interact by co-immunoprecipitation. The FLAG-tagged S69A PEAK3 mutant interacted with the HA-tagged S69A PEAK3 to the same extent as WT PEAK3 **(Fig. 1.13 f)**, indicating that 14-3-3 binding is not necessary for PEAK3 dimerization.

14-3-3 regulates intracellular localization of PEAK3

A well-documented functional role of 14-3-3 scaffolds is the regulation of cellular localization of their client proteins, for example, shuttling client proteins between the cytosol and the nucleus[42]. To test if 14-3-3 binding regulates PEAK3 subcellular localization, we used immunofluorescence-based imaging of FLAG-tagged WT PEAK3 and 14-3-3 binding-deficient mutant S69A. We found that WT PEAK3 uniformly distributed throughout the cytoplasm of COS-7 cells, as previously observed[22]; in contrast, the PEAK3 S69A mutant was predominantly localized in the nucleus of COS-7 cells **(Fig. 1.15 a, b)**. Mutations that disrupted the secondary

14-3-3 interface also increased PEAK3 nuclear localization, albeit to a smaller extent **(Fig. 1.15 a , b)**, consistent with their weaker effect on disrupting PEAK3/14-3-3 binding **(Fig. 1.13 d)**. These data demonstrate that 14-3-3 has a profound effect on PEAK3 cellular localization by sequestering it in the cytosol upon binding. While 14-3-3s typically alter client nuclear localization by obscuring nuclear import or export signals[31,43,44], we have not identified such signals in the PEAK3 sequence.

Loss of 14-3-3 binding and nuclear redistribution expands PEAK3's protein-protein interaction network

The redistribution of PEAK3 to the nucleus in the absence of 14-3-3 binding prompted us to examine if this change in localization modulates PEAK3's function as a molecular scaffold. We used immunoprecipitation coupled with mass spectrometry to map the binding partners of WT PEAK3 and the 14-3-3 binding-deficient S69A mutant transiently expressed in HEK293 cells. Remarkably, we observed that while WT PEAK3 predominantly interacted with 14-3-3 proteins and several motility factors, as previously described[12], the S69A mutant showed a more diverse set of binding partners, with some interactors being present in both conditions but significantly increased in the absence of 14-3-3 binding **(Fig. 1.15 c)**. Notable changes included an increase in Grb2 and CrkL binding to the S69A mutant compared to WT PEAK3. Some interactions were only observed in the absence of 14-3-3 binding, including binding of PEAK3 to a type 2A serine/threonine phosphatase complex (*PPP2R1A*, *PPP2R2A*, and *PPP3CA*), and to three protein kinase D (PKD) members, PKD1 (*PRKD1*), PKD2 (*PRKD2*), and PKD3 (*PRKD3*). This substantial expansion of the PEAK3 interactome in the absence of 14-3-3 binding strongly suggests that one of the primary functions of 14-3-3 binding to PEAK3 is to regulate its

scaffolding potential, either by directly blocking interactions between PEAK3 and its binding partners or by restricting PEAK3 shuttling between the cytosol and the nucleus.

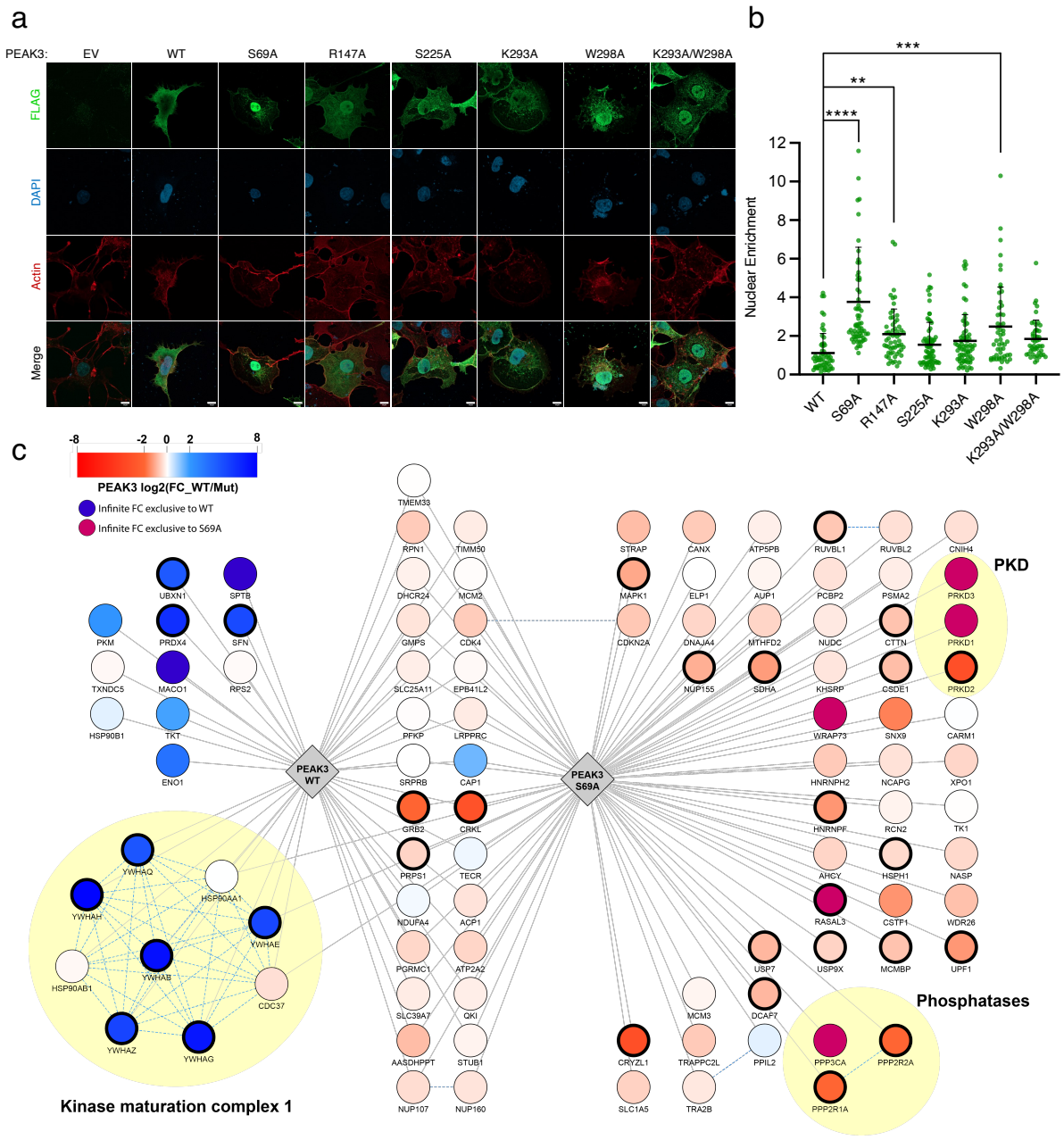


Figure 1.15: 14-3-3 influences cellular localization and scaffolding range of PEAK3
a Immunofluorescence-based imaging of FLAG-tagged PEAK3 transiently expressed in COS-7 cells. Representative confocal microscopy images show cells transfected with an empty vector (EV) control or PEAK3 variants: WT, S69A, R147A, S225A, K293A, W298A, or K293A/W298A. (Figure caption continued on the next page.)

Figure 1.15: 14-3-3 influences cellular localization and scaffolding range of PEAK3
(Figure caption continued from the previous page.) PEAK3 was detected with an anti-FLAG antibody (green), and cells were further stained with DAPI (blue, nucleus) and iFluor-647 conjugated phalloidin (red, actin). Scale bars: 10 μm. **b** Quantification of relative nuclear enrichment of PEAK3 under conditions of impaired 14-3-3 binding. The ratio of fluorescence intensity in the green channel after background subtraction measured in the nucleus to the fluorescence intensity of the non-nuclear portion of the cell is plotted for each PEAK3 variant; see Methods for details. Data are plotted as the mean with standard deviation, combining all cells from at least 3 independent experiments (n = 57, 65, 60, 69, 71, 53, and 48 total cells for WT, S69A, R147A, S225A, K293A, W298A, and K293A/W293A, respectively). Statistical significance was determined using One-way ANOVA Dunnett's multiple comparisons test, **p< 0.01, ***p<0.001, ****p<0.0001. **c** Spectrum of protein-protein interactions engaged by the WT or S69A PEAK3 analyzed by immunoprecipitation/mass spectrometry approach. Edges represent significant specific interactions of PEAK3 WT or S69A as determined by SAINTexpress (BFDR < 0.05) compared to negative control (non-transfected cells). Node colors represent the log2 fold change enrichment determined by MSstats between WT and S69A PEAK3 (bold node border represents significant adjusted p value < 0.05). CORUM complexes are indicated by yellow circles. Source data are provided as a Source Data file.

The enhanced interaction of PKD kinases with the 14-3-3 binding-deficient mutant of PEAK3 suggests that these kinases could mediate PEAK3 Ser 69 phosphorylation. Indeed, the sequence of PEAK3's 14-3-3 binding site, which encompasses Ser 69, is consistent with a PKD substrate consensus site **(Fig. 1.16 a)**. Treatment of HEK293 cells with increasing concentrations of the pan PKD-specific tool compound, active-site inhibitor CRT0066101[45] resulted in a dose-dependent decrease of endogenous 14-3-3 co-immunoprecipitation with FLAG-tagged WT PEAK3 **(Fig. 1.16 b)**. Treatment with a PKD allosteric inhibitor, CID755673, also led to a dose-dependent decrease in endogenous 14-3-3 co-immunoprecipitation with FLAG-tagged WT PEAK3, although to a lesser extent than CRT0066101 **(Fig. 1.17 a, b)**. These experiments demonstrated that in cells, PKD activity modulates PEAK3's interaction with 14-3-3. Next, we tested if PKD can directly phosphorylate PEAK3. In an in vitro phosphorylation assay, recombinant PKD2 phosphorylated the peptide corresponding to the putative PKD recognition sequence of WT PEAK3 (PKKILTRTQSLPTR) to the same degree as a positive control peptide

for PKD, CREBtide (KRREILSRRPSYR) **(Fig. 1.16 c)**[46-48]. In contrast, a PEAK3 peptide containing the S69A mutation (PKKILTRTQALPTR) was not phosphorylated at a detectable rate. Lastly, COS-7 cells transfected with FLAG-tagged WT PEAK3 treated with either CRT0066101 or CID755673 resulted in an increase of PEAK3 nuclear localization, similar to the effect of the S69A mutation **(Fig. 1.16 d, e; Fig. 1.17 c, d)**, consistent with PKDs having a regulatory role in the PEAK3/14-3-3 interaction. However, PKD inhibition did not completely abolish the PEAK3/14-3-3 interaction, suggesting that other kinases may also regulate the PEAK3/14-3-3 complex.

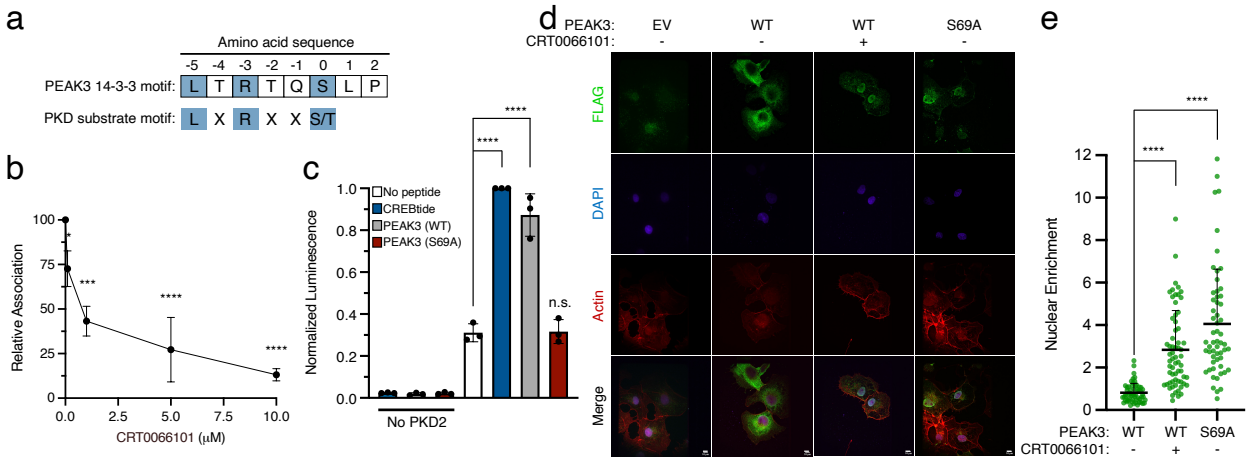


Figure 1.16: PKD regulates the PEAK3/14-3-3 interaction

a Consensus sequence of PKD substrates aligned with PEAK3's 14-3-3 consensus site. **b** Co-immunoprecipitation of endogenous 14-3-3 with FLAG-tagged WT PEAK3 transiently expressed in HEK293 cells treated with 0.1% DMSO or increasing concentrations of the PKD inhibitor CRT0066101 dihydrochloride. Quantification of co-immunoprecipitation data plotted as the mean with standard deviation from 3 independent experiments. Statistical significance was determined using One-way ANOVA Dunnett's multiple comparisons test, ***p<0.001, ****p<0.0001. Protein levels were detected with anti-FLAG and anti-pan 14-3-3 antibodies by Western Blot. **c** ADP-Glo PKD2 in vitro kinase assay conducted with PEAK3-derived PKD consensus site peptides (WT and S69A) and a PKD2 substrate peptide (CREBtide). Data are plotted as the mean with standard deviation, combining 3 independent experiments. Statistical significance was determined using One-way ANOVA Dunnett's multiple comparisons test, ****p<0.0001. **d** Immunofluorescence-based imaging of FLAG-tagged PEAK3 transiently expressed in COS-7 cells. Representative confocal microscopy images show cells transfected with an empty vector (EV) control or indicated FLAG-tagged PEAK3 constructs, and treated with 0.1% DMSO or 10 μM PKD inhibitor CRT0066101. PEAK3 was detected with an anti-FLAG antibody (green), and cells were further stained with DAPI (blue, nucleus) and iFluor-647 conjugated phalloidin (red, actin). Scale bars: 10 μm. **e** Quantification of relative nuclear enrichment of PEAK3 under conditions of impaired 14-3-3 binding. The ratio of fluorescence intensity in the green channel after background subtraction measured in the nucleus to the fluorescence intensity of the non-nuclear portion of the cell is plotted for each PEAK3 variant; see Methods for details. Data are plotted as the mean with standard deviation, combining all cells from at least 3 independent experiments (n = 58, 64, and 57 total cells for WT, WT + CRT0066101, and S69A respectively). Statistical significance was determined using One-way ANOVA Dunnett's multiple comparisons test, ****p<0.0001. Source data are provided as a Source Data file.

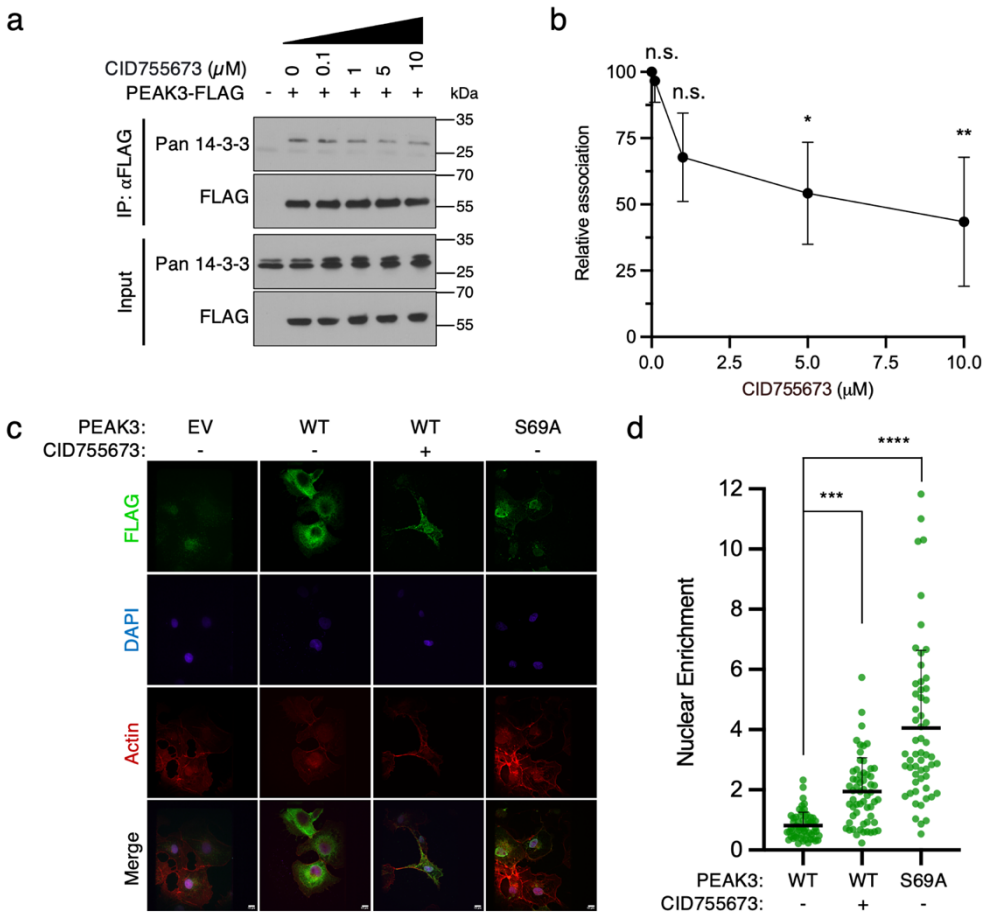


Figure 1.17: Allosteric inhibition of PKD regulates the PEAK3/14-3-3 interaction
a Representative co-immunoprecipitation of endogenous 14-3-3 with FLAG-tagged WT PEAK3 transiently expressed in HEK293 cells treated with 0.1% DMSO or increasing concentrations of the allosteric PKD inhibitor CID755673. **b** Quantification of co-immunoprecipitation data shown in panel (**a**) plotted as the mean with standard deviation from 3 independent experiments. Statistical significance was determined using One-way ANOVA Dunnett's multiple comparisons test, *p < 0.05, **p < 0.01. Protein levels were detected with the indicated antibodies. **c** Immunofluorescence-based imaging of FLAG-tagged PEAK3 transiently expressed in COS-7 cells. Representative confocal microscopy images show cells transfected with an empty vector (EV) control or indicated FLAG-tagged PEAK3 constructs treated with 0.1% DMSO or 10 μM PKD inhibitor CID755673. PEAK3 was detected with an anti-FLAG antibody (green), and cells were further stained with DAPI (blue, nucleus) and iFluor-647 conjugated phalloidin (red, actin). Scale bars: 10 μm. **d** Quantification of relative nuclear enrichment of PEAK3 under conditions of impaired 14-3-3 binding. The ratio of fluorescence intensity in the green channel after background subtraction measured in the nucleus to the fluorescence intensity of the non-nuclear portion of the cell is plotted for each PEAK3 variant; see Methods for details. Data are plotted as the mean with standard deviation, combining all cells from at least 3 independent experiments (n = 58, 59, and 57 total cells for WT, WT + CID755673, and S69A respectively). Statistical significance was determined using One-way ANOVA Dunnett's multiple comparisons test, ***p<0.001, ****p<0.0001. Source data are provided as a Source Data file.

DISCUSSION

Here, we present the first structure of the PEAK3 pseudokinase and the first structural characterization of any full-length PEAK family member. The N-terminal domain of PEAK3 in our structure is largely disordered, but its presence was critical for capturing PEAK3 in complex with the endogenous 14-3-3 dimer. 14-3-3 proteins have been consistently identified in unbiased mass spectrometry studies as top PEAK3 interaction partners[22-24]. In our experiments, this interaction was key to purifying full-length PEAK3 and may have played a stabilizing role, yielding a higher resolution cryo-EM reconstruction **(Fig. 1.6)**. While several putative 14-3-3 binding motifs can also be found in the N-terminal domains of PEAK1 and PEAK2 **(Fig. 1.3 b, c)**, it is unclear whether 14-3-3 proteins play a similar role for these family members, since the use of N-terminal truncated constructs in previous structural studies of PEAK1 and PEAK2 eliminated the chances of their isolation in complex with 14-3-3s[21,26,27]. Interestingly, the asymmetric binding mode we observe between PEAK3 and 14-3-3 should allow PEAK3 heterodimers containing PEAK1 or PEAK2 to complex with 14-3-3.

In the PEAK3/14-3-3 structure, two distinct interfaces contribute to complex formation. The first, canonical interface, involves binding between the phosphorylated 14-3-3 binding motifs located in the N-terminal domains of each PEAK3 monomer and the conserved 14-3-3 amphipathic grooves. The second interface is unique and contrasts with commonly observed secondary interactions, where the 14-3-3 client sits within or on top of the 14-3-3 cradle and typically interacts with both 14-3-3 molecules in the dimer. Instead, the secondary interface in the PEAK3/14-3-3 complex involves only one monomer of 14-3-3, which forms an extensive interface with the PEAK3 dimer. Our structural analysis demonstrates that the secondary interface, via charge complementarity, is key in driving specificity of PEAK3 to 14-3-3ε.

Interestingly, solution studies designed to characterize dynamic protein-protein interactions, such as small angle X-Ray scattering (SAXS), have previously pointed to similarly asymmetric binding poses between 14-3-3 and the CaMKK2 and DAPK2 kinases[49,50]. While in our experiments 14-3-3 binding clearly reduces the overall diversity of PEAK3's interactome, the unique architecture of the PEAK3/14-3-3 complex captured in our structure leaves the unstructured PEAK3 N-termini accessible. As these contain numerous consensus binding sites for key signaling proteins, having these regions exposed may play an important role in tuning of PEAK3 scaffolding function and/or initial recruitment of PEAK3 complexes. Lastly, asymmetry in the 14-3-3 interaction leaves open a possibility that a second 14-3-3 heterodimer could be accommodated at the free secondary interface of the other PEAK3 monomer. We predict that to recruit a second 14-3-3 dimer, one of the primary 14-3-3 binding sites of PEAK3 (containing the Ser 69) would need to be free, since this site contributes significant binding affinity. Although such a ternary complex may exist under some conditions in cells, we do not observe it in vitro.

Our structure highlights the conservation of SHED-dependent dimerization across all PEAK pseudokinases, as previously anticipated based on structural models[22]. We propose here an explanation for why dimerization of PEAKs is essential for binding of their signaling partners, a phenomenon consistently observed across studies[21,26,27]. Based on our finding that the PEAK3 SHED domain forms essential contacts with 14-3-3, largely contributing to the secondary interface of the PEAK3/14-3-3 interaction, we speculate that this binding mode might represent a universal model for how PEAK pseudokinases interact with other signaling molecules which depend on PEAK dimerization for binding. This hypothesis is supported by our observation that when 14-3-3 binding to PEAK3 is disrupted, exposing the SHED domain interface, the spectrum of PEAK3 interactions with other binding partners increases significantly.

The PEAK3 structure highlights unique features of its pseudokinase domain that are distinct from PEAK1 and PEAK2. The overall architecture of the PEAK3 pseudokinase homodimer within the PEAK3/14-3-3 complex, or alone solved at lower resolution, shows significant twisting between two pseudokinase domains instigated by rotations of the SHED domain helices, αJ and αL, relative to PEAK1 and PEAK2. These differences are thus independent from 14-3-3 binding and intrinsic to PEAK3. Within the putative ATP-binding site, PEAK3 resembles its paralogs, as it also has a pocket highly occluded by the side chains of multiple residues which engage the catalytic lysine. However, unlike in structures of PEAK1 and PEAK2, in which the αC helix and activation loop were either partially or not at all resolved, these structural elements are found intact in the PEAK3 structure due to their stabilization by the interaction with 14-3-3ε. The proline-rich sequence of the PEAK3 activation loop, which is positioned closest to 14-3-3ε, is distinct in PEAK3 compared to PEAK1 and PEAK2. This sequence is reminiscent of proline-rich SH3 domain-binding sites, suggesting a potential role for the PEAK3 activation loop in the recruitment or stabilization of SH3 domain-containing interaction partners. A number of characterized PEAK3 binding partners, such as CrkII and Grb2, contain two SH3 domains. The canonical proline-rich motifs found within PEAK3's N-terminal domain may engage one of the SH3 domains to initiate the interaction with these partners, while the less conserved motif within the activation loop may act to further stabilize the complex, similar to what is seen in the PEAK3/14-3-3 complex.

The strong association between PEAK3 and 14-3-3 points to a functional role for this interaction. 14-3-3s regulate their client proteins through several mechanisms, including inducing conformational changes, protecting sites of posttranslational modifications, altering subcellular localization, and facilitating or blocking protein-protein interactions[29-32]. We show that 14-3-3 is

not essential for PEAK3 dimerization, but rather controls subcellular localization of PEAK3 and prevents it from nuclear translocation. Since PEAK3 does not have its own nuclear import signal, it could be that 14-3-3 blocks PEAK3 from interacting with another protein that is responsible for delivery of PEAK3 to the nucleus. Our mass spectrometry analysis shows that when not bound to 14-3-3, PEAK3's interactome is greatly expanded. Consistent with this idea, Roy *et al.*[51] have recently shown that 14-3-3 directly competes with CrkII for binding to PEAK3. Thus, 14-3-3 might exert a dual control over PEAK3 function: over its localization and the extent of its protein-protein interactions.

Among notable PEAK3 interactors enriched in the absence of 14-3-3 binding are a PP2A serine/threonine phosphatase complex and the PKD family of serine/threonine kinases. PKDs play numerous important roles in the cell, including regulating secretion and vesicle transport through the trans-Golgi network, inducing migration and differentiation, attenuating JNK activation in response to EGFR stimulation, and stimulating the Ras and ERK pathways[52-57]. One way PKDs exert their pleiotropic effects is by phosphorylating 14-3-3 consensus motifs of their substrates, thereby promoting 14-3-3 binding and cytoplasmic sequestration of their substrates[58]. For example, RIN1, which in its unphosphorylated form inhibits the Ras/Raf interaction by associating with membrane-bound activated Ras, loses this ability upon PKD-dependent phosphorylation of its 14-3-3 consensus site that promotes 14-3-3 binding and blocks RIN1 association with the membrane[59]. Another example is class IIa histone deacetylases, which can shuttle between the nucleus and cytoplasm and form complexes with transcriptional repressors in the nucleus; however, PKD phosphorylation enables 14-3-3 binding, restricting nuclear import of class IIa histone deacetylases[60,61]. We show that the PEAK3/14-3-3 interaction is PKD-dependent and that PKD phosphorylates PEAK3's 14-3-3 consensus site in vitro, suggesting that

PKD regulates the extent of PEAK3's role as a scaffold via 14-3-3 binding. PP2A phosphatases, which we also found recruited to PEAK3, might oppose the PKD-mediated effects, constituting the opposing arm of this regulation.

How and if 14-3-3 regulates interactions of PEAK3 with other signaling proteins, such as MAPK and Grb2, is a topic of future investigation. PEAK3 overexpression has been shown to increase MAPK phosphorylation in AML cells, and PEAK3 knockdown consequently decreases phospho-MAPK[24]; thus, 14-3-3 may play an important role in this regulation. Grb2 is known to interact with PEAK3 via the N-terminal domain Tyr 24 and has been shown to regulate cell invasiveness in breast epithelial cells[23]. The enriched interaction between Grb2 and PEAK3 in the absence of 14-3-3 binding reported here suggests that 14-3-3 might negatively regulate the oncogenic Grb2/PEAK3 signaling axis.

Our structure provides the first characterization of how the SHED domain supports the scaffolding functions of PEAK pseudokinases. It also underscores the remarkable conservation of pseudokinase architecture and dimeric organization across all PEAK pseudokinases, suggesting that all of them might utilize a similar interface for engaging their signaling partners. At the same time, the unique features of the PEAK3 pseudokinase domain offer a possibility for conceptualizing paralog-specific therapeutics[22,23,28]. An expanding body of evidence demonstrating association of PEAKs with the progression of human cancers makes them emerging targets of interest[3]. Binding of PEAK3 to 14-3-3 may play an important role in buffering the population of PEAK3 that is available to engage with its scaffolding substrates and thereby modulate the oncogenic potential of PEAK pseudokinases.

MATERIALS AND METHODS

Plasmids and cell culture

The human PEAK3 gene was synthesized by GenScript and subcloned into the pcDNA4/TO vector with a C-terminal 3xFLAG tag, 1xFLAG tag, or HA tag. Mutations were introduced using Quikchange mutagenesis (Agilent). All constructs were verified via DNA sequencing (Elim Biopharmaceuticals). HEK293 (ATCC, CRL-1573) and COS-7 (ATCC, CRL-1651) cells were maintained at 37 ºC and 5% CO_2 and cultured in Dulbecco's modified Eagle media (Life Technologies) supplemented with 10% FBS (Hyclone) and 1% penicillin/streptomycin (Life Technologies). PEAK3 constructs were transiently transfected into cells 24 hours prior to imaging or cell lysis using Lipofectamine 3000 (Invitrogen) according to the manufacturer's protocol. The PKD inhibitors CRT0066101 (MedChemExpress, HY-15698A) and CID755673 (Selleck Chemicals, S7188) were dissolved in DMSO and added to cells 1 hour prior to cell lysis.

PEAK3 expression and purification

Expi293F suspension cells (Thermo Fisher Scientific, A14527) were maintained at 37 ºC and 8% CO_2 while rocking at 125 RPM (Thermo Fisher Scientific, 88881101 shaker) in 125 mL non-baffled sterile cap vented flasks. The PEAK3-1xFLAG construct was transfected into 30 mL of Expi293F culture at a cell density of 4.0 x 10^6 cells/mL using ExpiFectamine 293 transfection reagent (Thermo Fisher Scientific, A14524) according to the manufacturer's protocol at 1 µg DNA /1 mL. Enhancer was added 18 hours post-transfection, and cells were collected 48 hours post-enhancer addition in an Allegra X-14 centrifuge (Beckman Coulter) at 1,000 xg for 10 min. Pellets were flash frozen in liquid nitrogen for later purification or resuspended in binding buffer

(50 mM Tris-HCl, pH 7.5, 150 mM NaCl, 2 mM $MgCl_2$, 2 mM DTT) with 1 mM NaF, 1 mM $NaVO_4$, DNase I, and a cOmplete mini EDTA-free protease inhibitor cocktail tablet (Roche) supplemented fresh. If frozen, pellets were thawed on ice and homogenized by gentle pipetting. Cells were lysed using an EmulsiFlex-C5 homogenizer (Avestin) at 10,000–15,000 psi, and the cell lysate was spun down in an Avanti centrifuge with a JA 25.50 rotor at 20,000 xg for 40 min, at 4 °C. The clarified lysate was then incubated with 125 µL of G1 Flag resin (Genscript) per 30 mL culture overnight at 4 °C with rotating before washing with 50 bead volumes of lysis buffer. Resin was then incubated with 10 bead volumes of elution buffer (lysis buffer + 0.25 mg/mL FLAG peptide [SinoBiological]) for 1 hour at 4 °C with rotating and protein was eluted by gravity flow. The eluate was concentrated using an Amicon Ultra-0.5 30k MWCO centrifugal filter (Millipore), before being loaded and separated on a Superdex 200 Increase 10/300 GL column (GE Life Sciences). PEAK3/14-3-3 peak fractions were collected, concentrated to 20 µM and flash frozen.

Sample preparation for cryo-electron microscopy imaging

Peak fractions of the PEAK3/14-3-3 complex were pooled and concentrated using an Amicon Ultra-0.5 30k MWCO centrifugal filter (Millipore). Immediately before preparing cryo-EM grids, a final concentration of 0.1% n-Octyl-β-D-glucoside (Affymetrix) was added to a 7 µM sample of the PEAK3/14-3-3 complex to limit orientation bias of PEAK3/14-3-3 complex particles. 3 µL of this sample was then applied to negatively glow discharged Quantifoil R1.2/1.3 300 mesh Au holey-carbon grids, blotted using a Vitrobot Mark IV (FEI), and plunge frozen in liquid ethane at 5 °C, 100% humidity, 4–8 s blot time, and 4 blot force.

Grids were imaged on a 300-keV Titan Krios (FEI) with a K3 direct electron detector (Gatan) and a BioQuantum energy filter (Gatan) using SerialEM v4.0.3 and Digital Micrograph v3.31.2359.0. Data for the PEAK3/14-3-3 complex were collected in super-resolution mode at a physical pixel size of 0.835 Å pixel^{-1} with a dose rate of 16.0 e^- pixel^{-1} s^{-1} (operated in non-CDS mode). Images were recorded with a 3 s exposure over 120 frames with a dose rate of 0.57 e^- Å^{-2} per frame.

Image processing and 3D reconstruction

Raw movies were corrected for motion and radiation damage with MotionCor2 v1.5.0[62] during collection launched via Scipion 3.0.1 [63], and the resulting sums were imported in CryoSPARC v2.15.0[4]. Micrographs were curated based on ice thickness, CTF fit resolution, and particle distribution, yielding a final stack of 80% of total micrographs collected. Micrograph contrast transfer function (CTF) parameters were estimated with the patch CTF job in CryoSPARC. Particles were initially picked with blob picking, extracted, and 2D-classified yielding both PEAK3 only particles and PEAK3/14-3-3 complex particles. Particles were then template picked with low-pass filtered (to 20 Å) 2D class averages of the PEAK3/14-3-3 complex, and the resulting picks were extracted with 2× Fourier cropping and subjected to iterative rounds of ab initio and heterogeneous refinements (see processing workflow chart). Finally, unbinned particles were re-extracted and run through non-uniform refinements to achieve reconstruction with the highest resolution. The final reconstruction of the PEAK3/14-3-3 complex used for model building included 169,563 particles with C1 symmetry and resulted in an overall resolution of 3.1 Å by gold standard FSC (GS-FSC) cut-off of 0.143 (masked), sharpened with -107.4 B-factor.

Particles in the same dataset were also template picked with low-pass filtered (to 20 Å) 2D class averages of the PEAK3 homodimer alone and processed similarly to PEAK3/14-3-3 complex particles. To alleviate streaking artifacts due to the orientation bias of PEAK3 homodimer particles in the reconstructions from CryoSPARC, unbinned particles of the PEAK3 homodimer were re-extracted and imported into RELION 3.1[5] through pyEM v0.5 where they were further 3D-classified. The final reconstruction of the PEAK3/14-3-3 complex used for model building included 32,734 particles and resulted in an overall resolution of 4.9 Å by GS-FSC (masked).

Each map was assessed for local and directional resolutions through ResMap v1.1.4[1] and 3DFSC v3.0[6] server, respectively. For the PEAK3/14-3-3 complex reconstruction, the pseudokinase domain of the monomer of PEAK3 not interfacing with the 14-3-3 dimer was at local resolutions between 3.5–5.5 Å, while the remainder of the complex was at local resolutions between 2.5–3.5 Å.

Model building, refinement, and validation

Model building for both the PEAK3/14-3-3 complex and the PEAK3 homodimer began with fitting of the AlphaFold2 models of PEAK3, with the N-terminal extensions truncated due to low confidence scores, and 14-3-3 isoforms ε and β into the corresponding 3D volumes in ChimeraX 1.2.5[64]. The PEAK3/14-3-3 complex and PEAK3 homodimer models were fit into the respective cryo-EM maps with FastRelax protocol in Rosetta 3.0 in torsion space[3]. For the PEAK3/14-3-3 complex, the PEAK3 N-terminal peptides within the 14-3-3 cradle were built manually in Coot 0.9.6 and the full complex model was further manually examined and refined in Coot and ISOLDE 1.2.1[65,66]. Per-atom *B*-factors were assigned in Rosetta indicating the local

quality of the map around that atom[3]. MolProbity, as part of the Phenix 1.19.2 validation tools, was used to assess quality of the models[67,68]. The residues modeled for the PEAK3/14-3-3 complex are as follows: PEAK3-Chain A (128-406, 419-473), PEAK3-Chain B (130-406, 415-472), 14-3-3β (3-232), 14-3-3ε (3-233), PEAK3 N-terminus-Chain E (66-73), and PEAK3 N-terminus-Chain P (66-72). Residues modeled for the PEAK3 homodimer are PEAK3-Chain A (128-406, 419-473) and PEAK3-Chain B (130-406, 415-472). Q-scores were calculated using the appropriate plugin in UCSF Chimera 1.16[69,70].

Identification and structural alignment of 14-3-3/client complexes

A search was carried out for 14-3-3/client complex structures in the Protein Data Bank using the Advanced Search Query Builder via the sequence similarity feature. Structures with a sequence similarity of 30% to 14-3-3ε and an E-value cutoff of 0.1 were manually curated, removing 14-3-3 structures that only contained client peptides, with no globular domains present. Following curation, structures were aligned in ChimeraX[64] on the 14-3-3 dimer to visualize different binding modes. Structures exhibiting binding mode 1 include PDB IDs: 2O98, 5N6N, 6UAN, 6Q0K, 7MFE, 7MFF, 1IB1, 6XAG, 6U2H. Structures exhibiting binding mode 2 include PDB IDs: 3AXY, 6GN0, 6GNK, 6GNJ, 6GN8, 5LTW, 6GNN.

Co-immunoprecipitation and Western blot analysis

HEK293 cells were seeded on 100 mm dishes at a density of 5.0 x 10^6 cells/dish and transfected the following day. 24 hours post transfection, cells were washed two times on ice with ice cold PBS followed by lysis (50 mM Tris-HCL pH 8.0, 150 mM NaCl, 0.5% Triton X-100, 0.5% NP-40, 1 mM NaF, 1 mM Na_3VO_4, 1 mM EDTA, cOmplete mini EDTA-free protease

inhibitor cocktail [Roche]). Cells were scraped and incubated with rotation at 4 °C for 45 min to ensure complete lysis. Lysates were clarified by centrifugation for 10 min at 21,000 xg at 4 °C. The clarified lysates were pre-cleared with 100 µL Protein A beads (Novex) for 30 min at 4 °C with rotation. The pre-cleared lysates were then incubated with 100 µL of antibody/protein A complexed beads (3 µg of anti-FLAG [mouse, Sigma, F1804] or 3 µg of anti-HA [mouse, SCBT, sc-7392]) per 100 mm plate overnight at 4 °C with rotation. The beads were washed three times with lysis buffer. The bound proteins were eluted from the beads using SDS-loading buffer and were boiled at 95 °C for 10 min prior to SDS-PAGE and analysis by Western blot. Samples were run on 4-15% acrylamide gels and transferred onto PVDF membranes. Membranes were blocked in 5% milk in TBS and 0.1% Tween-20 (TBS-T) for 30 min at room temperature, followed by incubation with primary antibodies diluted in blocking buffer (1:2,000, anti-FLAG [rabbit, CST, 2368S], 1:1,000, anti-HA [mouse, SCBT, sc-7392], and 1:1,000, anti-pan 14-3-3 [rabbit, CST, 8312S]) at 4 °C overnight. Next, blots were incubated with secondary antibodies diluted in blocking buffer (1:500, anti-IgG Veriblot, Abcam, ab131366) for 1 hour at room temperature. ECL Western blotting detection reagent (GE) or ECL prime (VWR) were used for detection. HA, FLAG and IgG secondary antibodies were validated through empty vector transfection and the manufacturer. The pan-14-3-3 antibody was validated through the manufacturer.

Western blot quantification was performed in FIJI v2.0.0 using the gel analysis tool. First, the 14-3-3 IP signal was normalized against the corresponding IP FLAG signal. Next, each normalized 14-3-3 IP signal was compared against the 14-3-3 signal from the PEAK3 WT pull-down (secondary interface IP) or DMSO control (PKD inhibition IP). Statistical significance was determined using One-way ANOVA Dunnett's multiple comparisons test in Prism 9 (Graphpad Software, Inc.).

Immunofluorescence

COS-7 cells (1.0 x 10^5 per well) were plated onto glass coverslips or in glass bottom petri dishes (MatTek, P35GCOL-1.5-14-C) and transfected the following day. 24 hours post transfection, cells were rinsed twice with PBS, followed by fixation in 3.7% formaldehyde for 10 min at room temperature. For PKD inhibition experiments, 10 μM CRT0066101 (MedChemExpress, HY-15698A), 10 μM CID755673 (Selleck Chemicals, S7188), or the equivalent volume of DMSO (corresponding to 0.1%) was added 1 hour prior to fixation. Cells were then rinsed three times with PBS, followed by blocking and permeabilization with the blocking/permeabilization buffer (PBS, 2.5% BSA, 0.1% Triton X-100) for 20 min at room temperature. Next, the cells were incubated with primary antibodies (1:500, anti-FLAG [rabbit, CST, 2368S]) diluted in the blocking/permeabilization buffer for 1 hour at room temperature. The cells were then rinsed three times with PBS, followed by incubation with secondary antibodies (1:1,000, AlexaFluor 488 anti-rabbit IgG [donkey, Life Technologies, A21206]) diluted in blocking buffer for 1 hour at room temperature. During the last 20 min of this incubation, iFluor-647-Phalloidin (Cayman Chemical Company, 20555) was added at a 1:1000 dilution to stain actin. Coverslips were mounted onto glass coverslips with Prolong Gold AntiFade with DAPI (Cell Signaling Technologies) to stain the nucleus. Images were acquired on either a Zeiss LSM 800 confocal laser scanning microscope using a 63x oil objective running Zen 2 blue edition v1.0 (Zeiss) or an Eclipse Ti with a CSU-X1 spinning disc confocal (Nikon) and Clara interline CCD camera (Andor) with a Plan Apo 60x oil objective (Nikon) running Nikon Elements 5.02 build 1266 (Nikon) . The FLAG antibody was validated through empty vector transfection and the manufacturer. The secondary antibody was validated through the manufacturer.

Image analysis was performed in FIJI v1.53f51. The nucleus and total cell were manually outlined using the nuclear (DAPI channel) and actin (AF647 channel) stains, respectively, and then the fluorescence intensity of PEAK3 (AF488 channel) in each region was measured. Nuclear enrichment in each cell was determined post background correction as the ratio of average intensity in the nucleus to average intensity of the whole cell, excluding the nucleus. Each condition was imaged in at least three independent experiments, and the data from all cells across all experiments were combined. Statistical significance was determined using One-way ANOVA Dunnett's multiple comparisons test in Prism 9 (Graphpad Software, Inc.).

Immunoprecipitation/Mass spectrometry

Immunoprecipitation of PEAK3. One 100 mm plate of HEK293 cells (~80% confluency) was washed with ice-cold Dulbecco's PBS and lysed with 500 µL of ice-cold lysis buffer containing 20 mM Tris-HCl pH 8.0, 100 mM KCl, 5 mM $MgCl_2$, 0.1% Tween-20, 0.1% NP40, 10% glycerol, 1× protease inhibitor cocktail (Roche, complete mini-EDTA free), and 1× phosphatase inhibitor cocktail (Roche, PhosStop). Lysates were sonicated and then clarified by centrifugation at 13,000 xg for 15 min at 4 °C. For FLAG purification, 25 µL of bead slurry (Anti-FLAG M2 Magnetic Beads; Sigma-Aldrich) was washed twice with 1 mL of ice-cold wash buffer (20 mM Tris-HCl pH 8.0, 100 mM KCl, 5 mM $MgCl_2$, 0.1% Tween-20, 0.1% NP40, 10% glycerol), and 2 mg lysate was incubated with the anti-FLAG beads at 4 °C with rotation for 3 hours. After incubation, flow-through was removed and beads were washed three times with 1 mL of wash buffer and twice with 1 mL reduced wash buffer (20 mM Tris-HCl pH 8.0, 100 mM KCl, 5mM $MgCl_2$). Bound proteins were eluted by incubating beads with 15 µL of 100 ug/mL 3xFLAG

peptide in 0.05% RapiGest in wash buffer for 15 min at room temperature with shaking. Supernatants were removed and elution was repeated.

Preparation of samples for MS. For immunoprecipitated PEAK3 from HEK293 cells, eluates were combined and 10 µL of 8 M urea, 250 mM Tris, 5 mM DTT (final concentration ~1.7 M urea, 50 mM Tris, and 1 mM DTT) was added to give a final total volume of ~45 µL. Samples were incubated at 60 °C for 15 min and allowed to cool to room temperature. IODO was added to a final concentration of 3 mM and the mixture was incubated at room temperature for 45 min in the dark. DTT was added to a final concentration of 3 mM before adding 1 µg of sequencing-grade trypsin (Promega) and incubating at 37 °C overnight. Samples were acidified to 1% trifluoroacetic acid (TFA, pH < 2) with 20% TFA stock and incubated for 30 min before desalting on C18 stage tip.

For purified PEAK3/14-3-3 complexes, 5 ug of the purified protein complex was resuspended in 10 µL of 8 M urea, 50 mM Tris, 1 mM DTT. Samples were incubated at 60 °C for 15 min and allowed to cool to room temperature. IODO was added to a final concentration of 3 mM and the mixture was incubated at room temperature for 45 min in the dark. DTT was added to a final concentration of 3 mM and the sample was then diluted with 90 µL of 50 mM Tris before adding 0.1 µg of sequencing-grade trypsin (Promega) and incubating at 37 °C overnight. Samples were acidified to 1% trifluoroacetic acid (TFA, pH < 2) with 20% TFA stock and incubated for 30 min before desalting on C18 stage tip.

MS data acquisition and analysis. For AP-MS, samples from each condition (non-transduced HEK293 lysate (Control), WT and S69A PEAK3-3xFLAG) were acquired as biological quadruplicate. For the purified PEAK3/14-3-3 complex experiment, one acquisition was performed. For AP-MS and purified PEAK3/14-3-3 complex experiments, samples were

resuspended in 15 µL of MS loading buffer (1% formic acid) and 2 µL was separated by a reversed-phase gradient over a nanoflow 75 µm internal diameter × 25 cm long picotip column packed with 1.9 µM C18 particles (Dr. Maisch) using an EASY nLC (ThermoFisher Scientific) at 300nl/min. Gradient details are described in the Source Data file. Peptides were directly injected over the course of a 75 min acquisition into a Q-Exactive Plus mass spectrometer (ThermoFisher Scientific). MS acquisition setting are detailed in the Source Data file.

Raw MS data were searched against the Uniprot canonical isoforms of the human proteome (Downloaded January 2020) using the default settings in MaxQuant (version 1.6.12.0; see detailed settings in the Source Data file), with a match-between-runs enabled[71]. Peptides and proteins were filtered to 1% FDR in MaxQuant, and identified proteins were then subjected to PPI scoring. To quantify changes in interactions between WT and mutant baits, we used a label-free quantification approach in which statistical analysis was performed using MSstats[72] from within the artMS Bioconductor R (version 4.1.1) package (Log2 Fold change were mapped onto the network resulting from SAINT analysis with no pValue cutoff, see Source Data file). All raw data files and search results are available from the Pride partner ProteomeXchange repository under the PXD035574 identifier[73,74]. Detailed MS acquisition and MaxQuant search parameters are provided in the Source Data file. The resulting network was built in Cytoscape (version 3.8), supplemented from STRING database (version 11.5), and log2 fold change of WT compared mutant preys as determined by artMS (see Source Data file) was mapped onto the network.

PPI scoring. Protein spectral intensities as determined by MaxQuant search results were used for PPI confidence scoring by SAINTexpress (version 3.6.1)[75]. For SAINTexpress, control samples in which bait protein was not transduced were used. Candidate PPIs were filtered to those that displayed a SAINTexpress BFDR <0.05.

Sequence bioinformatics

In order to generate the sequence logo for PEAK3's 14-3-3 binding site, PEAK3 homologs were collected by BLAST search in the NCBI RefSeq protein sequence database (E-value threshold 0.00001). Orthologs of PEAK1 and PEAK2 were filtered out manually, leaving 251 homologs. Sequences thus collected were cleared of redundancy by clustering at sequence identity threshold 0.8 using MMSEQ (version 1.0.11)[76] and aligned using Mafft v7[77]. The Mafft sequence alignment served to generate the sequence logo using the Weblogo 3 algorithm[78].

ADP-Glo in-vitro kinase assay

20 nM recombinant PKD2 (Thermo Scientific, PV3758) was incubated with 100 μM ATP and 5 mM $MgCl_2$ in 50 mM Tris-HCL, pH 7.5, 150 mM NaCl, 1 mM DTT for 1 hour at room temperature to allow for autophosphorylation and activation of the kinase. Substrate peptides were then added to the reaction mixture at a final concentration of 100 μM and a final volume of 10 μL, followed by incubation for 1 hour at 30 °C. Next, the ADP-Glo manufacturer's protocol was followed to quench the reaction and detect substrate phosphorylation via the coupled luciferin/luciferase reaction (Promega, V9101). Reactions were transferred to a 384-well white low volume microplate (Corning, 3825) and luminescence was read using a Synergy H1 plate reader in luminescence mode (Biotek). Luminescence values were averaged for each sample and then normalized to the maximum value for a given day. The normalized data was then averaged across experiments from multiple days. Statistical significance was determined using One-way ANOVA Dunnett's multiple comparisons test in Prism 9 (Graphpad Software, Inc.).

REFERENCES

1. Kucukelbir, A., Sigworth, F. J. & Tagare, H. D. Quantifying the local resolution of cryo-EM density maps. *Nature methods* **11**, 63-65 (2014).
2. Madeira, F. *et al.* 14-3-3-Pred: improved methods to predict 14-3-3-binding phosphopeptides. *Bioinformatics* **31**, 2276-2283 (2015).
3. DiMaio, F. *et al.* Atomic-accuracy models from 4.5-Å cryo-electron microscopy data with density-guided iterative local refinement. *Nature methods* **12**, 361-365 (2015).
4. Punjani, A., Rubinstein, J. L., Fleet, D. J. & Brubaker, M. A. cryoSPARC: algorithms for rapid unsupervised cryo-EM structure determination. *Nature methods* **14**, 290-296 (2017).
5. Zivanov, J. *et al.* New tools for automated high-resolution cryo-EM structure determination in RELION-3. *elife* **7**, e42166 (2018).
6. Tan, Y. Z. *et al.* Addressing preferred specimen orientation in single-particle cryo-EM through tilting. *Nature methods* **14**, 793-796 (2017).
7. Arthur, J. S. C. & Ley, S. C. Mitogen-activated protein kinases in innate immunity. *Nature Reviews Immunology* **13**, 679-692 (2013).
8. Cargnello, M. & Roux, P. P. Activation and function of the MAPKs and their substrates, the MAPK-activated protein kinases. *Microbiology and molecular biology reviews* **75**, 50-83 (2011).
9. Lavoie, H. & Therrien, M. Regulation of RAF protein kinases in ERK signalling. *Nature reviews Molecular cell biology* **16**, 281-298 (2015).
10. Newton, A. C. Protein kinase C: poised to signal. *American Journal of Physiology-Endocrinology and Metabolism* (2010).

11. Mace, P. D. & Murphy, J. M. There's more to death than life: Noncatalytic functions in kinase and pseudokinase signaling. *Journal of Biological Chemistry* **296** (2021).

12. Kung, J. E. & Jura, N. Structural Basis for the Non-catalytic Functions of Protein Kinases. **24**, 7-24 (2016).

13. Patel, O., Roy, M. J., Murphy, J. M. & Lucet, I. S. The PEAK family of pseudokinases, their role in cell signalling and cancer. **45**, 665 (2019).

14. Paul, M. D., Torosyan, H. & Jura, N. Piquing our interest: Insights into the role of PEAK3 in signaling and disease. *Science Signaling* **15**, eabm9396 (2022).

15. Wang, Y. *et al.* Pseudopodium-enriched atypical kinase 1 regulates the cytoskeleton and cancer progression [corrected]. **107**, 10920-10925 (2010).

16. Croucher, D. R. *et al.* Involvement of Lyn and the atypical kinase SgK269/PEAK1 in a basal breast cancer signaling pathway. **73**, 1969-1980 (2013).

17. Zheng, Y. *et al.* Temporal regulation of EGF signalling networks by the scaffold protein Shc1. **499**, 166-171 (2013).

18. Tanaka, H., Katoh, H. & Negishi, M. Pragmin, a Novel Effector of Rnd2 GTPase, Stimulates RhoA Activity. **281**, 10355-10364 (2006).

19. Safari, F., Murata-Kamiya, N., Saito, Y. & Hatakeyama, M. Mammalian Pragmin regulates Src family kinases via the Glu-Pro-Ile-Tyr-Ala (EPIYA) motif that is exploited by bacterial effectors. **108**, 14938-14943 (2011).

20. Senda, Y., Murata-Kamiya, N. & Hatakeyama, M. C-terminal Src kinase-mediated EPIYA phosphorylation of Pragmin creates a feed-forward C-terminal Src kinase activation loop that promotes cell motility. *Cancer science* **107**, 972-980 (2016).

21. Lecointre, C. *et al.* Dimerization of the Pragmin Pseudo-Kinase Regulates Protein Tyrosine Phosphorylation. **26**, 545-554.e544 (2018).

22. Lopez, M. L. *et al.* PEAK3/C19orf35 pseudokinase, a new NFK3 kinase family member, inhibits CrkII through dimerization. **116**, 15495-15504 (2019).

23. Hou, J. *et al.* Distinct PEAK3 interactors and outputs expand the signaling potential of the PEAK pseudokinase family. *Science Signaling* **15**, eabj3554 (2022).

24. Ounoughene, Y. *et al.* SHED-Dependent Oncogenic Signaling of the PEAK3 Pseudo-Kinase. *Cancers* **13**, 6344 (2021).

25. Patel, O. *et al.* Production and purification of the PEAK pseudokinases for structural and functional studies. *Methods in Enzymology* **667**, 1-35 (2022).

26. Ha, B. H. & Boggon, T. J. The crystal structure of pseudokinase PEAK1 (Sugen Kinase 269) reveals an unusual catalytic cleft and a novel mode of kinase fold dimerization. (2017).

27. Patel, O. *et al.* Structure of SgK223 pseudokinase reveals novel mechanisms of homotypic and heterotypic association. **8**, 1157 (2017).

28. Liu, L. *et al.* Homo- and Heterotypic Association Regulates Signaling by the SgK269/PEAK1 and SgK223 Pseudokinases. *Journal of Biological Chemistry* **291**, 21571-21583 (2016).

29. Masters, S. *et al.* Survival-promoting functions of 14-3-3 proteins. *Biochemical Society Transactions* **30**, 360-365 (2002).

30. Aitken, A. in *Seminars in cell & developmental biology.* 673-680 (Elsevier).

31. Cornell, B. & Toyo-Oka, K. 14-3-3 proteins in brain development: neurogenesis, neuronal migration and neuromorphogenesis. *Frontiers in molecular neuroscience* **10**, 318 (2017).

32. Abdrabou, A., Brandwein, D. & Wang, Z. Differential subcellular distribution and translocation of seven 14-3-3 isoforms in response to EGF and during the cell cycle. *International Journal of Molecular Sciences* **21**, 318 (2020).

33. Kondo, Y. *et al.* Cryo-EM structure of a dimeric B-Raf:14-3-3 complex reveals asymmetry in the active sites of B-Raf kinases. **366**, 109-115 (2019).

34. Park, E. *et al.* Architecture of autoinhibited and active BRAF–MEK1–14-3-3 complexes. 1-29 (2019).

35. Yang, X. *et al.* Structural basis for protein–protein interactions in the 14-3-3 protein family. *Proceedings of the National Academy of Sciences* **103**, 17237-17242 (2006).

36. Karlberg, T. *et al.* 14-3-3 proteins activate Pseudomonas exotoxins-S and-T by chaperoning a hydrophobic surface. *Nature communications* **9**, 1-11 (2018).

37. Ren, Y. *et al.* CIC is a mediator of the ERK1/2-DUSP6 negative feedback loop. *IScience* **23**, 101635 (2020).

38. Petosa, C. *et al.* 14-3-3ζ binds a phosphorylated Raf peptide and an unphosphorylated peptide via its conserved amphipathic groove. *Journal of Biological Chemistry* **273**, 16305-16310 (1998).

39. Zheng, J. *et al.* 2.2 Å refined crystal structure of the catalytic subunit of cAMP-dependent protein kinase complexed with MnATP and a peptide inhibitor. *Acta Crystallographica Section D: Biological Crystallography* **49**, 362-365 (1993).

40. Obsil, T. & Obsilova, V. in *Seminars in cell & developmental biology.* 663-672 (Elsevier).

41. Liau, N. P. D. *et al.* Negative regulation of RAF kinase activity by ATP is overcome by 14-3-3-induced dimerization. 1-20 (2020).

42. Davezac, N. *et al.* Regulation of CDC25B phosphatases subcellular localization. *Oncogene* **19**, 2179-2185 (2000).

43. Muslin, A. J. & Xing, H. 14-3-3 proteins: regulation of subcellular localization by molecular interference. *Cellular signalling* **12**, 703-709 (2000).

44. Brunet, A. *et al.* 14-3-3 transits to the nucleus and participates in dynamic nucleocytoplasmic transport. *The Journal of cell biology* **156**, 817-828 (2002).

45. Harikumar, K. B. *et al.* A novel small-molecule inhibitor of protein kinase D blocks pancreatic cancer growth in vitro and in vivo. *Molecular cancer therapeutics* **9**, 1136-1146 (2010).

46. Cha-Molstad, H., Keller, D. M., Yochum, G. S., Impey, S. & Goodman, R. H. Cell-type-specific binding of the transcription factor CREB to the cAMP-response element. *Proceedings of the National Academy of Sciences* **101**, 13572-13577 (2004).

47. Wu, J., Vajjhala, S. & O'Connor, S. A microPLC-based approach for determining kinase-substrate specificity. *ASSAY and Drug Development Technologies* **5**, 559-566 (2007).

48. Adams, D. G. *et al.* Cellular Ser/Thr-kinase assays using generic peptide substrates. *Current Chemical Genomics* **1**, 54 (2008).

49. Psenakova, K. *et al.* 14-3-3 protein directly interacts with the kinase domain of calcium/calmodulin-dependent protein kinase kinase (CaMKK2). *Biochimica et Biophysica Acta (BBA)-General Subjects* **1862**, 1612-1625 (2018).

50. Horvath, M., Petrvalska, O., Herman, P., Obsilova, V. & Obsil, T. 14-3-3 proteins inactivate DAPK2 by promoting its dimerization and protecting key regulatory phosphosites. *Communications biology* **4**, 1-14 (2021).

51. Roy, M. J. *et al.* When two is a crowd-Structural mapping of PEAK pseudokinase interactions identifies 14 3 3 as a molecular switch for PEAK3/Crk signaling. *bioRxiv*, 2022.2009. 2001.506260 (2022).

52. Bagowski, C. P., Stein-Gerlach, M., Choidas, A. & Ullrich, A. Cell-type specific phosphorylation of threonines T654 and T669 by PKD defines the signal capacity of the EGF receptor. *The EMBO Journal* **18**, 5567-5576 (1999).

53. Rey, O., Sinnett-Smith, J., Zhukova, E. & Rozengurt, E. Regulated nucleocytoplasmic transport of protein kinase D in response to G protein-coupled receptor activation. *Journal of Biological Chemistry* **276**, 49228-49235 (2001).

54. Brändlin, I. *et al.* Protein kinase C (PKC) η-mediated PKCμ activation modulates ERK and JNK signal pathways. *Journal of Biological Chemistry* **277**, 6490-6496 (2002).

55. Sinnett-Smith, J., Zhukova, E., Hsieh, N., Jiang, X. & Rozengurt, E. Protein kinase D potentiates DNA synthesis induced by Gq-coupled receptors by increasing the duration of ERK signaling in swiss 3T3 cells. *Journal of Biological Chemistry* **279**, 16883-16893 (2004).

56. Rozengurt, E., Rey, O. & Waldron, R. T. Protein kinase D signaling. *Journal of Biological Chemistry* **280**, 13205-13208 (2005).

57. Roy, A., Ye, J., Deng, F. & Wang, Q. J. Protein kinase D signaling in cancer: A friend or foe? *Biochimica et Biophysica Acta (BBA)-Reviews on Cancer* **1868**, 283-294 (2017).

58. Freeman, A. K. & Morrison, D. K. in *Seminars in cell & developmental biology.* 681-687 (Elsevier).

59. Wang, Y. *et al.* The RAS effector RIN1 directly competes with RAF and is regulated by 14-3-3 proteins. *Molecular and cellular biology* **22**, 916-926 (2002).

60. Vega, R. B. *et al.* Protein kinases C and D mediate agonist-dependent cardiac hypertrophy through nuclear export of histone deacetylase 5. *Molecular and cellular biology* **24**, 8374-8385 (2004).

61. Nishino, T. G. *et al.* 14-3-3 regulates the nuclear import of class IIa histone deacetylases. *Biochemical and biophysical research communications* **377**, 852-856 (2008).

62. Zheng, S. Q. *et al.* MotionCor2: anisotropic correction of beam-induced motion for improved cryo-electron microscopy. *Nature methods* **14**, 331-332 (2017).

63. De la Rosa-Trevín, J. *et al.* Scipion: A software framework toward integration, reproducibility and validation in 3D electron microscopy. *Journal of structural biology* **195**, 93-99 (2016).

64. Pettersen, E. F. *et al.* UCSF ChimeraX: Structure visualization for researchers, educators, and developers. *Protein Science* **30**, 70-82 (2021).

65. Emsley, P. & Cowtan, K. Coot: model-building tools for molecular graphics. *Acta crystallographica section D: biological crystallography* **60**, 2126-2132 (2004).

66. Croll, T. I. ISOLDE: a physically realistic environment for model building into low-resolution electron-density maps. *Acta Crystallographica Section D: Structural Biology* **74**, 519-530 (2018).

67. Williams, C. J. *et al.* MolProbity: More and better reference data for improved all-atom structure validation. *Protein Science* **27**, 293-315 (2018).

68. Afonine, P. V. *et al.* Real-space refinement in PHENIX for cryo-EM and crystallography. *Acta Crystallographica Section D: Structural Biology* **74**, 531-544 (2018).

69. Pintilie, G. *et al.* Measurement of atom resolvability in cryo-EM maps with Q-scores. *Nature methods* **17**, 328-334 (2020).

70. Pettersen, E. F. *et al.* UCSF Chimera--a visualization system for exploratory research and analysis. **25**, 1605-1612 (2004).

71. Cox, J. & Mann, M. MaxQuant enables high peptide identification rates, individualized ppb-range mass accuracies and proteome-wide protein quantification. *Nature biotechnology* **26**, 1367-1372 (2008).

72. Choi, M. *et al.* MSstats: an R package for statistical analysis of quantitative mass spectrometry-based proteomic experiments. *Bioinformatics* **30**, 2524-2526 (2014).

73. Vizcaíno, J. A. *et al.* ProteomeXchange provides globally coordinated proteomics data submission and dissemination. *Nature biotechnology* **32**, 223-226 (2014).

74. Perez-Riverol, Y. *et al.* The PRIDE database resources in 2022: a hub for mass spectrometry-based proteomics evidences. *Nucleic acids research* **50**, D543-D552 (2022).

75. Teo, G. *et al.* SAINTexpress: improvements and additional features in Significance Analysis of INTeractome software. *Journal of proteomics* **100**, 37-43 (2014).

76. Hauser, M., Steinegger, M. & Söding, J. MMseqs software suite for fast and deep clustering and searching of large protein sequence sets. *Bioinformatics* **32**, 1323-1330 (2016).

77. Katoh, K., Rozewicki, J. & Yamada, K. D. MAFFT online service: multiple sequence alignment, interactive sequence choice and visualization. *Briefings in bioinformatics* **20**, 1160-1166 (2019).

78. Crooks, G. E., Hon, G., Chandonia, J.-M. & Brenner, S. E. WebLogo: a sequence logo generator. **14**, 1188-1190 (2004).

Chapter 2: Structural characterization of the PI3Kα/KRas complex on membranes

ABSTRACT

PI3Kα serves as a central regulator of cell signaling by phosphorylating the membrane lipid phosphatidylinositol (4,5)-bisphosphate, producing the essential second messenger, phosphatidylinositol (3,4,5)-trisphosphate. This function relies on the recruitment of PI3Kα to the plasma membrane and its subsequent activation by two key effectors: receptor tyrosine kinases (RTKs) and Ras GTPases. Synergistic activation of PI3Kα by RTKs and Ras amplifies PI3Kα signaling, leading to the promotion of tumorigenesis, particularly in Ras-driven cancers. However, the molecular mechanisms governing PI3Kα activation at the membrane remain unclear, given the absence of any structures of active-state PI3Kα complexes. Here, we elucidate the mechanism of PI3Kα activation by presenting a series of membrane-bound PI3Kα/KRas cryo-EM structures which showcase the stepwise conformational changes associated with PI3Kα activation. When bound to POPC/POPS nanodiscs, both PI3Kα and KRas interface with the membrane and PI3Kα adopts three distinct conformations depicting the gradual release of key inhibitory domains from its catalytic core. Incorporation of PIP2 into the nanodiscs triggers a significant reorientation of PI3Kα relative to the membrane, bringing the active site in direct contact with membrane lipids. This leads to a 180° rotation of helix kα12 towards the active site, accompanied by an extension of the activation loop towards the membrane. Upon rearranging, the activation loop and helix kα12 sandwich the PIP2 substrate, trapping it within the active site for phosphorylation. Remarkably, the introduction of an RTK-derived phosphopeptide induces dimerization of the PI3Kα-KRas complex facilitated by the p110α catalytic subunit of PI3Kα, an interface which is sterically occluded in auto-inhibited PI3Kα.

INTRODUCTION

The lipid kinase PI3Kα is among the most heavily mutated proteins in cancer[1-6]. Upon activation by receptor tyrosine kinases (RTKs), PI3Kα phosphorylates the membrane lipid phosphatidylinositol 4,5-bisphosphate (PIP2), generating PIP3. PIP3 drives AKT signaling, regulating cell growth, survival, and proliferation[7,8]. The oncogenic potential of PI3Kα is further amplified by its interaction with another highly mutagenic protein, its effector Ras[9,10]. Membrane-localized and GTP-bound Ras enhances PI3Kα activation both in vitro and in vivo, inducing tumorigenesis[9,11-13]. However, the exact mechanism behind the synergistic signaling between PI3Kα, RTKs and Ras remains unclear.

Due to its oncogenic potential, the activation of PI3Kα requires tight regulation which is dictated by its core architecture. PI3Kα functions as a heterodimer composed of a p85α regulatory subunit and a p110α catalytic subunit, in which p85α inhibits the catalytic activity of p110α through a complex network of interactions[7]. Within its N-terminus, p85α contains an SH3 and BH domain, the latter of which is flanked by two proline-rich motifs. Interestingly, these domains have been implicated in PI3Kα dimerization, both in the context of the PI3K heterodimer as well as p85 alone, leading to regulation of its phosphatase, PTEN, among other functions[14-17]. The C-terminal end is comprised of two SH2 domains, termed the nSH2 and cSH2 domains, separated by the inter-SH2 (iSH2) domain. The n and cSH2 domains play pivotal roles in the recruitment and activation of PI3Kα. By binding to phosphorylated YXXM motifs on RTK c-terminal tails, the SH2 domains of p85 facilitate recruitment of PI3Kα to the membrane, thereby leading to the activation of the enzyme.

The catalytic subunit contains the adaptor binding domain (ABD), Ras binding domain (RBD), C2, helical and kinase domains. Extensive biochemical studies have identified three key

inhibitory interfaces crucial to PI3Kα auto-inhibition[18-25]. The primary and most extensive interface is formed between the nSH2 domain of p85α and the C2, helical and kinase domains of p110α. The second interface involves the iSH2 domain which makes additional inhibitory contacts with the C2 and kinase domains. Lastly, the third interface is composed of intra-subunit interactions between the ABD and kinase domains of p110α. HDX-MS studies have revealed that upon activation by phosphopeptides derived from RTKs, these inhibitory interfaces are disrupted and that oncogenic mutations in p110α mimic these very conformational changes to hyperactivate the enzyme[19,24,26-28].

A mechanistic understanding of PI3Kα signaling in physiology and disease requires high-resolution structural characterization of PI3Kα in the appropriate membrane environment, interacting with a phosphorylated RTK tail, PIP2 and Ras. Although over 50 structures of PI3Kα have been solved to date, a true active state structure of any PI3K—such as the one described above—remains elusive. Far from possessing a comprehensive understanding of PI3K activation, we even lack structural insight into the engagement of PI3Kα with any of these individual inputs. In this study, we use cryo-electron microscopy to elucidate membrane-bound structures of PI3Kα in the presence of KRas, PIP2, and an activating RTK phosphopeptide, unveiling the dynamic rearrangement of PI3Kα during activation.

RESULTS

Multi-state structures of the PI3Kα/KRas complex bound to POPC/POPS membranes

To date, PI3Kα has only been structurally characterized in solution, in the absence of a lipid bilayer. This is likely due to the transient nature of PI3Kα/membrane interactions, which make it challenging to capture and stabilize them in-vitro for high-resolution structural studies. To address this technical challenge, we produced a GppNHp-loaded, farnesylated, and methylated KRas from insect cells which readily integrates into synthetic membranes. Additionally, we utilized a compound which binds at the predicted PI3Kα/Ras interface and acts as a molecular glue, stabilizing PI3Kα binding to Ras and, in turn, the membrane. With these tools, we reconstituted the PI3Kα/KRas complex on lipid nanodiscs composed of POPC/POPS lipids and the membrane scaffold protein, 1E3D1 (MSP1E3D1) **(Fig. 2.1 a, b)**. This approach not only stabilized PI3Kα at the membrane but also allowed us to study it in the context of its physiological effector, Ras.

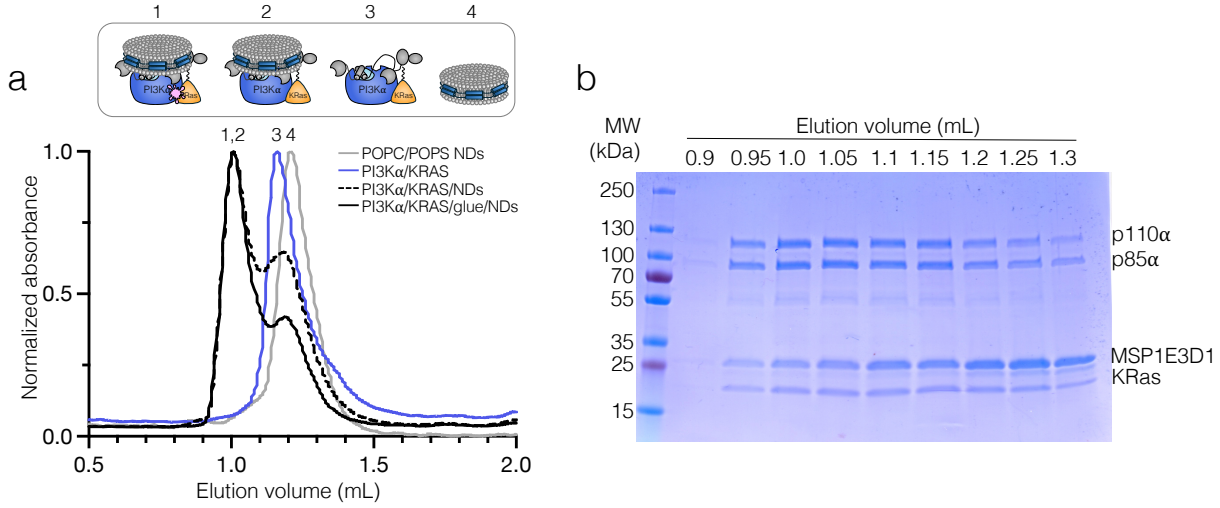


Figure 2.1: In-vitro reconstitution of the PI3Kα/KRas complex bound to POPC/POPS membranes

a Representative size exclusion chromatography profiles of POPC/POPS/MSP1E3D1 nanodiscs (grey), PI3Kα/KRas complex (violet), PI3Kα/KRas complex on nanodiscs (black, dotted), and PI3Kα/KRas/molecular glue complex on nanodiscs (black) resolved on a Superdex 200 Increase 3.2/300 column. **b** Corresponding Coomassie-stained SDS-PAGE analysis of the purified PI3Kα/KRas/molecular glue complex on nanodiscs.

Structural analysis of this complex by cryo-EM on graphene-oxide (GO) grids yielded reconstructions of three distinct states at resolutions of 3.01 Å , 3.23 Å and 3.05 Å: Class 1, Class 2, and Class 3, respectively **(Fig. 2.2)**. In all three classes, both the catalytic core of p110α and the C-terminus of KRas make interactions with the nanodisc. However, the angle (~45°) and distance (~33 Å) of the PI3Kα active site relative to the membrane appear incompatible with catalysis **(Fig. 2.3 b)**. Interestingly, the three classes depict conformational rearrangements between p85α and p110α along the activation pathway of PI3Kα. In the first reconstruction class (class 1), two inhibitory domains, iSH2 of p85α and ABD of p110α, are well resolved along with the remainder of p110α. However, the nSH2 domain of p85α, is only visible in a 8 Å low-pass filtered map, indicating its low occupancy, and suggesting the displacement of this crucial inhibitory domain from p110α upon association of PI3Kα with KRas and the membrane **(Fig.**

2.3 c, right). The second reconstruction class (class 2) adopts an intermediate conformation, in which the nSH2-p110α interactions are completely disrupted while iSH2 and ABD interactions with p110α become more dynamic and thus poorly resolved **(Fig. 2.3 c, middle)**. Finally, in the third and most active-like reconstruction (class 3), all three inhibitory interfaces, involving the nSH2, iSH2 and ABD domains, are disrupted, with the iSH2 and ABD domains only partially observed in low-pass filtered maps, indicating significant rearrangements and increased flexibility within the inhibitory framework of the PI3Kα heterodimer **(Fig. 2.3 c, right)**.

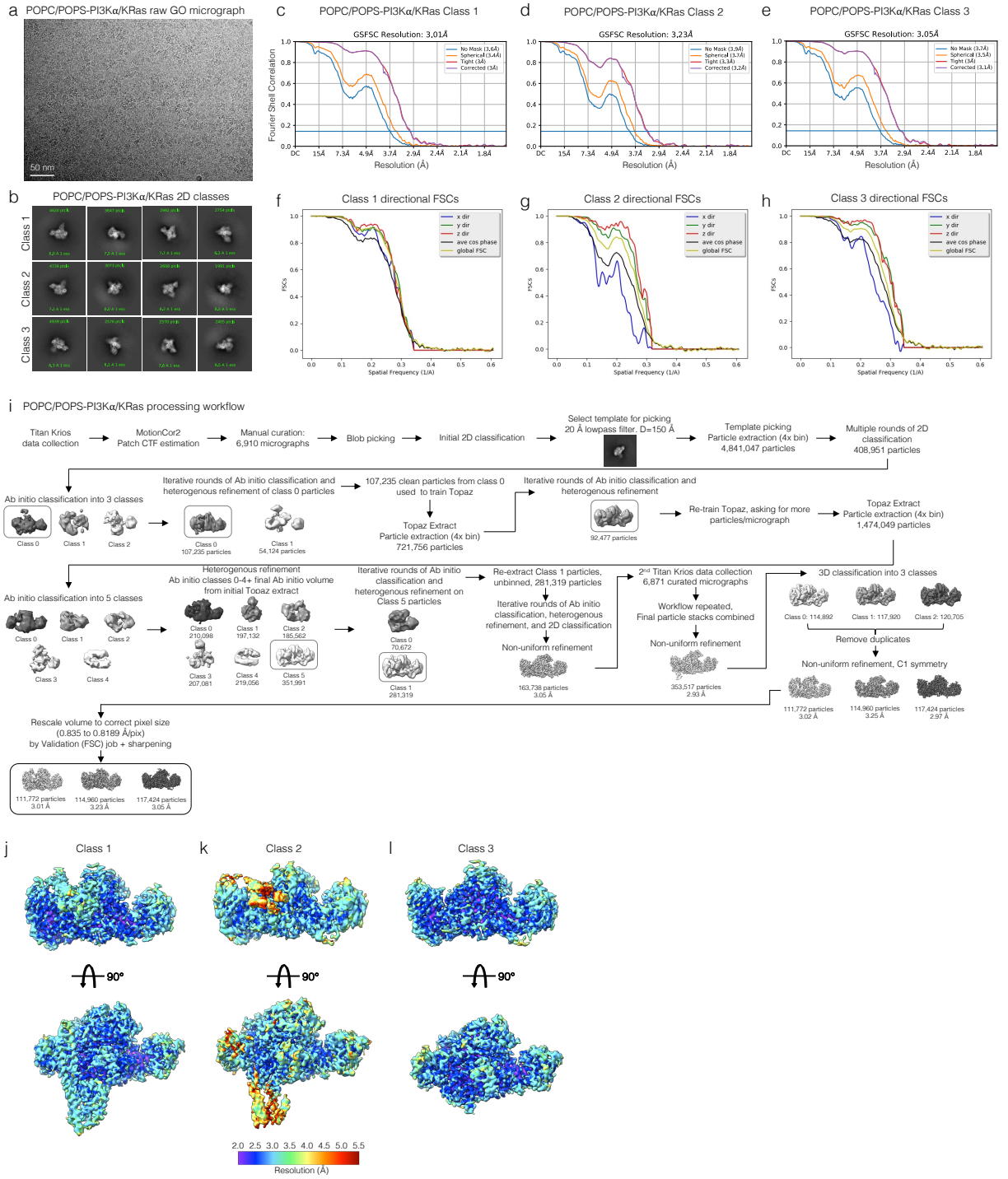


Figure 2.2: Resolution estimation, map quality and processing workflow for the POPC/POPS-PI3Kα/KRas complex dataset

a Representative micrograph of the POPC/POPS-PI3Kα/KRas complex sample on Quantifoil R1.2/1.3 300 mesh Au holey-carbon graphene oxide grids from a dataset of 13,781 micrographs. The scale bar corresponds to 50 nm. (Figure caption continued on the next page.)

Figure 2.2: Resolution estimation, map quality and processing workflow for the POPC/POPS-PI3Kα/KRas complex dataset

(Figure caption continued from the previous page.) **b** Representative cryo-EM 2D class averages of particles corresponding to class 1, class 2 and class 3 POPC/POPS-PI3Kα/KRas complexes. **c-d** Gold Standard Fourier Shell Correlation (GSFSC) of final maps used for model building for Class 1 **(c)** , Class 2 **(d)** and Class 3 **(e)** complexes from CryoSparc4. **f-h** Directional FSCs of Class 1 **(f)** , Class 2 **(g)** and Class 3 **(h)** complexes calculated by the 3DFSC server. i) Processing workflow of POPC/POPS-PI3Kα/KRas complex dataset. **j-l** Cryo-EM maps of the Class 1 **(j)**, Class 2 **(k)** and Class 3 **(l)** complexes colored according to local resolution determined by ResMap.

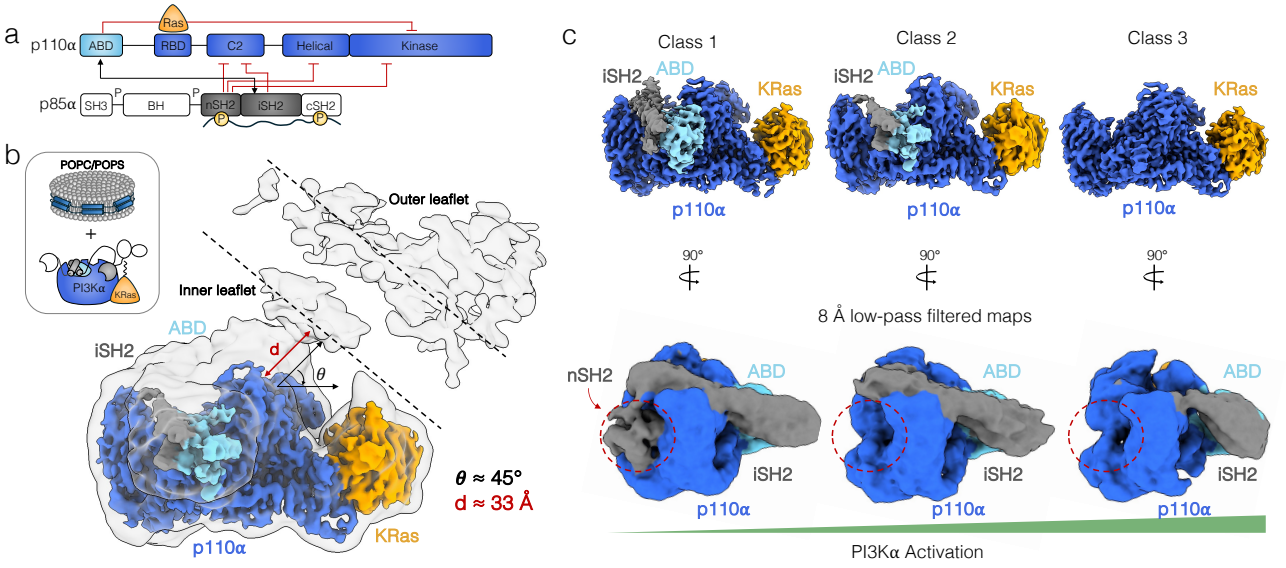


Figure 2.3: Multi-state structures of the PI3Kα/KRas complex bound to POPC/POPS membranes

a Cartoon schematic of domain structure of p85α regulatory and p110α catalytic subunits of PI3Kα. p110α is composed of an adaptor binding domain (ABD), Ras binding domain (RBD), C2, helical and kinase domains. p85α contains an SH3, Bar homology domain (BH) and two Src homology domains (nSH2 and cSH2) separated by a coiled coil domain, termed the inter-SH2 (iSH2) domain. Inter and intra-subunit inhibitory interactions are depicted with red lines and non-inhibitory interactions are illustrated with black arrows. **b** Cryo-EM map of the Class 2 PI3Kα/KRas complex bound to POPC/POPS nanodiscs overlayed with a transparent 10 Å low-pass filtered version of the same map, highlighting membrane interface. p85α is colored in grey, p110α in blue, the ABD domain of p110α in cyan, and KRas in orange. **c** Cryo-EM maps of three distinct classes of the PI3Kα/KRas complex bound to POPC/POPS nanodiscs as well as their corresponding 8 Å low-pass filtered maps, illustrating conformational changes between p85α and p110α along the PI3Kα activation pathway.

Upon release of these inhibitory interactions, the C2 domain and kinase domain of p110α rotate away from one another, as previously seen in the ΔnSH2 crystal structure of PI3Kα. This rotation is especially evident in the activation loop, as well as helices kα8 and kα11 of the kinase c-lobe **(Fig. 2.4 a)**. The activation loop, which is stabilized by the iSH2 domain in the Class 1 reconstruction, becomes more dynamic and poorly resolved in Class 2 and Class 3 states **(Fig. 2.4 b)**. Intriguingly, we note an unstructured helix kα12, folded away from the active site and situated between helices kα8 and kα11 in the Class 1 reconstruction. However, as PI3Kα adopts more active-like conformations in Classes 2 and 3, helix kα12 becomes increasingly dynamic, and loses its stabilization through its interactions with helices kα8 and kα11 **(Fig. 2.4 c)**. The gradual release of the inhibitory nSH2, iSH2 and ABD domains as well as the destabilization of the activation loop and helix kα12 observed in these three states suggest that binding to KRas and the membrane primes PI3Kα for activation **(Fig. 2.4 d)**.

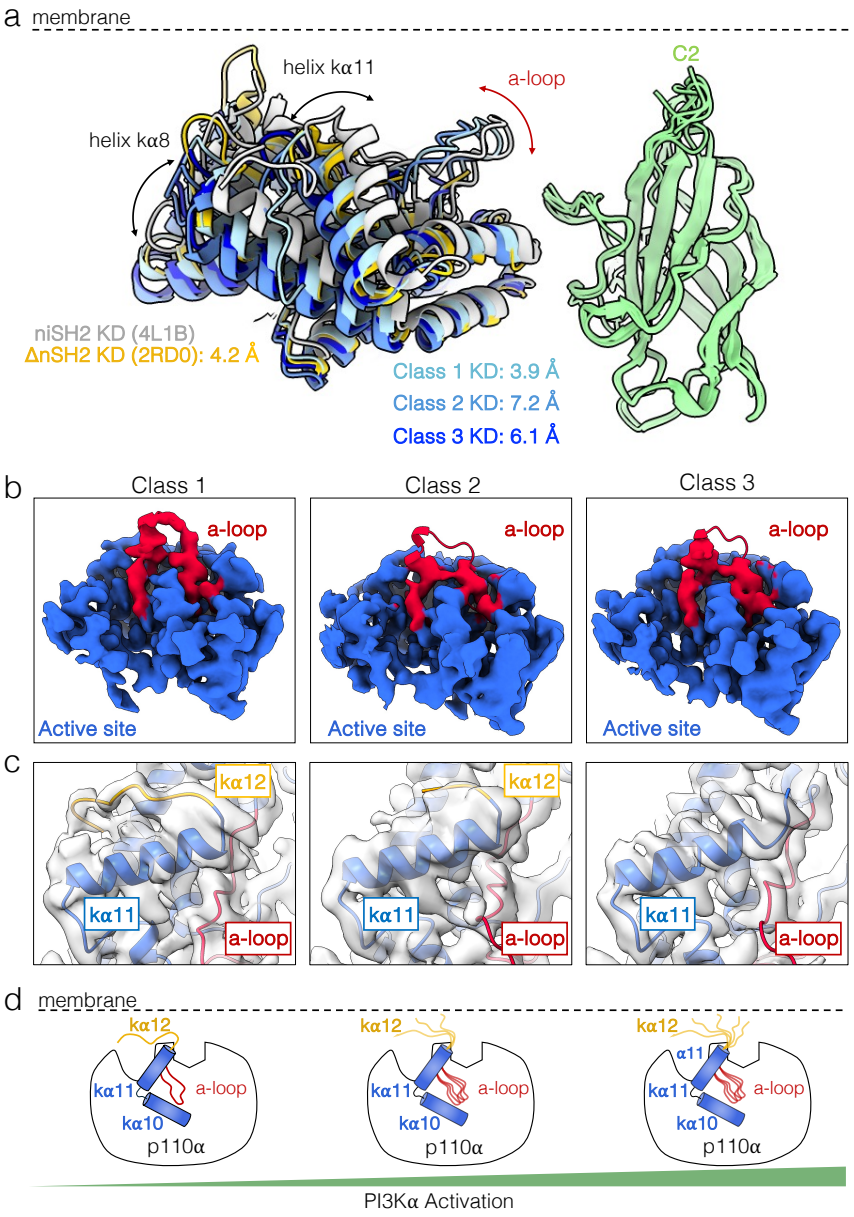


Figure 2.4: Confirmational rearrangements and increased dynamics within the PI3Kα active site upon binding to KRas and POPC/POPS membranes

a Overlay of Class 1, Class 2 and Class 3 structures with ΔnSH2 (2RD0) and niSH2 (4L1B) crystal structures of PI3Kα. Structures are aligned on the C2 domains shown in light green. Kinase domains of structures are colored as indicated in the legend. The remaining PI3Kα domains and KRas are not shown for clarity. **b** 4 Å low-pass filtered cryo-EM maps of Class 1, Class 2 and Class 3 reconstructions overlayed with their corresponding models with activation loop density highlighted in red. **c** 4 Å lowpass filtered cryo-EM maps of Class 1, Class 2 and Class 3 reconstructions overlayed with corresponding models, showing the conformation of helix kα12 in yellow. **d** Cartoon schematic summarizing the conformational changes observed in the activation loop and helix kα12 of PI3Kα in the three reconstructions of the PI3Kα/KRas complex bound to POPC/POPS membranes.

Our structures also provide insight into PI3Kα/Ras interactions. To date, there is only one structure of any PI3K bound to Ras, that of p110γ and HRas[29]. In this structure, the RBD domain of p110γ makes significant polar contacts with both the switch I and switch II regions of HRas. Interestingly, HRas makes an additional contact with the kinase domain of p110γ, suggesting a potential role for direct regulation of PI3K catalytic activity by Ras.

In our POPC/POPS-bound PI3Kα/KRas structures, the majority of the RBD/Ras interactions observed between p110γ and HRas are conserved, except for a few key differences **(Fig. 2.5 a)**. KRas undergoes an 18° rotation relative to the RBD of p110α, when compared to the p110γ/HRas complex **(Fig. 2.5 b)**. This is a common feature observed in Ras/effector complexes, serving as a mechanism through which Ras discriminates between its various effectors. Interestingly, p110α diverges slightly with regards to two sets of interactions present in the p110γ/HRas complex: one involving the 253-267 loop of the p110γ RBD which binds the switch I region of HRas, and another involving the kinase domain of p110γ which contacts the switch II region of HRas. The 253-267 loop in p110γ becomes structured upon binding to HRas, providing an additional contact point, mediated by Lys 251, Lys 255 and Ser 257, which interact with Asn 25 and Asp 33 of HRas, to stabilize the already extensive p110γ/HRas interface **(Fig. 2.5 b)**. However, in our structures, the equivalent loop in p110α (230-245) points away from the p110α/KRas interface, but still maintains interactions with Asn 25 and Asp 33 of KRas via Ser 231 and Arg 230, respectively. Instead, the pocket that accommodates the 253-267 loop of p110γ is occupied by the molecular glue **(Fig 2.5 b)**. The second contact, a salt bridge between Glu 919 of the c-lobe of the p110γ kinase domain and Arg 73 of the switch II region of HRas is absent in

p110α as the helices which house the corresponding residues in p110α (Glu 888) and KRas (Arg 73) are rotated away from one another, preventing the formation of this interaction **(Fig. 2.5 c)**.

a

Region	KRas/HRas	p110α	p110γ
N/A	N25	S231	L258, S257
Switch I	D33	R230	K251, K255
Switch I	E37	K206, T208	T232
Switch I	D38	T208, K227	K251
Switch I	S39	K206	S230
Switch I	Y40	Y207	N231
Switch I	R41	K204, N205	T228
Switch II	E63	K210	K234
Switch II	Y64	K210	K234
Switch II	R73	N/A	E919

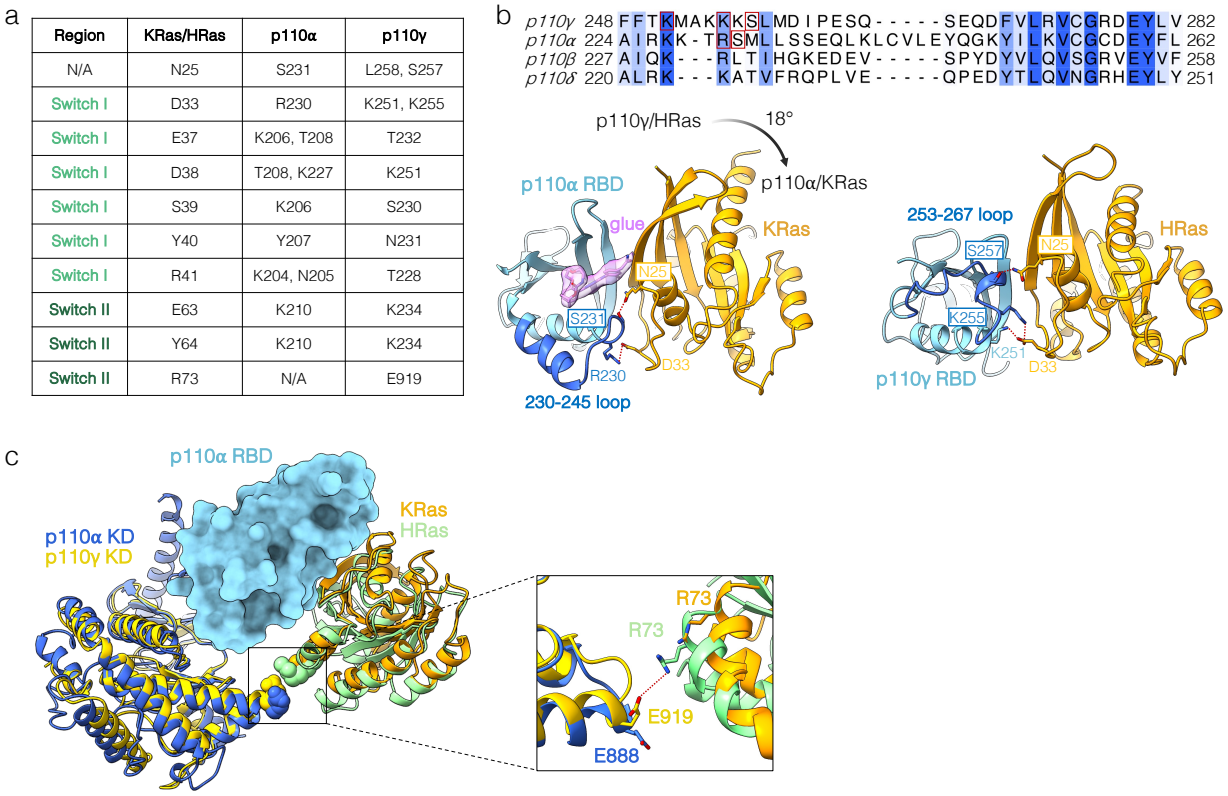


Figure 2.5: Comparison of the PI3Kα/KRas and PI3Kγ/HRas interfaces
a Interactions composing the PI3Kα/KRas and PI3Kγ/HRas (1HE8) interfaces. **b** Structure of the Class 1 PI3Kα/KRas complex, highlighting the p110α RBD/KRas(left) and p110γ RBD/HRas (right) interfaces. p110α and p110γ RBDs are colored in cyan and their corresponding 230-245 and 253-267 loops are colored in blue. The protein sequence alignment of these loop regions in Class I PI3K isoforms are shown above, with conserved residues colored in various shades of blue depending on level of conservation. p110α and p110γ residues which interface with Ras are boxed in red. Molecular glue is shown in pink overlayed with its corresponding density. **c** Overlay of the PI3Kα/KRas and PI3Kγ/HRas structures showing the interaction between the p110γ kinase domain (yellow) and HRas (light green) which is missing between p110α (blue) and KRas (orange).

PIP2 remodels the active site of PI3Kα

We next wanted to structurally characterize the interaction between the PI3Kα/KRas complex and PIP2 in the context of a lipid bilayer. Previous structural studies on the PI3Kα/PIP2 interaction have used soluble PIP2 mimetics, like diC4-PIP2[20]. However, these mimetics do not fully capture the complex lipid environment and extensive lipid surface area available to PI3Kα during substrate engagement in the cell. Thus, we incorporated 5% PIP2 into our POPC/POPS nanodiscs and reconstituted the PI3Kα/KRas complex, stabilized by the molecular glue, on these membranes **(Fig. 2.6 a, b)**. However, the excess negative charge contributed by PIP2 lead to aggregation of the sample upon application on GO grids. We therefore used GO grids functionalized with PEG-amino groups to accommodate this increase in negative charge, which resulted in well-folded and mono-dispersed particles on the grid. Structural characterization of this sample by cryo-EM yielded a 2.88 Å reconstruction of the PI3Kα/KRas complex bound to PIP2-containing nanodiscs **(Fig. 2.7)**. The addition of PIP2 dramatically altered the PI3Kα/membrane interface, reorienting PI3Kα to form a more head-on interaction with the membrane **(Fig. 2.8 a)**. Furthermore, the buried surface area between PI3Kα and the membrane increased significantly, bringing the active site of PI3Kα in direct contact with lipid densities.

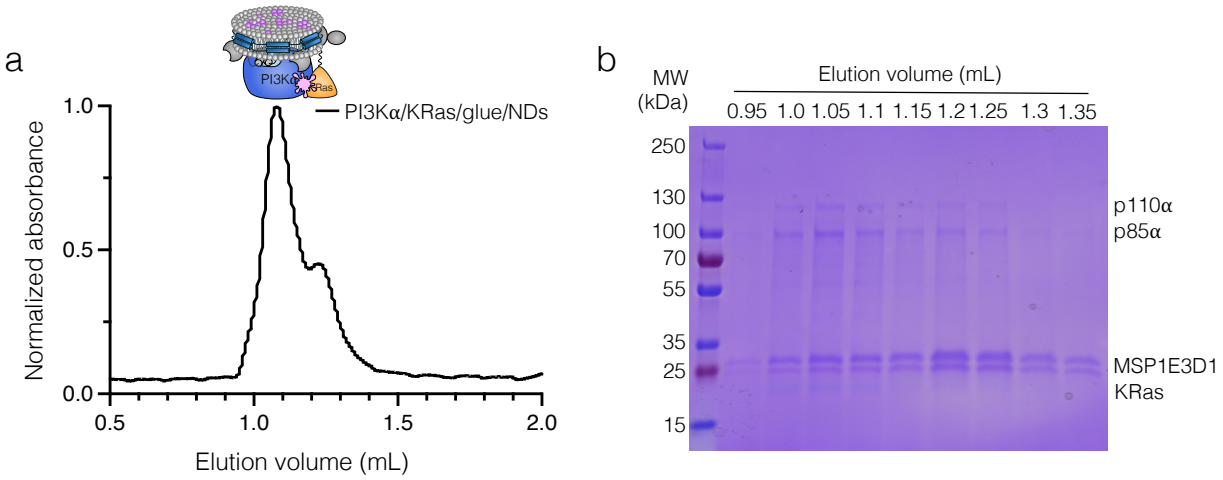


Figure 2.6: In-vitro reconstitution of the PI3Kα/KRas complex bound to POPC/POPS/PIP2 membranes

a Representative size exclusion chromatography profile of the PI3Kα/KRas complex bound to POPC/POPS/PIP2/MSP1E3D1 nanodiscs (black) resolved on a Superdex 200 Increase 3.2/300 column and **b** corresponding Coomassie-stained SDS-PAGE analysis.

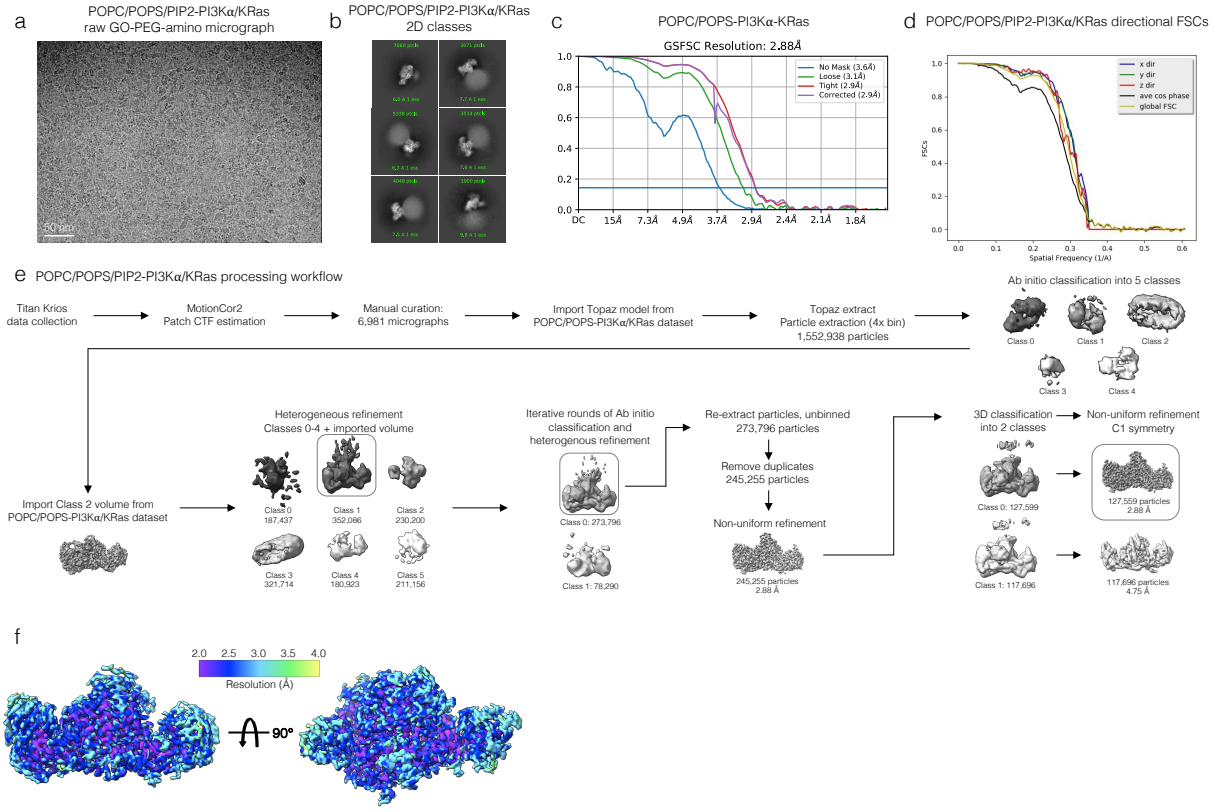


Figure 2.7: Resolution estimation, map quality and processing workflow for the POPC/POPS/PIP2-PI3Kα/KRas complex dataset

a Representative micrograph of the POPC/POPS-PI3Kα/KRas complex sample on Quantifoil R1.2/1.3 300 mesh Au holey-carbon PEG-amine functionalized graphene oxide grids from a dataset of 6,981 micrographs. The scale bar corresponds to 50 nm. **b** Representative cryo-EM 2D class averages of particles corresponding to the POPC/POPS/PIP2-PI3Kα/KRas complex. **c** Gold Standard Fourier Shell Correlation (GSFSC) of final map used for model building for the POPC/POPS/PIP2-PI3Kα/KRas complex from CryoSparc4. **d** Directional FSCs of the POPC/POPS/PIP2-PI3Kα/KRas complex calculated by the 3DFSC server. **e** Processing workflow of POPC/POPS/PIP2-PI3Kα/KRas complex dataset. f) Cryo-EM map of the POPC/POPS/PIP2-PI3Kα/KRas complex colored according to local resolution determined by ResMap.

In addition to stabilizing the membrane interface, PIP2 induced both global and local conformational rearrangements in PI3Kα. Globally, the inhibitory iSH2 and ABD domains, which are partially displaced upon binding POPC/POPS membranes, undergo complete disengagement from the catalytic core of p110α, a change necessary to accommodate the enhanced interaction of p110α with the membrane **(Fig. 2.8 a)**. Locally, the active site of PI3Kα reorganizes to facilitate PIP2 binding. Specifically, the activation loop extends towards the membrane while helix kα12 undergoes a ~180° rotation towards the active site and adopts a more defined helical structure relative to the POPC/POPS-bound Class 1 structure **(Fig. 2.8 b)**. Within helix kα12, lies the "WIF" motif, which is relatively conserved across all Class I PI3K isoforms and is known to be crucial for PI3Kα membrane binding and catalytic activity[30]. In our PIP2-bound structure, helix kα12 and the "WIF" motif play three important roles. First, helix kα12 residues Lys 1054, Met 1055, Ile 1058 and Phe 1059 stabilize the catalytic loop by forming a series of hydrogen bonds with Arg 916, His 917, Asn 918, and Ser 919 of the catalytic loop **(Fig. 2.8 c)**. Secondly, upon rotation, helix kα12 aligns against the membrane, with Trp 1050 and Trp 1057 directly interfacing with membrane densities, offering an additional anchoring point to the membrane **(Fig. 2.8 c)**. Most importantly, we observe a lipid density, which most likely corresponds to PIP2, wedged between the activation loop and helix kα12, deep within the active site. This density forms 2 distinct contacts with the activation loop, one likely involving its first basic box, and two interactions with helix kα12, consistent with residues Lys 1054 and Ile 1058 **(Fig. 2.8 d)**. Thus, our structure of the PI3Kα/KRas complex bound to a PIP2-containing lipid bilayer demonstrates that PIP2-binding alone is sufficient to induce near-complete displacement of the inhibitory iSH2 and ABD domains and reorganize the PI3Kα active site **(Fig, 2.8 e)**.

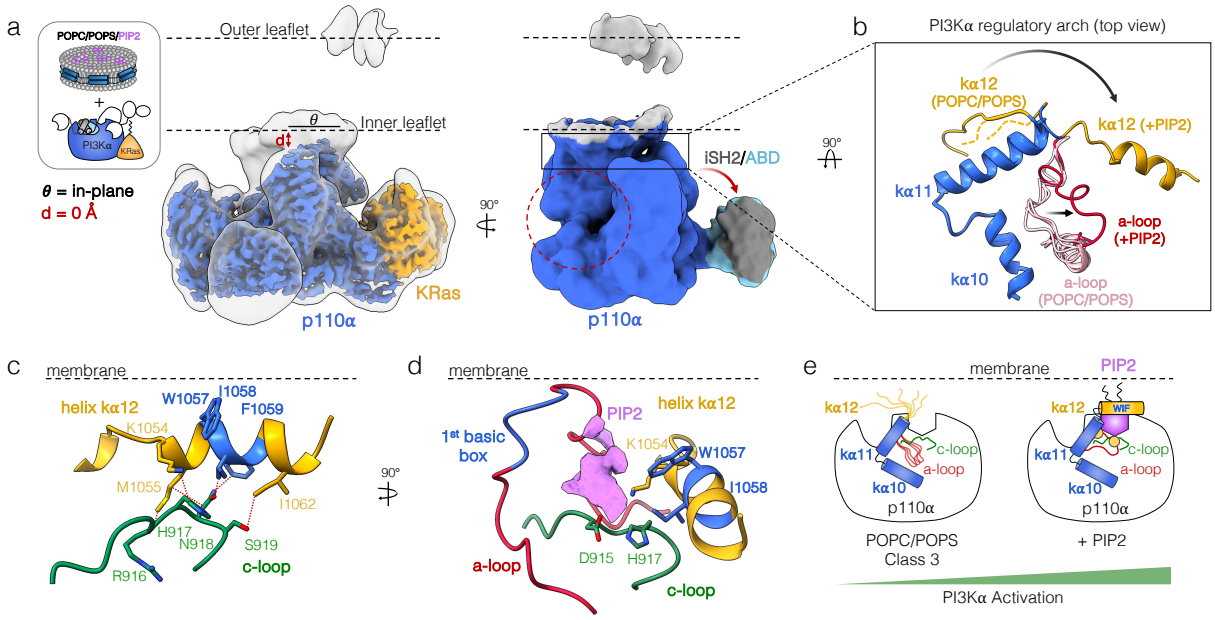


Figure 2.8: PIP2 remodels the active site of PI3Kα

a Cryo-EM map of the PI3Kα/KRas complex bound to POPC/POPS/PIP2 nanodiscs overlayed with a transparent 10 Å low-pass filtered version of the same map to highlight membrane interface (left) and an 8 Å low-pass filtered map (right) illustrating displacement of inhibitory domains from the catalytic core of p110α. **b** Overlay of POPC/POPS-bound and PIP2-bound active sites highlighting conformational changes in helix kα12 and the activation loop. kα10 and kα11 helices are colored in blue and kα12 helices are colored in yellow. POPC/POPC activation loops are colored in pink and PIP2 activation loop is colored in red. **c** Interactions between helix kα12 ("WIF" motif shown in blue) and the catalytic loop (c-loop, green) **d** PI3Kα active site of the PIP2-bound complex, showing the density for PIP2 (pink) and interacting residues of helix kα12 and catalytic loop and its proximity to the 1st basic box of the activation loop. **e** Cartoon schematic summarizing the conformational changes in the activation loop and helix kα12 of PI3Kα upon PIP2 binding.

Phosphopeptide binding induces dimerization of the PI3Kα/KRas complex

Lastly, to gain complete insight into PI3Kα activation, we reconstituted a dually activated PI3Kα on PIP2-containing lipid nanodiscs, complexed with both KRas and a YXXM bis-phosphopeptide derived from HER3, a potent activator of PI3Kα **(Fig. 2.9 a, b)**. The use of PEG-amino functionalized GO grids was especially critical for this sample because of the excess negative charge contributed by not only PIP2 but also the bis-phosphopeptide. A 2.84 Å reconstruction of this complex recapitulated the extensive and direct membrane interaction of PI3Kα seen in the PIP2-bound reconstruction in the absence of peptide **(Fig. 2.10 a; Fig. 2.11 a)**. However, peptide binding did induce additional rotation of the dislodged iSH2 and ABD domains away from the catalytic core of p110α when compared to the PIP2-only bound state **(Fig. 2.11 a, right)**.

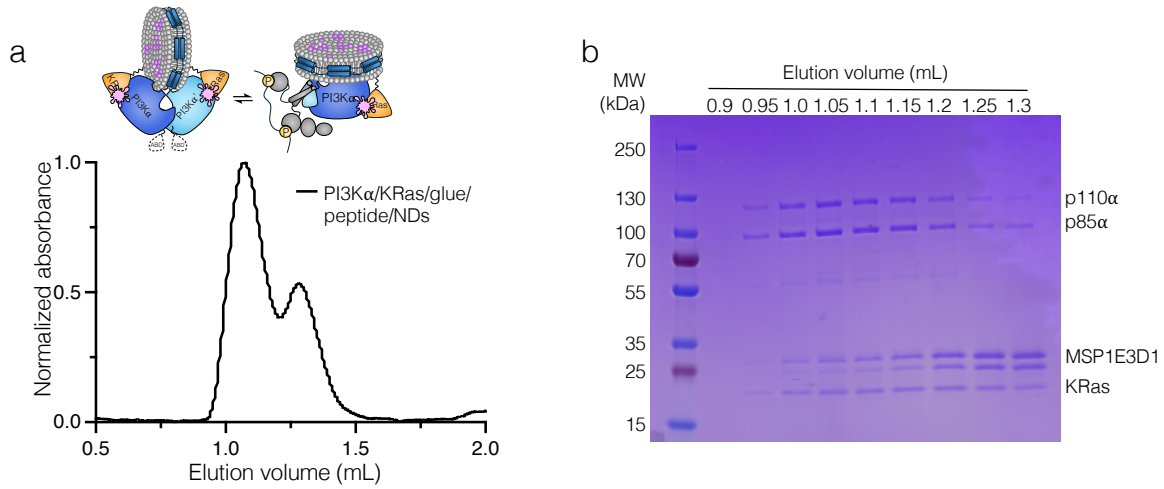


Figure 2.9: In-vitro reconstitution of the PI3Kα/KRas/peptide complex bound to POPC/POPS/PIP2 membranes

a Representative size exclusion chromatography profile of PI3Kα/KRas/peptide complex on POPC/POPS/PIP2/MSP1E3D1 nanodiscs (black) resolved on a Superdex 200 Increase 3.2/300 column and **b** corresponding Coomassie-stained SDS-PAGE analysis.

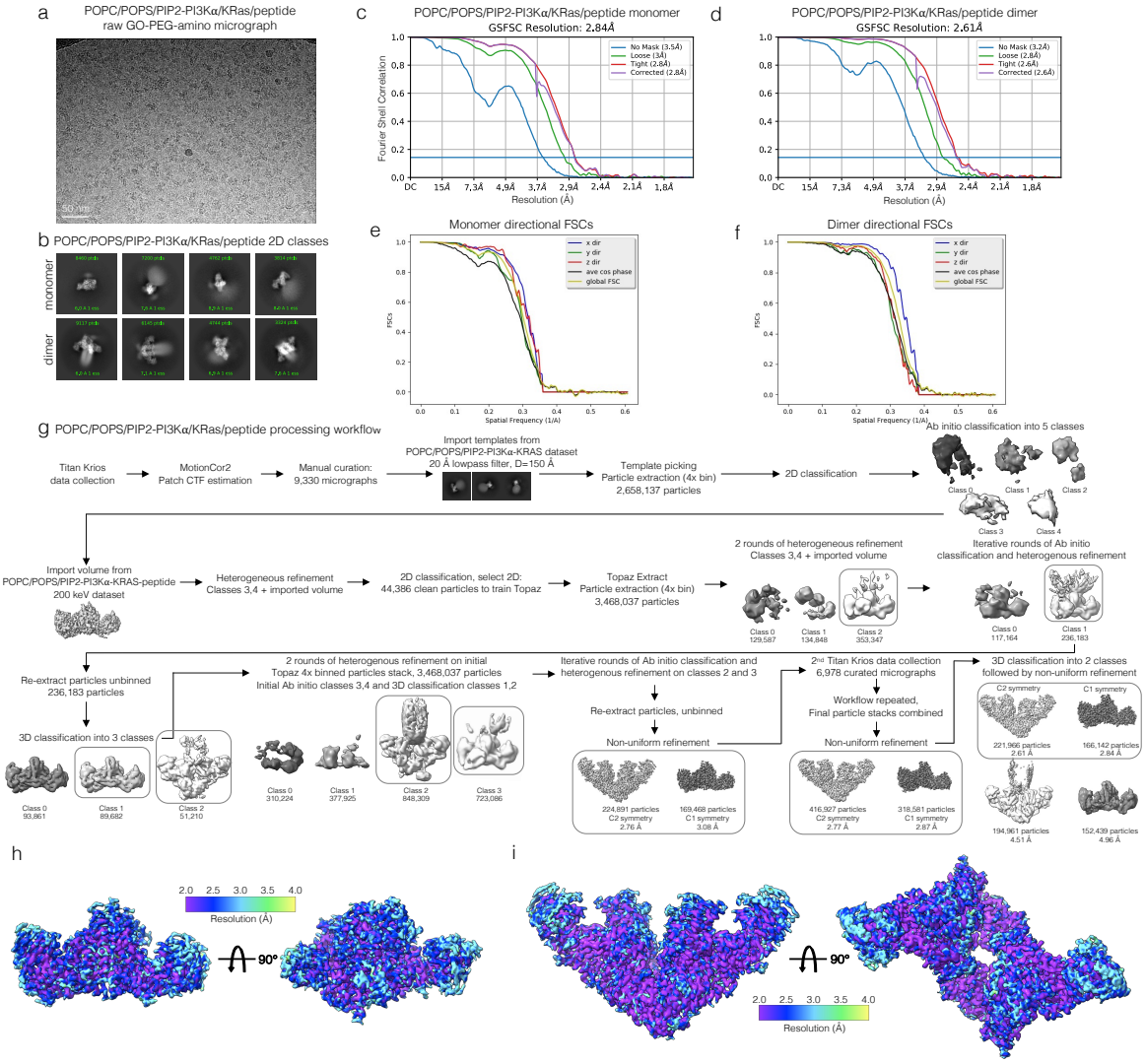


Figure 2.10: Resolution estimation, map quality and processing workflow for the POPC/POPS/PIP2-PI3Kα/KRas/peptide complex dataset

a Representative micrograph of the POPC/POPS-PI3Kα/KRas/peptide complex sample on Quantifoil R1.2/1.3 300 mesh Au holey-carbon PEG-amine functionalized graphene oxide grids from a dataset of 16,308 micrographs. The scale bar corresponds to 50 nm. **b** Representative cryo-EM 2D class averages of particles corresponding to the POPC/POPS/PIP2-PI3Kα/KRas/peptide monomer and dimer complexes. **c-d** Gold Standard Fourier Shell Correlation (GSFSC) of final maps used for model building for the POPC/POPS/PIP2-PI3Kα/KRas/peptide monomer **(c)** and dimer **(d)** complexes from CryoSparc4. **e-f** Directional FSCs of the POPC/POPS/PIP2-PI3Kα/KRas/peptide monomer **(e)** and dimer **(f)** complexes calculated by the 3DFSC server. **g** Processing workflow of POPC/POPS/PIP2-PI3Kα/KRas/peptide complex dataset. h-i Cryo-EM maps of the POPC/POPS/PIP2-PI3Kα/KRas/peptide monomer **(h)** and dimer **(i)** complexes colored according to local resolution determined by ResMap.

Strikingly, a subset of particles within this dataset were dimeric, something we had not observed in any of our previous datasets without peptide. These particles yielded a 2.61 Å reconstruction of a PI3Kα/KRas complex dimer with an extensive dimerization interface (BSA = 3,164 $Å^2$) mediated by the two p110α subunits **(Fig. 2.11 b)**. In our structure, the dimer cradles the nanodisc, with each PI3Kα/KRas pair making membrane interactions with opposite sides of the nanodisc. This arrangement likely arises due to the limited membrane surface area available for such a large complex, with PI3Kα striking a balance between its affinity for membrane lipids and its affinity for dimerization.

The dimerization interface is stabilized by extensive polar contacts between the C2 domain of one p110α subunit and the ABD-RBD linker of the second p110α subunit **(Fig. 2.11 c)**. The interface is further reinforced by two salt-bridges formed between Glu 707 of the kinase domain and Lys 678 of the helical domain of one p110α subunit with Arg 349 and Glu 469 of the C2 domain of the other p110α subunit, respectively. Interestingly, this interface is only accessible for dimerization upon maximal displacement of the iSH2 and ABD domains away from the catalytic core of p110α, which is only achieved when PI3Kα binds phosphopeptide **(Fig. 2.11 d)**.

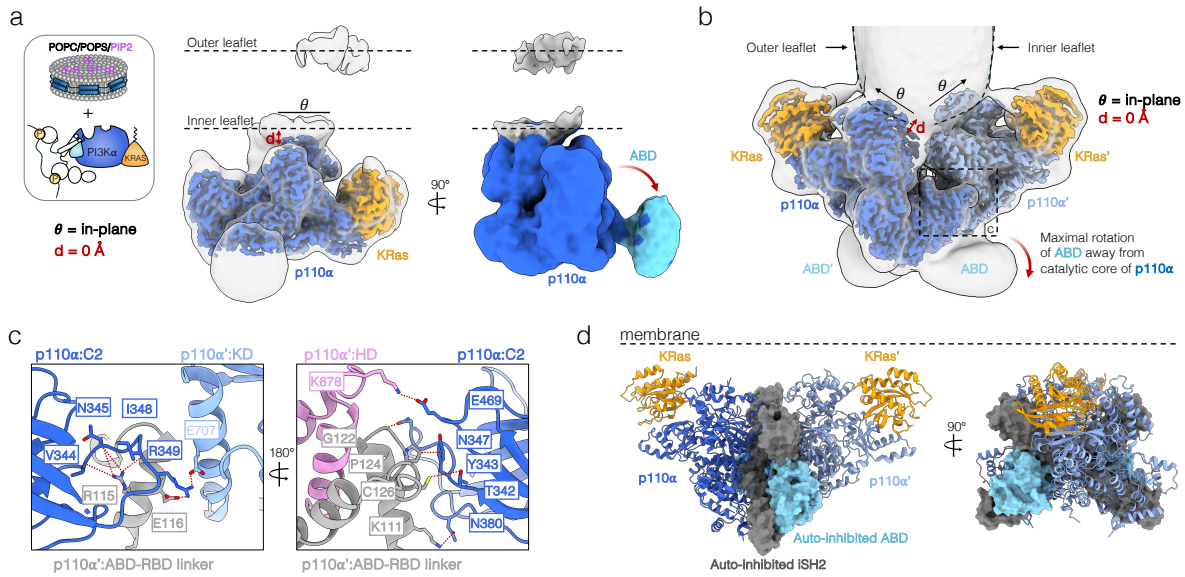


Figure 2.11: Phosphopeptide binding induces p110α-mediated dimerization of the PI3Kα/KRas complex

a Cryo-EM map of the PI3Kα/KRas/peptide complex bound to POPC/POPS/PIP2 nanodiscs overlayed with a transparent 10 Å low-pass filtered version of the same map to highlight membrane interface (left) and an 8 Å low-pass filtered map (right) illustrating displacement of inhibitory domains from the catalytic core of p110α. p110α in shown in blue and KRas in orange. **b** Cryo-EM map of the dimeric PI3Kα/KRas/peptide complex bound to POPC/POPS/PIP2 nanodiscs overlayed with a transparent 10 Å low-pass filtered version of the same map to highlight membrane interface. The p110α subunits are colored in light and dark blue, KRas molecules are colored in orange. **c** Zoomed-in view of the dimerization interface of the PI3Kα/KRas/peptide complex. C2 domain of one p110α subunit is shown in dark blue, and ABD-RBD linker, kinase domain, and helical domains of the other p110α monomer are shown in grey, light blue and pink, respectively. **d** Structure of the PI3Kα/KRas/peptide dimeric complex (in cartoon representation) aligned with two sets of iSH2 (grey) and ABD (cyan) domains from the POPC/POPS-bound Class 1 structure (in surface representation), illustrating the severe steric clash between these domains in their autoinhibited conformations and the dimerization interface of the PI3Kα/KRas/peptide complex.

In the dimeric complex, KRas inserts into the membrane at an unconventional angle to accommodate the large membrane curvature resulting from the flipped orientation of the nanodisc. To assess the feasibility of this interaction angle under more physiological membrane curvatures, we analyzed all nanodisc-bound structures of Ras in the Protein Data Bank. Our analysis focused on the angle of helix α5, which precedes the unstructured c-terminal hyper-variable region of Ras, in relation to the nanodisc plane. We categorized the insertion angles into three broad types: direct insertion, oblique and in-plane, with helix α5 interfacing with the membrane at approximately 90°, 45° and 0° angles **(Fig. 2.12 a)**. Across the PDB structures, we observed considerable variability in Ras insertion angles, with dimeric Ras structures exhibiting the highest angles of insertion. Although our dimeric complex had the lowest membrane insertion angles of Ras, around 30°, across our structures, this aligned with nearly half of the reported structures **(Fig. 2.12 b)**. Furthermore, the wide range of Ras membrane orientations underscores Ras's ability to dynamically engage with the membrane and adapt to different membrane curvatures, facilitating the formation of the dimeric complex.

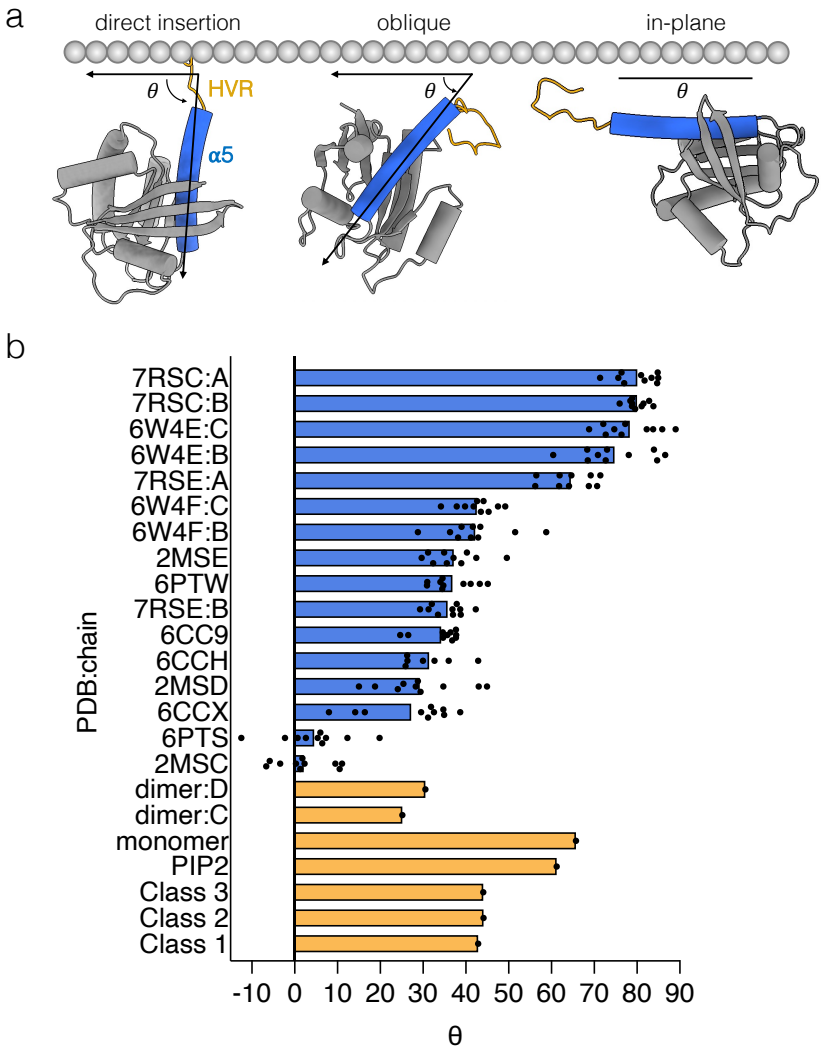


Figure 2.12: Dynamic membrane insertion of Ras

a Examples of Ras membrane insertion angles from the PDB. **b** Insertion angles of Ras as part of nanodisc-bound NMR structures from the PDB and KRas as part of our membrane-bound PI3Kα/KRas complex structures. Measurements represent the angle between helix α5 and the plane of the nanodisc. Each data point within a PDB corresponds to each model within the NMR ensemble.

DISCUSSION

Our membrane-bound structures of the PI3Kα/KRas complex provide a detailed map of the activation trajectory of PI3Kα. The three POPC/POPC-bound structures reveal that membrane binding alone, in the context of KRas, is sufficient to weaken inhibitory contacts between p85α and p110α, resulting in complete disruption of nSH2 domain contacts and partial disruption of iSH2/ABD domain contacts with the p110α catalytic core. These global rearrangements translate to critical changes in the active site of PI3Kα, including the release of the activation loop and the unstructured helix kα12 from inhibitory inter- and intra-subunit interactions, respectively. In nearly all auto-inhibited PI3Kα crystal structures, helix kα12 adopts a conformation similar to that observed in the Class 1 POPC/POPS-bound state, extended away from the active site[7,30,31]. However, in these structures, helix kα12 makes crystal contacts with the RBD of another PI3Kα molecule, making its functional significance uncertain, until now.

The structure of the PIP2-bound complex reveals that even in the absence of an activating phosphopeptide, substrate binding drives near-complete displacement of the inhibitory iSH2 and ABD domains. As these domains are wedged between the catalytic core of PI3Kα and the membrane, their release is crucial to enabling the tight and extensive interface formed between the active site of PI3Kα and the membrane in the presence of PIP2. Furthermore, binding of PIP2 causes the activation loop to extend toward the membrane and helix kα12 to undergo a ~180° rotation toward the active site of PI3Kα, where it adopts a helical structure. Interestingly, this inward conformation of helix kα12 is observed in the crystal structures of the auto-inhibited Class I PI3Ks, PI3Kβ and PI3Kγ, whereas in the active state structure of the Class III PI3K, Vps34, helix kα12 is rotated away from the active site[7,32-34]. Thus, based on these structures, the

inward conformation of helix kα12 has been generally interpreted as inactive. However, the coordinated displacement of the inhibitory nSH2, iSH2 and ABD domains along with the inward rotation of helix kα12 observed in our structures suggest that this inward conformation constitutes a critical component of the active state of PI3Kα. Intriguingly, in crystal structures of the oncogenic PI3Kα mutant, H1047R, helix kα12 is rotated towards the active site, although it remains unstructured[35].

Helix kα12 has been shown to play a critical role in the regulation of membrane binding and lipid kinase activity in Class I and Class III PI3Ks, although the exact mechanism of this function has been unclear[30,32,34,36]. A trio of hydrophobic residues within helix kα12 of PI3Kα, known as the "WIF" motif, has been biochemically identified as a major component of this regulatory effect. Upon adopting an inward confirmation in our PIP2-bound structure, helix kα12 gains three sets of critical interactions, with the "WIF" motif being a key participant. First, it forms polar contacts with the catalytic loop of PI3Kα, stabilizing it for catalysis. This conformation additionally positions helix kα12 in-plane with the membrane, making direct contact with membrane lipid densities, reinforcing the PI3Kα/membrane interface. Lastly, the activation loop and helix kα12 wedge the PIP2 lipid density deep within the active site of PI3Kα, trapping the PIP2 substrate for phosphorylation. Together, our POPC/POPS and PIP2-bound structures of the PI3Kα/KRas complex rationalize the functional significance of helix kα12 and the "WIF" motif in membrane binding and catalysis.

Finally, our structures of PI3Kα in complex with both an RTK-derived phosphopeptide and KRas on PIP2-containing membranes provide a comprehensive view of the PI3Kα activation cycle. In the presence of phosphopeptide, PI3Kα exists in a dynamic equilibrium

between its monomeric and dimeric forms. As a monomer, the dually activated complex is largely consistent with the PIP2-only bound state, with the activation loop and helix kα12 adopting nearly identical conformations as those seen in the absence of peptide. However, peptide binding does induce additional displacement of the inhibitory iSH2 and ABD domains from the catalytic core of p110α. This suggests that the significant role of RTK binding is likely the recruitment of PI3Kα to the plasma membrane where it can engage PIP2.

Our structure of the dimeric PI3Kα/KRas complex offers the first high-resolution visualization of a phenomenon that was observed biochemically more than 20 years ago. Early studies established that the N-terminus of the p85 regulatory subunit facilitates dimerization between two p85 molecules. Specifically, the SH3 domain of one molecule binds a proline-rich motif of the second molecule and vice versa while the BH domains engage one another[37]. It was additionally shown that phosphopeptide binding induces homodimerization of the p85/p110 heterodimer[17]. Our dimeric structure explains why dimerization of the p85/p110 heterodimer is driven by phosphopeptide-binding. Simply, the inhibitory iSH2 and ABD domains must undergo complete displacement from the p110α core to allow for the establishment of the p110α-mediated dimerization interface and this only occurs upon complete activation of PI3Kα. Because we do not resolve p85α in our dimeric structure, likely due to its flexibility, it is unclear whether this dimer is initiated through p85α-p85α interactions followed by the formation of the p110α/p110α interface or whether two distinct dimers exist with discrete roles. Both p85 homodimers and PI3Kα/PI3Kβ heterodimers have been implicated in the regulation of PTEN, by preferentially binding PTEN and increasing its activity, suggesting that dimeric PI3K complexes may negatively regulate the PI3K/AKT pathway[14,15]. However, the existence of multi-site PI3K scaffolds such as HER3 and IRS1, which are primed to simultaneously recruit multiple

molecules of PI3K, raise the possibility that PI3K dimerization may serve as a mechanism to enhance its activity.

Lastly, it has long been an open question whether enhanced activation of PI3Kα in the presence of Ras is driven by the membrane-anchoring effect of Ras or its allosteric regulation of PI3Kα's kinase activity. It is unknown how much of the dis-inhibition we observe in the POPC/POPS-bound structures of PI3Kα is a result of its association with KRas or the membrane. However, given that altering the lipid composition, through the addition of PIP2, results in sweeping conformational rearrangements in PI3Kα, consistent with activation of the enzyme, it is likely the contribution of membrane to activation is significant.

MATERIALS AND METHODS

PI3Kα virus generation, expression and purification

Full length p85α and p110α were cloned into pFastBac1 and pFastBacHT B vectors respectively. The p85α subunit is untagged while the p110α vector encodes an N-terminal 6X His tag. Baculovirus was generated for each construct separately using the DH10Bac system. The p85α and p110α heterodimer was co-expressed in Sf9 insect cells by co-infection of individual baculoviruses at 27 C. Cells were harvested after 72 hours, centrifuged and flash frozen in liquid nitrogen for later use.

Pellets were resuspended in 50 mM Sodium Phosphate buffer, pH 8, 400 mM NaCl, 10 mM imidazole, 5% glycerol, 1% triton X-100, 10 mM βME. Cells were lysed by sonication at 40% amplitude for 5 min (10 sec ON, 5 sec OFF) using an and spun down in an Optima L-90K ultracentrifuge (Beckman Coulter) equipped with a 45 Ti rotor at 40,000 rpm for 1 hr at 4 C. The clarified lysate was filtered using a 0.22 μm syringe filter and loaded onto a 1 mL HisTrap HP column equilibrated with binding buffer consisting of 50 mM Sodium Phosphate buffer, pH 8, 400 mM NaCl, 10 mM Imidazole, 10 mM βME. The column was washed with 15 column volumes of binding buffer and eluted with binding buffer containing 250 mM Imidazole using a linear imidazole gradient over 35 column volumes. The eluate was diluted 2-fold with binding buffer without Imidazole and glycerol was added at a final concertation of 5%. The eluate was then concentrated using an Amicon Ultra-15 100k MWCO centrifugal filter and loaded onto a Superdex 200 increase 10/300 GL or Superose 6 increase 10/300 GL column and separated using an isocratic gradient of 50 mM Tris pH 7.5, 150 mM NaCl, 10 % glycerol, 1 mM TCEP. Peak fractions were concentrated using Amicon-Ultra 0.5 mL 100k MWCO centrifugal filters

KRAS4b-FME virus generation, expression and purification

A full-length farnesylated and methylated KRAS4b (KRAS-FME) was produced as previously described[38]. Briefly, a clone for human KRAS4b (amino acids 2-188) with an upstream TEV protease cleavage site and an N-terminal 6XHis-MBP fusion tag was transformed into *E. coli* DE35 and plated on LB agar with 7μg/ml gentamicin, 50 μg/mL kanamycin, 10 μg/mL tetracycline, 100 μg/ml Bluo-gal, and 40 μg/mL IPTG. White colonies were grown in liquid culture, and bacmid DNA was purified by alkaline lysis. Positive clones were transfected into 100 mL of Tni-FNL insect cells at 1.5 x 10^6 cells/mL, grown at 27 °C for 4-6 days. The resulting P1 baculovirus was used to infect expression cultures, which were spun down and their pellets flash frozen after 72 hours.

Pellets were resuspended in 20 mM HEPES, pH 7.3, 300 mM NaCl, 5 mM MgCl2, 1 mM TCEP, and 1 x protease inhibitor tablet (Sigma Aldrich). Cells were lysed using an EmulsiFlex-C5 homogenizer (Avestin) and the cell lysate was clarified by ultracentrifugation at 50,000 xg for 30 min, at 4 °C. Imidazole was added to the supernatant at a final concertation of 35 mM and loaded onto a 10 mM IMAC column (HisTrap, GE Healthcare) equilibrated with 20 mM HEPES, pH 7.3, 300 mM NaCl, 5 mM MgCl2, 1 mM TCEP, 35 mM imidazole and protease inhibitor tablet. The column was washed with equilibration buffer and proteins eluted with increasing imidazole gradient up to 500 mM imidazole. Peak fractions were dialyzed into 20 mM MES, pH 6.0, 150 mM NaCl, 5 mM MgCl2 and 1 mM TCEP and diluted into dialysis buffer to reduce salt concentration to 75 mM NaCl. Dialyzed protein was loaded onto a 10 mL SP Sepharose column equilibrated with 20 mM MES, pH 6.0, 75 mM NaCl, 5 mM MgCl2, and 1 mM TCEP. The column was washed and then eluted with a salt gradient of up to 650 mM NaCl. Protein was incubated with TEV protease and simultaneously dialyzed into 20 mM HEPES, pH

7.3, 300 mM NaCl and 5 mM MgCl2, and 1 mM TCEP overnight at 4 °C. Digested protein was separated by IMAC, peak fractions pooled, concentrated using an Amicon-Ultra10k MWCO centrifugal filters and flash frozen for storage at -80 °C.

Nanodisc preparation

Chloroform/methanol solutions of POPC, POPS and PIP2 (Avanti Polar Lipids: 850457, 840034, 840046) were prepared and mixed together in the appropriate molar ratios (65:35 POPC:POPS for non-PIP2 nanodiscs and 70:25:5 POPC:POPS:PIP2 for PIP2 nanodiscs) in glass vials. Lipids were initially dried down under nitrogen gas and left overnight in a freeze dryer for complete solvent evaporation. Lipid films were resuspended in 20 mM Tris, pH 7.5, 100 mM NaCl, 0.5 mM EDTA, 40 mM Sodium Cholate to a final lipid concentration of 20 mM. Resuspended lipids were vortexed and sonicated in a bath sonicator for 45 minutes for solubilization. Detergent-solubilized lipids were incubated with mixed with MSP1E3D1 protein at a 1:130 (non-PIP2 lipid mixtures) and 1:140 (PIP2-conatining lipid mixtures) molar ratio (MSP:lipid) for 1 hr on ice (Sigma-Aldrich, M7074). Bio-beads (Bio-Rad, 1528920) were activated in methanol for 30 min while shaking and thoroughly washed with ddH2O and 20 mM Tris, pH 7.5, 100 mM NaCl. Bio-beads were then added to the lipids-MSP mixtures at a final concentration of 0.8 mg/mL and incubated overnight at 4 C with shaking. Nanodiscs were purified using either a Superdex 200 increase 10/300 GL or Superose 6 increase 10/300 GL column with an isocratic gradient of 50 mM Tris pH 7.5, 150 mM NaCl, 1 mM TCEP. Peak fractions were concentrated using Amicon-Ultra 0.5 mL 30k MWCO centrifugal filters.

Complex formation and sample preparation for cryo-electron microscopy imaging

PI3Kα, KRAS4b-FME and molecular glue were incubated at final concentrations of 3 μM, 6 μM and 30 μM, respectively, for 1 hr on ice. Nanodiscs were added to the protein complex mixture to a final concentration of 6 μM and incubated for an additional 45 min at RT. PI3Kα-KRAS4b-FME-nanodisc complexes were loaded onto a Superdex 200 increase 5/150 GL column and separated using an isocratic gradient of 50 mM Tris pH 7.5, 150 mM NaCl, 1 mM TCEP. For bis-phosphopeptide-bound complexes, PI3Kα, KRAS4b-FME, and molecular glue were incubated with a HER3-dervied bis-phosphopeptide (GD(p)YAAMGACPASEQG(p)YEEMRA, Genscript) at a final concentration of 15 μM for 1 hr on ice, followed by incubation with nanodiscs and separation by size exclusion chromatography. The peptide-bound complex was also prepared by forming PI3Kα- KRAS4b-FME-nanodisc complex first, followed by incubation with bis-phosphopeptide for 1 hr on ice and by separation by size exclusion chromatography. The order of peptide addition did not effect the resulting PI3Kα- KRAS4b-FME-nanodsic complex cryo-EM maps.

Peak fractions of each complex were pooled and diluted to a 40 mAU equivalent concentration. Immediately before preparing cryo-EM grids, fluorinated octyl maltoside was added to the samples at a final concentration of 0.0125% to alleviate orientation bias of nanodisc-bound complexes. For the POPC/POPS nanodisc complex, 3 uL of sample was applied to graphene-oxide coated Quantifoil R1.2/1.3 300 mesh Au holey-carbon grids, blotted using a Vitrobot Mark IV (FEI), and plunge frozen in liquid ethane at 5 °C, 100% humidity, 30 sec wait time, 7 sec blot time, and 0 blot force. For the POPC/POPS/PIP2 nanodisc complexes, in the presence or absence of bisphosphopeptide, 3 uL of sample was applied to graphene-oxide coated Quantifoil R1.2/1.3 300 mesh Au holey-carbon grids functionalized with PEG-amine, to combat

the excess negative charge from PIP2 and bisphosphopeptide. Grids were blotted and plunge frozen in liquid ethane at 5 °C, 100% humidity, 30 sec wait time, 3 sec blot time, and 0 blot force.

Grids were imaged on a 300-keV Titan Krios (FEI) with a K3 direct electron detector (Gatan) and a BioQuantum energy filter (Gatan) using SerialEM v4.1 and Digital Micrograph v3.2. Data for the PI3Kα- KRAS4b-FME-nanodsic complexes were collected in non-super-resolution mode at a physical pixel size of 0.8189 Å $pixel^{-1}$, with a dose rate of 16.0 e^{-} $pixel^{-1}$ s^{-1} (operated in non-CDS mode), at a nominal magnification of 105,000x. Images were recorded with a 2 sec exposure over 80 frames with a dose rate of 0.57 e^{-} $Å^{-2}$ per frame.

Image processing and 3D reconstruction

Raw movies were corrected for motion and radiation damage with MotionCor2[39] during collection launched via Scipion[40] (developer version), and the resulting sums were imported in CryoSPARC v4.2. Micrographs were curated based on ice thickness, CTF fit resolution, and particle distribution. Micrograph contrast transfer function (CTF) parameters were estimated with the patch CTF job in CryoSPARC. The following is a brief description of the general processing workflow for all datasets. See processing workflow charts for further details (Figures 2.2, 2.7, 2.10). Particles were initially picked with blob picking, extracted, and 2D-classified yielding templates for template picking. Particles were then template picked with low-pass filtered (to 20 Å) 2D class averages and resulting picks were extracted with 4× Fourier cropping and subjected to iterative rounds of ab initio and heterogeneous refinements. Refined particle stacks were then used to train Topaz and extract 4x binned particles from Topaz-based particle picking. These particles were subjected to iterative rounds of ab initio and heterogeneous

refinements. Finally, unbinned particles were re-extracted and run through non-uniform refinements to achieve reconstruction with the highest resolution. The final reconstructions of the POPC/POPS-bound PI3Kα/KRas Class 1, Class 2 and Class3 complexes used for model building included 111,772; 114,960; 117,424 particles with C1 symmetry and resulted in overall resolutions of 3.01 Å, 3.23 Å and 3.05 Å by gold standard FSC (GS-FSC) cut-off of 0.143 (masked), sharpened with -103.5, -111.9 and -103.3 B-factors, respectively. The final reconstruction of the POPC/POPS/PIP2-bound PI3Kα/KRas complex used for model building included 127,559 particles with C1 symmetry and resulted in an overall resolution of 2.88 Å, sharpened with -103.8 B-factor. The POPC/POPS/PIP2-bound PI3Kα/KRas/peptide monomer and dimer complexes used for model building included 166,142 and 221,966 particles with C1 and C2 symmetry, respectively, and resulted in overall resolutions of 2.84 Å and 2.61 Å, sharpened with -101.4 and -97.1 B-factors. Finally, each map was assessed for local and directional resolutions through ResMap v1.1.461 and 3DFSC v3.062 server, respectively.

Model building, refinement, and validation

Model building for PI3Kα/KRas complexes began with the alignment of the AlphaFold2 models of p85α, p110α, and KRas onto the p110γ/HRas crystal structure (1HE8). The resulting models were then rigid body fit into the corresponding 3D volumes in ChimeraX 1.6.1. The models were then torsion relaxed into their respective cryo-EM maps with FastRelax protocol in Rosetta 3.0[41] in torsion space and then were further manually examined and refined in Coot and ISOLDE[42]. Per-atom B-factors were assigned in Rosetta indicating the local quality of the map around that atom.

REFERENCES

1. Samuels, Y. & Waldman, T. Oncogenic mutations of PIK3CA in human cancers. *Curr Top Microbiol Immunol* **347**, 21-41 (2010).
2. Samuels, Y. *et al.* High frequency of mutations of the PIK3CA gene in human cancers. *Science* **304**, 554 (2004).
3. Samuels, Y. *et al.* Mutant PIK3CA promotes cell growth and invasion of human cancer cells. *Cancer Cell* **7**, 561-573 (2005).
4. Kang, S., Denley, A., Vanhaesebroeck, B. & Vogt, P. K. Oncogenic transformation induced by the p110beta, -gamma, and -delta isoforms of class I phosphoinositide 3-kinase. *Proc Natl Acad Sci U S A* **103**, 1289-1294 (2006).
5. Jaiswal, B. S. *et al.* Somatic mutations in p85alpha promote tumorigenesis through class IA PI3K activation. *Cancer Cell* **16**, 463-474 (2009).
6. Sun, M., Hillmann, P., Hofmann, B. T., Hart, J. R. & Vogt, P. K. Cancer-derived mutations in the regulatory subunit p85alpha of phosphoinositide 3-kinase function through the catalytic subunit p110alpha. *Proc Natl Acad Sci U S A* **107**, 15547-15552 (2010).
7. Vadas, O., Burke, J. E., Zhang, X., Berndt, A. & Williams, R. L. Structural basis for activation and inhibition of class I phosphoinositide 3-kinases. *Sci Signal* **4**, re2 (2011).
8. Burke, J. E. & Williams, R. L. Synergy in activating class I PI3Ks. *Trends Biochem Sci* **40**, 88-100 (2015).
9. Cuesta, C., Arevalo-Alameda, C. & Castellano, E. The Importance of Being PI3K in the RAS Signaling Network. *Genes (Basel)* **12** (2021).

10. Prior, I. A., Lewis, P. D. & Mattos, C. A comprehensive survey of Ras mutations in cancer. *Cancer Res* **72**, 2457-2467 (2012).

11. Buckles, T. C., Ziemba, B. P., Masson, G. R., Williams, R. L. & Falke, J. J. Single-Molecule Study Reveals How Receptor and Ras Synergistically Activate PI3Kalpha and PIP(3) Signaling. *Biophys J* **113**, 2396-2405 (2017).

12. Bell, C. M., Raffeiner, P., Hart, J. R. & Vogt, P. K. PIK3CA Cooperates with KRAS to Promote MYC Activity and Tumorigenesis via the Bromodomain Protein BRD9. *Cancers (Basel)* **11** (2019).

13. Gupta, S. *et al.* Binding of ras to phosphoinositide 3-kinase p110alpha is required for ras-driven tumorigenesis in mice. *Cell* **129**, 957-968 (2007).

14. Cheung, L. W. *et al.* Regulation of the PI3K pathway through a p85alpha monomer-homodimer equilibrium. *Elife* **4**, e06866 (2015).

15. Perez-Garcia, V., Redondo-Munoz, J., Kumar, A. & Carrera, A. C. Cell activation-induced phosphoinositide 3-kinase alpha/beta dimerization regulates PTEN activity. *Mol Cell Biol* **34**, 3359-3373 (2014).

16. Clayton, N. S. *et al.* Assembly of nuclear dimers of PI3K regulatory subunits is regulated by the Cdc42-activated tyrosine kinase ACK. *J Biol Chem* **298**, 101916 (2022).

17. Layton, M. J., Harpur, A. G., Panayotou, G., Bastiaens, P. I. & Waterfield, M. D. Binding of a diphosphotyrosine-containing peptide that mimics activated platelet-derived growth factor receptor beta induces oligomerization of phosphatidylinositol 3-kinase. *J Biol Chem* **273**, 33379-33385 (1998).

18. Backer, J. M. The regulation of class IA PI 3-kinases by inter-subunit interactions. *Curr Top Microbiol Immunol* **346**, 87-114 (2010).

19. Burke, J. E. & Williams, R. L. Dynamic steps in receptor tyrosine kinase mediated activation of class IA phosphoinositide 3-kinases (PI3K) captured by H/D exchange (HDX-MS). *Adv Biol Regul* **53**, 97-110 (2013).

20. Miller, M. S. *et al.* Structural basis of nSH2 regulation and lipid binding in PI3Kalpha. *Oncotarget* **5**, 5198-5208 (2014).

21. Wu, H. *et al.* Regulation of Class IA PI 3-kinases: C2 domain-iSH2 domain contacts inhibit p85/p110alpha and are disrupted in oncogenic p85 mutants. *Proc Natl Acad Sci U S A* **106**, 20258-20263 (2009).

22. Yu, J., Wjasow, C. & Backer, J. M. Regulation of the p85/p110alpha phosphatidylinositol 3'-kinase. Distinct roles for the n-terminal and c-terminal SH2 domains. *J Biol Chem* **273**, 30199-30203 (1998).

23. Yu, J. *et al.* Regulation of the p85/p110 phosphatidylinositol 3'-kinase: stabilization and inhibition of the p110alpha catalytic subunit by the p85 regulatory subunit. *Mol Cell Biol* **18**, 1379-1387 (1998).

24. Burke, J. E., Perisic, O., Masson, G. R., Vadas, O. & Williams, R. L. Oncogenic mutations mimic and enhance dynamic events in the natural activation of phosphoinositide 3-kinase p110alpha (PIK3CA). *Proc Natl Acad Sci U S A* **109**, 15259-15264 (2012).

25. Siempelkamp, B. D., Rathinaswamy, M. K., Jenkins, M. L. & Burke, J. E. Molecular mechanism of activation of class IA phosphoinositide 3-kinases (PI3Ks) by membrane-localized HRas. *J Biol Chem* **292**, 12256-12266 (2017).

26. Burke, J. E., Perisic, O. & Williams, R. L. Allosteric activation of PI3Kalpha by oncogenic mutations. *Oncotarget* **4**, 180-181 (2013).

27. Burke, J. E. *et al.* Dynamics of the phosphoinositide 3-kinase p110delta interaction with p85alpha and membranes reveals aspects of regulation distinct from p110alpha. *Structure* **19**, 1127-1137 (2011).

28. Jenkins, M. L. *et al.* Oncogenic mutations of PIK3CA lead to increased membrane recruitment driven by reorientation of the ABD, p85 and C-terminus. *Nat Commun* **14**, 181 (2023).

29. Pacold, M. E. *et al.* Crystal structure and functional analysis of Ras binding to its effector phosphoinositide 3-kinase gamma. *Cell* **103**, 931-943 (2000).

30. Hon, W. C., Berndt, A. & Williams, R. L. Regulation of lipid binding underlies the activation mechanism of class IA PI3-kinases. *Oncogene* **31**, 3655-3666 (2012).

31. Zhang, M., Jang, H. & Nussinov, R. Structural Features that Distinguish Inactive and Active PI3K Lipid Kinases. *J Mol Biol* **432**, 5849-5859 (2020).

32. Zhang, X. *et al.* Structure of lipid kinase p110beta/p85beta elucidates an unusual SH2-domain-mediated inhibitory mechanism. *Mol Cell* **41**, 567-578 (2011).

33. Walker, E. H. *et al.* Structural determinants of phosphoinositide 3-kinase inhibition by wortmannin, LY294002, quercetin, myricetin, and staurosporine. *Mol Cell* **6**, 909-919 (2000).

34. Miller, S. *et al.* Shaping development of autophagy inhibitors with the structure of the lipid kinase Vps34. *Science* **327**, 1638-1642 (2010).

35. Mandelker, D. *et al.* A frequent kinase domain mutation that changes the interaction between PI3Kalpha and the membrane. *Proc Natl Acad Sci U S A* **106**, 16996-17001 (2009).

36. Rostislavleva, K. *et al.* Structure and flexibility of the endosomal Vps34 complex reveals the basis of its function on membranes. *Science* **350**, aac7365 (2015).

37. Harpur, A. G. *et al.* Intermolecular interactions of the p85alpha regulatory subunit of phosphatidylinositol 3-kinase. *J Biol Chem* **274**, 12323-12332 (1999).

38. Gillette, W. K. *et al.* Farnesylated and methylated KRAS4b: high yield production of protein suitable for biophysical studies of prenylated protein-lipid interactions. *Sci Rep* **5**, 15916 (2015).

39. Zheng, S. Q. *et al.* MotionCor2: anisotropic correction of beam-induced motion for improved cryo-electron microscopy. *Nat Methods* **14**, 331-332 (2017).

40. De la Rosa-Trevín, J. *et al.* Scipion: A software framework toward integration, reproducibility and validation in 3D electron microscopy. *Journal of structural biology* **195**, 93-99 (2016).

41. DiMaio, F. *et al.* Atomic-accuracy models from 4.5-A cryo-electron microscopy data with density-guided iterative local refinement. *Nat Methods* **12**, 361-365 (2015).

42. Croll, T. I. ISOLDE: a physically realistic environment for model building into low-resolution electron-density maps. *Acta Crystallogr D Struct Biol* **74**, 519-530 (2018).

Publishing Agreement

It is the policy of the University to encourage open access and broad distribution of all theses, dissertations, and manuscripts. The Graduate Division will facilitate the distribution of UCSF theses, dissertations, and manuscripts to the UCSF Library for open access and distribution. UCSF will make such theses, dissertations, and manuscripts accessible to the public and will take reasonable steps to preserve these works in perpetuity.

I hereby grant the non-exclusive, perpetual right to The Regents of the University of California to reproduce, publicly display, distribute, preserve, and publish copies of my thesis, dissertation, or manuscript in any form or media, now existing or later derived, including access online for teaching, research, and public service purposes.

DocuSigned by:
2877F8F85404400...
Author Signature

5/23/2024
Date